STUDY OF ULTRASHORT-PULSE CODE-DIVISION MULTIPLE-ACCESS SCHEME FOR FIBER-OPTIC COMMUNICATIONS AND ITS HYBRID SPECTRAL OVERLAY WITH WAVELENGTH-DIVISION-MULTIPLEXING TECHNIQUE

A Thesis

Submitted to the Faculty

of

Purdue University

by

Shuai Shen

In Partial Fulfillment of the

Requirements for the Degree

of

Doctor of Philosophy

December 2000

To my family.

ACKNOWLEDGMENTS

Thanks to Prof. Andrew M. Weiner for his encouragement, guidance and support throughout my Ph.D. study. Thanks to Dan Leaird for his outstanding technical assistance in many of my research projects. Most of all, I am indebted to my beloved wife Rui (Judy), for her support and for her tolerance of my working late regularly and often over the weekend.

TABLE OF CONTENTS

LIST OF TABLES

LIST OF FIGURES

ABSTRACT

Shen, Shuai, Ph.D., Purdue University, December, 2000. Study of Ultrashort-pulse Code-division Multiple-access Scheme for Fiber-optic Communications and its Hybrid Spectral Overlay with Wavelength-division-multiplexing Technique. Major Professor: Andrew M. Weiner.

This dissertation demonstrates and extends the technical feasibility of spectral phase encoding/decoding based ultrashort-pulse optical code-division multiple-access (CDMA) scheme for local-area and metropolitan-area fiber-optic communications. The ultrashort pulse CDMA technique not only provides a unique multiplexing possibility on its own, but also complements other multiplexing approaches, in particular optical wavelength-division-multiplexing (WDM) technique. This thesis work includes both device and system level studies. At the device level, a femtosecond fiber laser was constructed as a broadband source for CDMA experiments. The complete dispersion compensation for distortion-less transmission of 400-fs pulses over a 10-km fiber link was achieved through the use of a dispersion compensating fiber and a femtosecond pulse shaper. The accumulated fiber nonlinearity during ultrashort-pulse propagation was investigated to facilitate power budget analysis in CDMA data transmission. At the system level, the bit-error-rate performance of a CDMA channel under multi-access interference was evaluated. The possibility of error-free CDMA operation in a multi-user environment was demonstrated. The feasibility of spectrally overlaying CDMA on WDM for the hybrid WDM/CDMA operation was also investigated through back-to-back system measurements.

1. Introduction

1.1 Scope of This Dissertation

This dissertation demonstrates and extends the technical feasibility of spectral phase encoding/decoding based ultrashort-pulse optical code-division multiple-access (CDMA) scheme for local-area and metropolitan-area fiber-optic communications. The CDMA technique not only provides a unique multiplexing possibility on its own right, but also complements other multiplexing approaches, in particular optical wavelength-division-multiplexing (WDM) technique.

In optical communications, there are three major multi-access techniques that allow users to share the same transmission media – time-division-multiplexing (TDM), wavelength-division-multiplexing (WDM) and code-division multiple-access (CDMA). Unlike in a TDM or WDM system, where users are distinguished either in the time or spectral domain, multiplexing in an optical CDMA system is achieved through assigning different minimally-correlated code-sequences to users. The use of encoding and decoding brings forth several unique features and advantages that make CDMA attractive. The most significant advantages are the possibility of higher level data security and the graceful system performance in a bursty environment (in another word, a CDMA system can support more users than that permitted by the code length). Note that the capacity in a WDM or TDM system is always "hard" limited by the physical channels available. Other advantages include (1) the elimination of high-speed electronic synchronization required in a TDM system or the precise frequency control of lasers required in a WDM system, (2) the possibility of all optical processing to perform certain network applications such as addressing and routing. These features could simplify the network management and increase overall system capacity. It should be noted that despite of its potentially advanced features, optical

CDMA is less explored in industry and university laboratory than TDM and WDM. This is perhaps because the technology required for implementing optical CDMA is less mature and maybe inherently more complex. Nonetheless, for some high performance applications, e.g. supercomputer interconnects over distance not exceeding tens of kilometers, it is desirable to have the unique networking advantages that optical CDMA could offer.

The concept of optical CDMA could be implemented in several different ways depending on the choice of sources (mode-locked laser [1] versus amplified spontaneous emission or LED [2]), coding schemes (time domain with fiber ladders [3] or tapped delay line [4] versus frequency domain with Fourier transformed pulse shaper [1]) and the detection method (direct O/E conversion [5] versus using nonlinear optical processing [6]). Each choice has its advantages and disadvantages. For example, the use of LED (incoherent source) may reduce the cost of CDMA system significantly. However, mode-locked lasers (coherent source) are expected to allow better system noise performance than LED, since a system with incoherent light source might suffer from optical beat noise, e. g. in coherent multiplexing approaches based on interferometric techniques [7]. One simple way to classify optical CDMA schemes is according to the choice of incoherent versus coherent processing. Since the coherent processing allows the manipulation of optical field, it could provide better suppression of multi-access interference than the incoherent processing (summing of optical power).

This dissertation focuses on a coherent CDMA technique called ultrashort-pulse optical CDMA based on spectral phase encoding/decoding. This technique takes advantage of high-fidelity femtosecond pulse shaping using multi-element spatial light modulator for spectral phase or amplitude encoding/decoding. It is expected that the ultrashort-pulse optical CDMA potentially offers a superior system performance over other CDMA alternatives (e. g. incoherent optical CDMA, etc.) due to its coherent processing and large spreading ratio. The main constraint appears to be the fidelity of the encoding/decoding operation for a user pair and the consequent successful detection in the presence of interference from other users. To demonstrate

the feasibility and usefulness of ultrashort-pulse CDMA for local- and metropolitan-area fiber-optic communications, this dissertation documents the research results on some key device technologies, on CDMA system performance evaluation in a multiple-user environment, and on a new multiplexing approach — spectral overlay of CDMA on WDM for hybrid WDM/CDMA operation.

1.2 Ultrashort-pulse Optical CDMA Systems

Fig. 1.1 shows the block diagram of an ultrashort-pulse fiber-optic CDMA system configured for local-area network (LAN) applications.

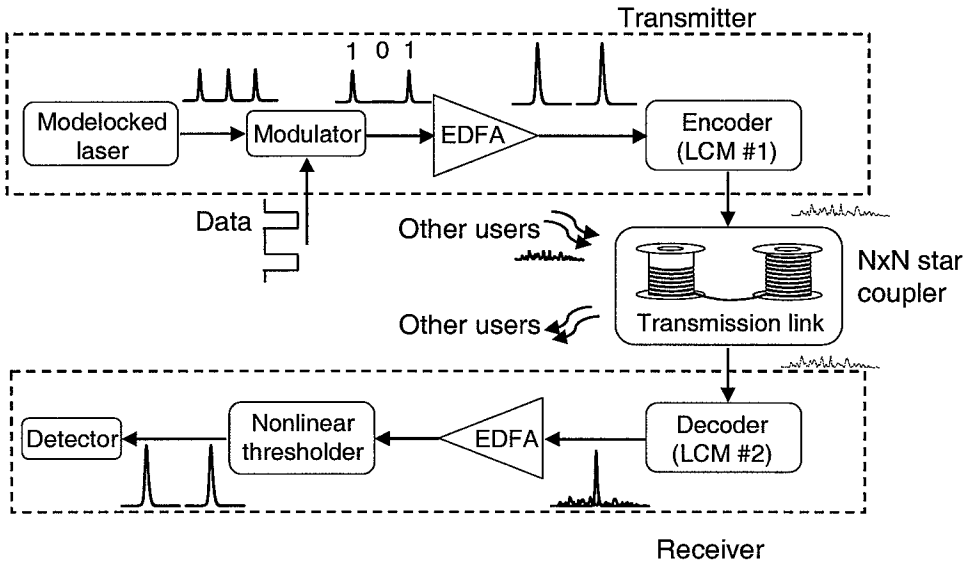

Fig. 1.1. Block diagram of an ultrashort-pulse optical CDMA system.

At the transmitter side, femtosecond laser pulses are spectrally encoded with a

pseudorandom phase code that transforms the laser pulses into picosecond-duration pseudonoise signals. Each user (transmitter) is assigned a unique phase code with which it encodes all its data bits. This phase code is chosen to be minimally interfering compared to the phase codes assigned to all the other users in the system. Different users can be connected in a simple broadcast-and-select architecture where all transmitters are connected to all receivers by a passive star coupler. Each receiver thus receives encoded data bits transmitted by every transmitter in the network, but the decoder in any one receiver matches the phase code of only one transmitter. Hence, only the encoded data bits of one transmitter that are intended for a particular receiver get properly decoded back to femtosecond pulse, and the encoded data bits transmitted by all other transmitters remain as improperly decoded interference tens of picosecond in duration. In this CDMA scheme, each transmitter may operate at moderate data rates (e. g. , on the order of 1 Gb/s), but higher overall data transmission rate may be achieved with multiple-access. A theoretical analysis of the crosstalk-limited performance of the ultrashort pulse CDMA scheme shows that the CDMA system capacity could range from ten to perhaps 100 Gb/s (depending the code length used in the system) [8].

The key components required for ultrashort pulse optical CDMA operation include: ultrashort-pulse laser source, fiber amplifier, optical encoder and decoder, dispersion compensated fiber link, and nonlinear thresholding devices. The followings explain the functions of some components in the CDMA system and my related thesis work.

Ultrashort-pulse laser provides wide spectral bandwidth and phase coherence for the spectral coding operation. It serves as a data-bit generator for each user in the system. Over the past decade, there has been a tremendous amount of research efforts toward developing ultrashort-pulse lasers for high speed fiber communications. Among these laser sources, femtosecond rare earth doped (in particular Erbium-doped) fiber laser offers inherent compatibility with other fiber optic technologies and is expected to be an ideal signal source for CDMA system. Spectral bandwidth up to

40 nm has been generated from fiber laser system. However, the output pulse energy from fiber laser tends to be relatively low and needs to be increased for practical networking applications. In this thesis work, a passively mode-locked fiber ring laser based on nonlinear polarization rotation was studied and developed for the CDMA operation.

The spectral phase encoding/decoding operation can be achieved through the use of a grating/lens based femtosecond pulse shaper, an array-waveguide-grating or a fiber Bragg grating [5, 9, 10, 11]. Although array-waveguide-grating and fiber Bragg grating are more compact than a pulse shaper, the pulse shaper technique pioneered by Weiner et. al. provides the best performance so far (e.g. the largest spectral bandwidth, the highest spectral resolution for phase modulation) [9, 12, 13]. A femtosecond pulse shaper consists of a grating pair, a lens pair and a programmable liquid crystal modulator array (LCM). The pseudorandom phase code is added to the input pulse spectrum by altering the relative phase of wavelength components in the femtosecond pulse. Encoding and decoding of ultrashort pulses have been demonstrated first at visible wavelengths [12] using free-space pulse shapers. The fiber-pigtailed pulse shaping at 1.55 μm wavelength with a 128-pixel programmable LCM was demonstrated with relatively low insertion loss ($\sim$ 5.8 dB) by our colleagues [14]. In the thesis work, this pulse shaper was used as a platform to study the encoding and decoding CDMA operation.

The use of spectral phase coding implies that fiber dispersion compensation is required for ultrashort-pulse propagation in a CDMA system. For femtosecond pulse CDMA operation, the simultaneous compensation of both the second and the third order dispersion of a SMF link is required. Several dispersion compensating techniques have been demonstrated. The dispersion-compensating fiber (DCF) technique is an especially attractive approach due to its ability to suppress the third order dispersion and its compatibility with all fiber systems. The 500-fs pulse transmission over a 2.5 km fiber link has been demonstrated using a dispersion-compensating fiber (DCF) [15]. When the DCF is combined with a pulse shaper [16], the nearly dispersion-free

transmission has been achieved for 500-fs pulses over the 2.5-km fiber link. In this thesis work, further efforts have been put forth to extend the distance of distortion-less femtosecond pulse propagation. Complete dispersion compensation for shorter pulse (400 fs) distortion-less transmission over 10-km fiber distance equivalent to LAN coverage has been achieved using the DCF/pulse-shaping technique. In addition, the accumulated fiber nonlinear effect during femtosecond pulse propagation over a dispersion compensated fiber link was also investigated. Since the quality of encoding and decoding operation is sensitive to the fiber nonlinear phase shifts, this study indicates the the nonlinearity-induced power limit during CDMA data transmission.

At the receiver side, properly decoded pulses (recovered high-intensity femtosecond pulses) and improperly decoded pulses (low intensity picosecond pseudonoise burst) have the same pulse energy. A nonlinear optical thresholding device is required to distinguish them through detecting the contrast in their peak intensity. This required discrimination has been accomplished by exploiting the nonlinear frequency shifts effect in optical fibers (self-phase modulation or Raman effects) [6, 17], two-photon absorption (TPA) effect in the optical waveguide [18] and second harmonic generation in periodic poled lithium niobate [19]. In this thesis, the suppression of multi-access interference using a fiber nonlinear thresholder based on self-phase modulation effect was demonstrated.

Previously, my colleagues have successfully demonstrated an ultrashort-pulse optical CDMA test-bed [1]. However, it consists of only one transmitter and one receiver. To truly show the feasibility of CDMA operation, it is necessary to evaluate the CDMA performance in a multi-user environment. This dissertation documents the experimental results on back-to-back system measurements of a CDMA channel under multi-access interference. It provides an evidence for the possibility of error-free CDMA detection in a multiple-user environment.

To extend the application of optical CDMA for broadband fiber communications, an attempt was made to spectrally overlaying ultrashort-pulse CDMA scheme in a WDM system. The CDMA scheme complements the WDM technique and poten-

tially could provide additional transmission bandwidth to the existing WDM system. The feasibility of the hybrid WDM/CDMA concept was successfully demonstrated through system experiments in this thesis work.

1.3 Organization of This Dissertation

Chapter 2 describes the design and study of a passively mode-locked femtosecond fiber laser.

Chapter 3 presents the experimental results on complete fiber dispersion compensation for femtosecond pulse distortion-less transmission over a LAN compatible 10-km distance for CDMA data transmission using a dispersion compensating fiber and a femtosecond pulse shaper [20].

Chapter 4 describes the experimental and theoretical study on nonlinear effects in a 2.5-km dispersion-compensated fiber link for femtosecond pulse propagation [21].

Chapter 5 documents the system bit-error-rate (BER) measurements of an ultrashort pulse CDMA channel under multi-user interference. Effective interference suppression for CDMA operation was shown through the use of spectral phase coding and a fber nonlinear thresholder.

Chapter 6 presents the research results on a hybrid optical WDM/CDMA system. The feasibility of spectrally overlaying CDMA on WDM was demonstrated through back-to-back system measurements. The scaling of the experiments to Gb/s CDMA data rate was carried out. The experiments on timing skew compensation using a dispersion compensated fiber link for bit-parallel WDM data transmission indicates that optical WDM system and CDMA system may share the same transmission link during hybrid operation [22].

2. Femtosecond Fiber Laser for Ultrashort-Pulse Optical CDMA Systems

2.1 Introduction

Femtosecond lasers are important for high speed and broadband optical communications. Their short output temporal duration enables more information bits to be packed in the limited time-window for high speed TDM operation, and their wide output spectral bandwidth makes possible large number of users in the coherent CDMA systems.

In an ultrashort-pulse optical CDMA system, femtosecond laser is a key element, as it provides the phase coherence and wide spectral bandwidth necessary for the encoding-decoding operation. Depending on different network topology and transmission media, the requirements on the laser source are quite different. Nevertheless, the favorable characteristics generally include wide spectral bandwidth, high output pulse energy, high pulse repetition rate, and good stability, etc.. To facilitate the study on ultrashort-pulse optical CDMA, a stretched-pulse passively mode-locked fiber ring laser was constructed as the light source for most of the experiments reported in this thesis. The laser structure is adopted from the design by Tamura et. al. [23, 24]. Attentions were particularly paid to increase laser output power and reduce required pump power for reliable mode-locking operation.

2.2 Stretched-Pulse Passively Mode-locked Fiber Ring Lasers

Fig. 2.1 shows the schematic diagram of the fiber laser. Its modelocking is initiated by the fast saturable absorbtion action based on nonlinear polarization rotation. The unique features of this laser design over conventional simple ring structures include: the pulse-stretching cavity, which effectively reduces the soliton instability due to

periodical perturbations [25]; the net positive cavity dispersion, which helps increase pulse energy inside the cavity [23]; and a high power extraction port, which increases the laser efficiency by almost 50%.

As shown in Fig. 2.1, this laser was constructed as a ring resonator containing both normal dispersion erbium-doped fiber and anomalous dispersion standard single mode fiber. The dispersion per unit length for each segment is so large (Erbium fiber: $\sim +75$ ps^2/km and SMF: ~ -22 ps^2/km) that the dispersion is a dominant characteristic of the cavity. The strong alternating dispersion causes laser pulse width to be periodically stretched and recompressed (typically by a factor of 10 to 20) as it propagates around the cavity. The pulse maintains minimum pulse width only over portions of the length and hence accumulates less nonlinear phase shift.

Specifically, the ring cavity was constructed of 3.30m Corning SMF-28 (~ -0.023 ps^2/m), 0.54 m Corning Flexco-1060 (SMF: ~ -0.007 ps^2/m) and 1.27 m of Erbium-doped fiber (donated from MIT Lincoln Laboratories). The total cavity length is $\sim$ 5.11 m, which corresponds to a fundamental pulse repetition rate of 39.6 MHz. The dispersion of the isolator is dominated by the YIG crystal and estimated to be $\sim +0.003$ ps^2. The net cavity dispersion is therefore estimated to be positive ($\sim +0.0185$ ps^2). With this small net positive dispersion in the cavity, the available output pulse energy from the laser is larger than those produced in soliton regime (with negative cavity dispersion).

One challenge faced by common passively mode-locked fiber laser with positive cavity dispersion is that it has a relatively higher mode-locking threshold (normally $\sim$ 300 mW pump at 980 nm) than that of the soliton fiber lasers (normally around 80 to 100 mW). In order to decrease the pump threshold, we placed a fiber-pigtailed isolator inside the cavity ring, which forces unidirectional pulse propagation and facilitates the mode-locking self-starting from CW noises [24]. Another important strategy is to force the net cavity dispersion close to zero from the positive side. This has been found to be an effective way to reduce the mode-locking threshold in experiments. The erbium-doped fiber is pumped by solid-state diode laser that is capable of delivering

up to 200 mW pump power at 980 nm. With the careful adjustment of laser cavity dispersion , we achieved a modelocking pump threshold of less than 160 mW at 980 nm in experiments.

In order to increase the laser output power, an open air gap section was used as a high power extraction port. A polarization beamsplitter was placed in this open section. With the help of the fiber polarization controller before and after the open gap, the beamsplitter acts both as a time domain filter shortening the laser pulses and as an output coupler to make use of the rejected laser power. By replacing the normal fiber output coupler with this polarization power extraction port, we reduced the intracavity loss, and increased the overall laser efficiency. The polarization beamsplitter extracts around 50% of the laser power inside the cavity, which significantly increases the laser output pulse energy (by almost 50%). The coupling loss across the open air gap section can be further reduced through replacing the bulk beam splitter with a fiber pigtailed polarization beamsplitter. The coupling loss could be reduced from 2.5 dB to 0.7 dB.

The intrinsic jitter of the laser caused by the quantum noise of the Erbium-doped fiber amplification process is relatively small ($<$ 20 ppm with 10 Hz resolution) [26]. The output pulse stability of the fiber laser is mostly affected by the stability of the laser pump source and variations of environmental conditions. It has been reported that the stability (laser jitter) of a passively mode-locked fiber laser could be improved by almost a factor of 5 to 10 if the laser module was isolated from the air flow and temperature variations [27]. In our experiments, we also observed a significant improvement in laser output pulse stability when the whole laser module is isolated from the air flows. In addition, we found that the laser output noise was further reduced through replacing the water-cooling based Ti:sapphire pump laser with solid-state diode laser.

2.3 Performance of the Fiber Laser

The fiber laser is pumped by a single 980 nm laser diode. The modelocking is initiated through adjusting the fiber polarization controller. The laser mode-locking

pump threshold is less than $\sim$ 160 mW. After modelocking is started, the 980 nm pump power could be reduced to $\sim$ 120 mW without stopping the modelocking condition. The laser output power (fiber coupled) reaches 8 mW at 1550 nm when the pump power is 160 mW. The output spectrum (log scale) from the laser is shown in Fig. 2.2. We observed two peaks in the spectrum: one at 1560 nm and the other at 1592 nm. The spectral peak at 1560 nm has a full-width at half-maximum (FWHM) bandwidth of $\sim$ 30 nm and was used for most of ultrashort-pulse optical CDMA experiment.

The fiber laser output was dispersion compensated with a piece of dispersion compensating fiber. The pulse width was measured through optical intensity autocorrelation. Fig. 2.3 shows the autocorrelation trace of the laser output. The deconvolved pulse width is estimated to be $\sim$ 110 fs assuming secant-hyperbolic pulse shape. Due to the complicated spectral shape, it is hard to estimate the time-bandwidth-product (TBP) of the output pulses.

The fiber laser is operated with a repetition rate of 39.6 MHz, which corresponds to the total cavity length of 5.11 m. Fig. 2.4 shows the pulse train measured with a PIN detector and a 500MHz digital scope.

Finally, Table 2.1 shows the performance comparison between our current fiber laser (Fig. 2.1)and the laser previously built in the laboratory. Our current fiber laser shows a great improvement over the previous one. Part of the imporovement is also due to the use of a better Erbium-doped fiber (higher Erbium concentration and lower scattering loss) than that used in the previous laser.

Table 2.1
Fiber laser performance comparison.

Performance	Current fiber laser	Previous fiber laser
Modelocking pump threshold	$\leq$ 160 mW	$\sim$ 320mW
Output laser power at 1550 nm	$\sim$ 8 mW	$\sim$ 2 mW
Laser pulse repetition rate	40 MHz	33 MHz
Laser output spectral bandwidth	30 $\sim$ 40 nm	40 nm

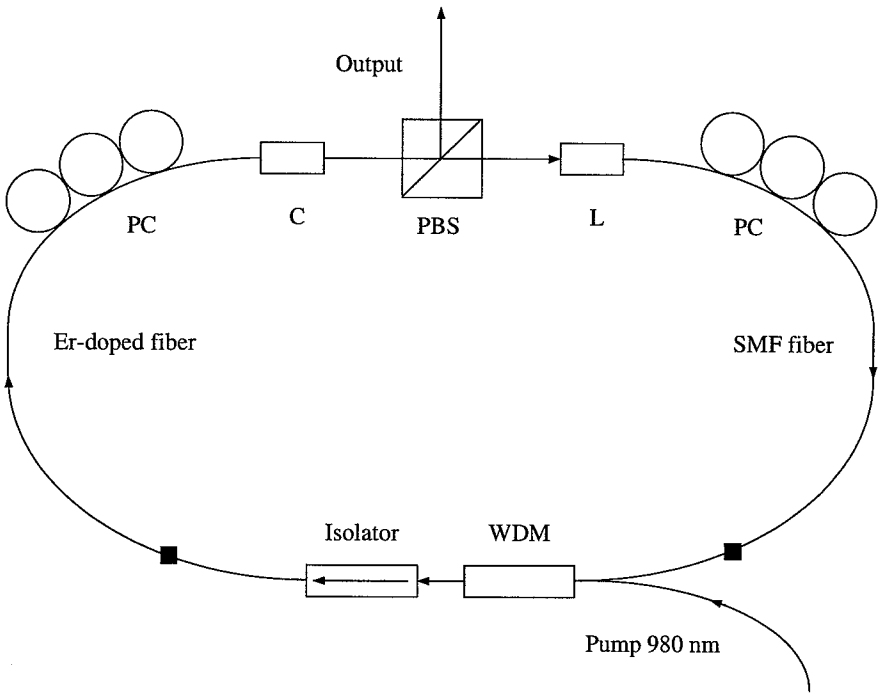

Fig. 2.1. Schematic diagram of the stretched-pulse passively mode-locking fiber ring laser with power extraction. PC: polarization controller; C: collimator; L: focusing lens; WDM: wavelength-division-multiplexed coupler; PBS: polarization beam splitter.

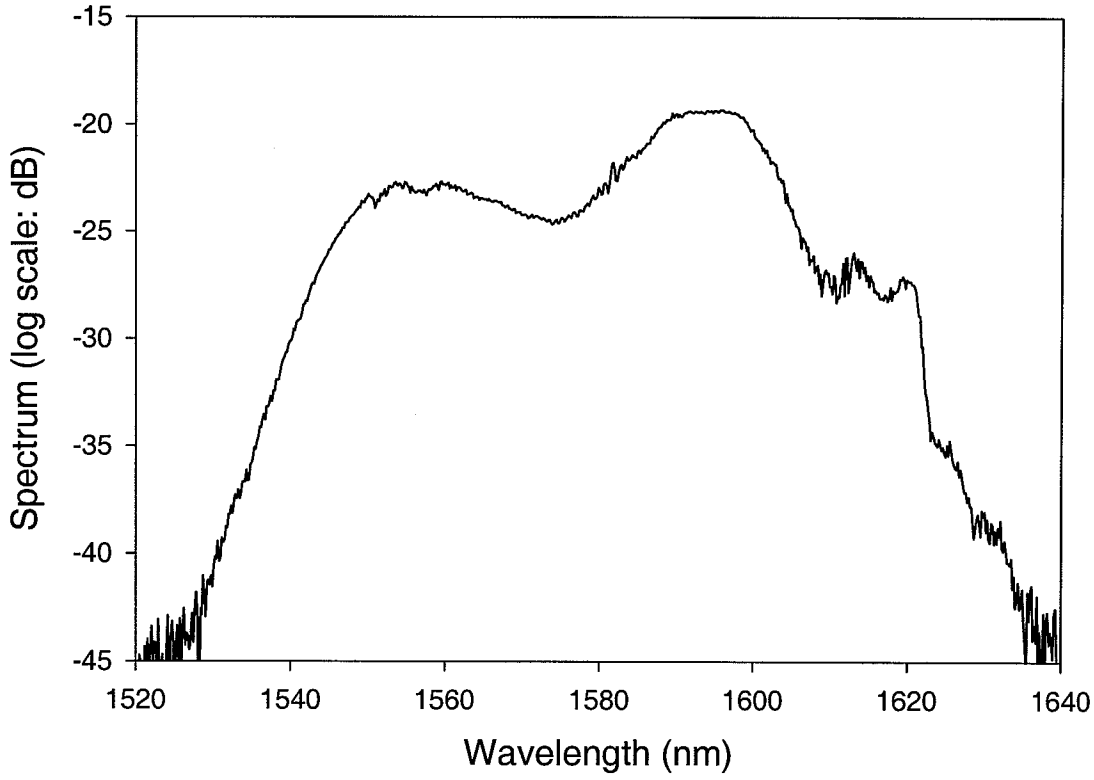

Fig. 2.2. Spectrum of the fiber laser output.

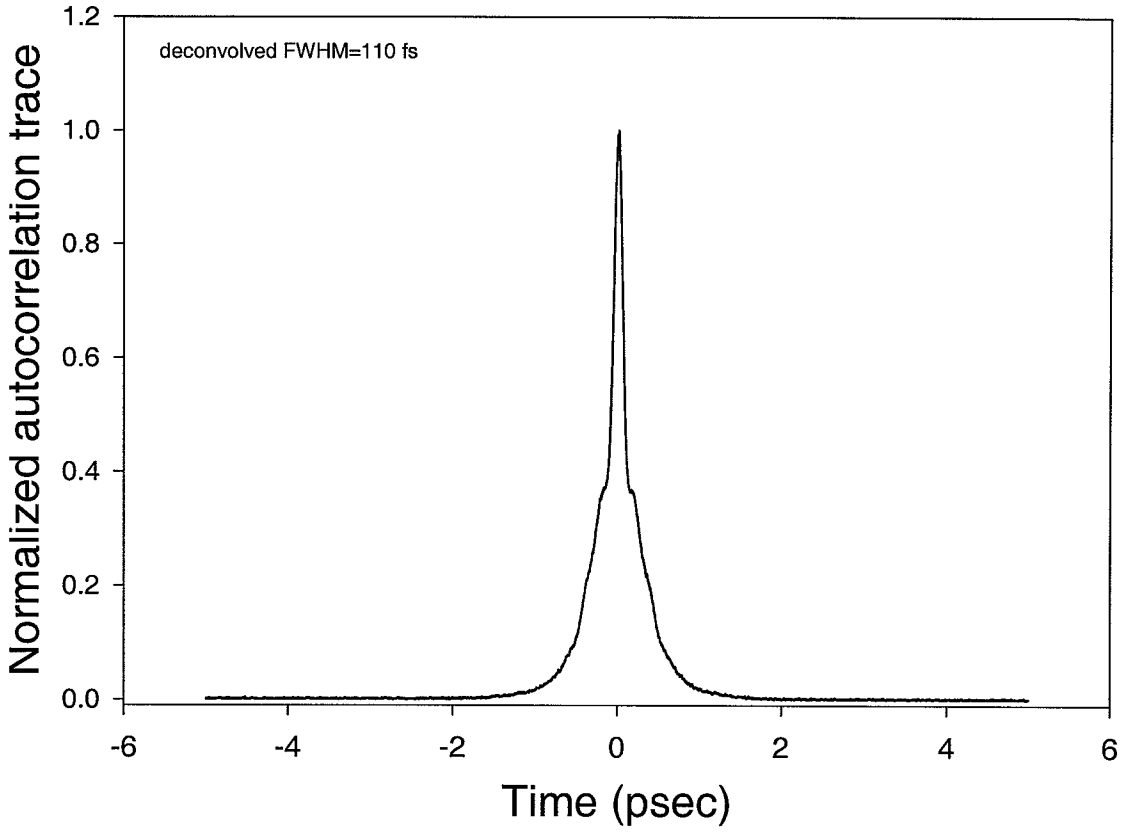

Fig. 2.3. Autocorrelation trace of the fiber laser output.

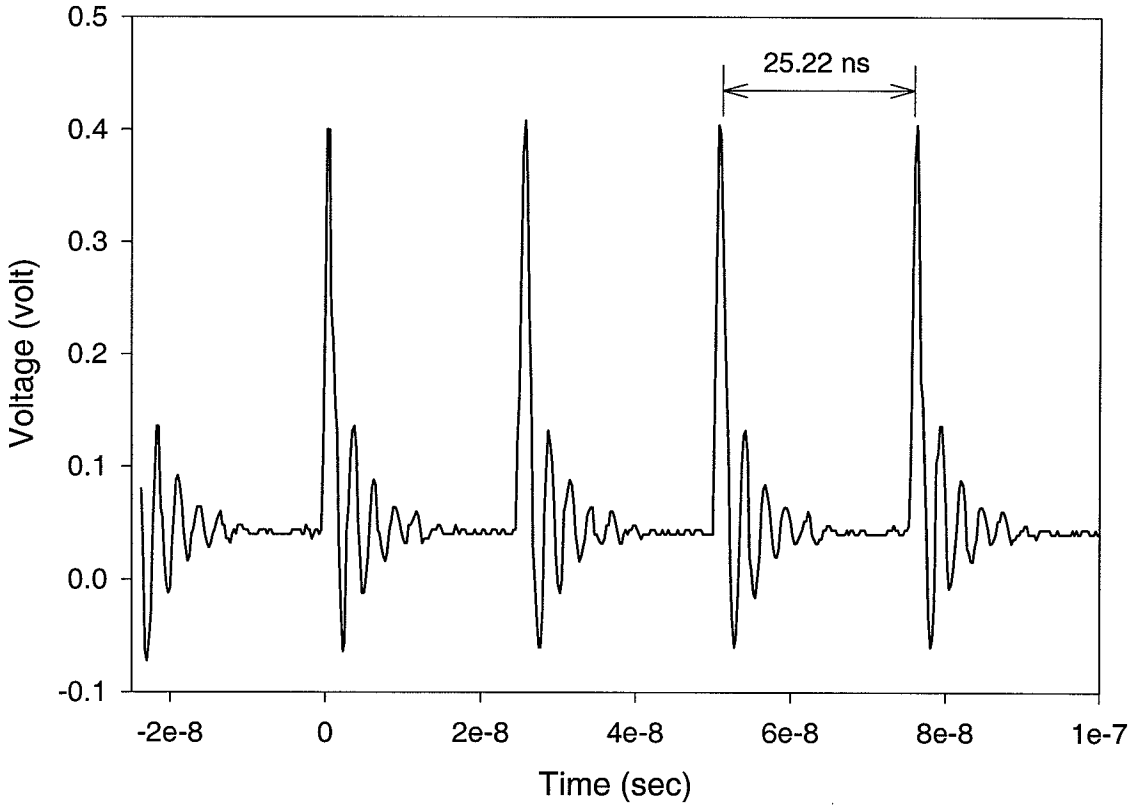

Fig. 2.4. Output laser pulse train measured from digital scope.

3. Complete Dispersion Compensation for 400-fs Pulse Transmission over a 10-km Fiber Link Using Disperison Compensating Fiber and a Programmable Pulse Shaper

Dispersion and dispersion compensation are key for high-speed lightwave transmission systems, such as time-division multiplexed (TDM) [28] and code-division multiple access (CDMA) systems [8, 29]. In femtosecond optical CDMA system, dispersion compensation is required for two major reasons. First, since CDMA scheme needs linear pulse transmission due to the phase sensitive encoding-decoding operation, we can not use soliton propagation. Second, any uncompensated dispersion will lead to severe degradation of the contrast between properly and improperly decoded pulses at the receiver end and degrades the system performance. Transmission of femtosecond pulses over kilometer distance, which is suitable for local area networks applications, requires the simultaneous compensation of both the 2nd order dispersion and the dispersion slope of the 1.3 μm single-mode fiber (SMF) link. A variety of dispersion compensating techniques have been proposed and investigated, e.g. mid-span spectral inversion [30, 31, 32], chirped fiber Bragg gratings [33, 34], bulk grating-and-lens pairs [35], and dispersion compensating fibers (DCF) [15, 36, 37, 38]. Among these compensating schemes, the DCF technique is especially attractive for femtosecond-pulse applications, since a carefully selected and precisely adjusted DCF can remove all the second order dispersion (GVD) and effectively suppress much of the third order dispersion (or dispersion slope) of the SMF. This made possible propagation of 500-fs pulses over a 2.5-km link [15] and 980-fs pulses over a 40-km fiber link [39] respectively with less than 2 times pulse broadening. However, the dispersion slope mismatch between the SMF and the DCF still leads to a small residual dispersion in

the compensated link. Although it was shown to be much lower ($\sim$ 4 times) than that of the dispersion shifted fiber (DSF) [15], this residual dispersion limits not only the fiber transmission distance but also the optical bandwidth, which in turn places a restrict on the usable code length (or the allowed number of users in CDMA systems). Further removal of this residual dispersion for distortion-less propagation of femtosecond pulses over longer distance with shorter pulsewidth becomes necessary.

Recently, a dispersion-shifted fiber (DSF) has been used in a 120-km SMF/DCF link to reduce the residual dispersion for $\sim$ 400 fs pulse transmission [40]. Nontheless, this technique requires very precise fiber length trimming and careful DCF selection. It is cumbersome and perhaps impractical to find such DCF that exactly matchs both the dispersion and dispersion slope of the SMF all the time in variety of applications. It is desirable to develop a technique capable of dynamically fine tuning and completely removing the residual dispersion without the strict requirement on DCF.

Previously, my collegues have demonstrated complete dispersion compensation for 500-fs pulse distortion-free transmission over a 2.5-km SMF/DCF link using a programmable pulse shaper [16]. In this chaper, we describe programmable and complete dispersion compensation for 400-fs pulses distortion-free transmission up to 10-km fiber distance using the pulse-shaper technique. The pulse shaper functions as a programmable spectral-phase equalizer and allows the complete removal of the residual dispersion in a nearly compensated fiber link with relaxed requirement on DCF and fiber length trimming. More importantly, the CDMA encoding operation and small dispersion compensation can be done in the pulse shaper at the same time. The figure of merit ($fiberlength \times pulsewidth^{-3}$) of our experiments is 8 times higher than previous 500-fs pulse transmission [16] and is 4 times higher than the 40-km link experiment [39].

3.1 Femtosecond Programmable Pulse Shaper

Grating-and-lens pulse shapers was originally introduced by Froehly [41] and was further developed by Weiner et. al. [9, 12, 13]. Such pulse shapers consisting of a pair of diffraction gratings, lenses, and a pulse shaping element. It is capable of picosecond

and femtosecond optical waveform synthesis through spectral filtering (by a spatial mask) in its mid-plane (called Fourier plane) and in the meantime introduces no temporal dispersion. Fig. 3.1 shows the diagram of the programmable pulse shaper used in our experiment. A programmable 128-pixel liquid crystal phase modulator (LCM) array was placed at the Fourier plane. The frequency components of the pulses are spatially dispersed across the Fourier plane by the first grating and lens, and recombined by the second identical grating/lens pair. A pair of zeroth-order half-wave plates were placed before and after the LCM to rotate the input polarization from horizontal to vertical and vice versa. This is necessary because while the gratings require horizontal polarization for good diffraction efficiency, the LCM is designed for vertical polarized beam. In general, the output pulse emerging from the pulse shaper is the Fourier transform of the mask phase function provided by the LCM.

The main modification of our pulse shaper over a conventional one [9] is that the input and output ports are fiber pigtailed ($\sim$1.5 m SMF at each end) with connectors. The major advantage of the fiber-connectorized ports is the flexibility and ease of hooking up any optical fiber devices without requiring beam alignment. The down sides are the fiber pigtails scramble polarization and introduce a small amount of dispersion. Therefore, a pair of polarization controllers are placed at each end to adjust the polarization state for best throughput. To compensate the dispersion of the fiber pigtails, the position of the second grating is adjusted so that the pulse shaper is in the minimum dispersion configuration, i.e. when the constant phase is applied across the LCM, the pulse shaper itself introduces no dispersion at all. If carefully designed and aligned, the fiber-pigtailed pulse shaper (with a liquid crystal phase modulator (LCM) in place) has a very low insertion loss (5.3 dB fiber-to-fiber) and is capable of high-fidelity pulse transmission when constant phase is applied onto the LCM.

To have good spectral-phase equalization performance, the spectral resolution of the pulse shaper has to be small enough to resolve physical features as small as the pixel width (100 μm) of the phase modulator. In other words, the focused Gaussian

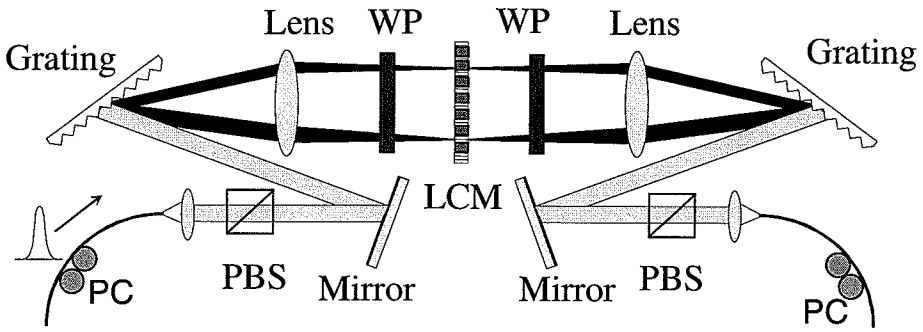

Fig. 3.1. Schematic diagram of programmable pulse shaper. LCM, liquid crystal modulator; WP, wave plate; PBS, polarization beam splitter; PC, polarization controller.

beam radius w_0 has to be smaller than pixel width [13]. Meanwhile, the pulse shaper must be able to accept the input spectral bandwidth within the window of the phase modulator ($\Delta x = 12.8\ mm$). The Gaussian beam radius w_0 and the spatial dispersion of the pulse shaper α can be expressed as

$$w_0 = \frac{cos(\theta_{in})}{cos(\theta_d)} \left(\frac{F\lambda}{\pi w_{in}} \right) < 100\ \mu m \tag{3.1}$$

$$\alpha = \frac{\Delta x}{\Delta \lambda} = \frac{F}{d\, cos(\theta_d)} < \frac{12.8\ mm}{15\ nm} = 0.85\ mm/nm, \tag{3.2}$$

where θ_{in} is input beam angle, θ_d is the diffracted angle, F is the lens focal length, w_{in} is the input beam radius, and d is the grating period. Furthermore, θ_{in} and θ_d have to satisfy grating equation given as

$$sin(\theta_d) = \frac{\lambda}{d} - sin(\theta_{in}). \tag{3.3}$$

In our experiment setup, we use d=1100 lines/mm, F=190 mm. Although w_0 and α can be calculated from the above equations with measured w_{in}, θ_{in} and θ_d, they can also be estimated by matching numerical simulation results with experimental results.

3.2 Dispersion Compensation Using Femtosecond Pulse Shaper

The fiber dispersion can be characterized by expanding the group delay per unit length $T(\omega)$ (inverse of the group velocity) around the center frequency ω_c as

$$T(\omega) = \frac{1}{v_g} = \frac{d\beta}{d\omega} = \beta_1 + \beta_2(\omega - \omega_c) + \frac{\beta_3}{2}(\omega - \omega_c)^2 + ... \tag{3.4}$$

where $\beta_m = (\frac{d^m \beta}{d\omega^m})_{\omega=\omega_c}$ represents the mth order dispersion. It is also often expressed as the variation in group delay with respect to the wavelength λ as

$$D(\lambda) = \frac{dT(\lambda)}{d\lambda} = D(\lambda_c) + D'(\lambda_c)(\lambda - \lambda_c) + ... \tag{3.5}$$

D and D' are closely related to β_2 and β_3 [15]. They represent the 2nd order and the 3rd order dispersion respectively. When a femtosecond pulse travels through a standard SMF ($\beta_2 < 0$) at 1.55μm, higher frequency components travel faster than the

lower frequency components. The output pulse width can be broadened significantly (up to hundreds of picosecond after a several kilometer link). When a well selected DCF is concatenated with SMF, it recompressed the broadened pulses after the SMF close to its original input pulse width. However, because the 3rd order dispersion of the DCF normally does not match the SMF exactly, it leads to an asymmetric pulse broadening and distortion in the form of an oscillating tail.

Since the spectral components of the femtosecond pulse are spatially dispersed across the Fourier plane of the pulse shaper, the residual dispersion can be removed conveniently and programmably by adding appropriate quadratic and cubic phases (and potentially higher order terms) in the pulse shaper through simply applying the required voltage pattern onto the LCM array. The quadratic and cubic phases provided by pixel #n of the LCM can be formulated as

$$\Phi_n = \frac{\phi_2}{2}(n - \frac{N}{2})^2\delta\omega^2 + \frac{\phi_3}{6}(n - \frac{N}{2})^3\delta\omega^3 + ... \tag{3.6}$$

where $n = 1, 2, 3, ..., N$ and N is the total pixel number. ϕ_2 (in ps^2) and ϕ_3 (in ps^3) are the second- and third-order phase curve parameters respectively, and $\delta\omega$ is the angular frequency increment (which is 1.1×10^{11} rad/sec in our case) between adjacent pixels. Note that the pixels are numbered in such way that higher frequency components impinge on higher number pixels. Since the phase variation is discretely sampled over the entire N pixels, where N is large ($N = 128$ in our experiment), the moderate phase curve can be considered as continuously sampled. Therefore exact phase correction is feasible. Note that the fiber dispersion induced spectral phase can be expressed as

$$\phi(\omega) = \phi_0 + \tau(\omega - \omega_c) + \frac{\beta_2}{2}L(\omega - \omega_c)^2 + \frac{\beta_3}{6}L(\omega - \omega_c)^3 + ... \tag{3.7}$$

Comparing Eq. 3.6 with Eq. 3.7, one will find the relations between the phase curve parameters (ϕ_2 and ϕ_3) and the fiber dispersion $\beta(\omega)$ as $\beta_2 = \frac{\phi_2}{L}$ and $\beta_3 = \frac{\phi_3}{L}$.

3.3 Experiments and Results

The 10-km dispersion compensated fiber link is constructed by concatenating a 9.1-km standard 1.3μm SMF (Corning SMF-28) and a 1.50-km dispersion-compensating

fiber (donated from Bell Laboratories). The total length of the fiber link is 10.6 km. No specific attempt was made in the selection of the DCF to exactly match the dispersion slope of the SMF. The length ratio between SMF and DCF was adjusted so that the pulse distortion after propagating through the fiber link closes to minimum. The total insertion loss of the fiber link including fiber splicing loss is ~6 dB.

The experimental setup for compensating residual dispersion in the pulse shaper is shown in Fig. 3.2. A femtosecond fiber laser was used to generate 110-fs pulses with a repetition rate of 40 MHz. After an interference filter, the laser spectrum was centered at 1559 nm with $\sim$ 11 nm bandwidth (FWHM). The output power of the filter is $\sim$ 400 μW. The laser pulses were then launched into the 10-km fiber link. A chirp-pulsed fiber amplifier was connected after the fiber link to increase the signal power. After the fiber amplifier, a programmable pulse-shaper was used to compensate the residual dispersion in the fiber link. A 128-pixel LCM was located in the Fourier plane of the pulse shaper. The spectral dispersion of the LCM is $\sim$ 0.12 nm/pixel and the spatial width of each pixel is 100 μm. The pulse shaper introduces zero dispersion when a constant phase is applied across the LCM. The output pulse width was measured through optical intensity autocorrelation based on non-collinear second-harmonic generation with accuracy of $\pm$ 20 fs.

The experiment was performed by first measuring the laser pulsewidth after the pulse shaper without connecting the 10-km fiber link . The fiber amplifier was directly connected at the end of the interference filter. The output average power from the amplifier is $\sim$ 500 μW. Fig. 3.3 shows the optical spectrum after the pulse shaper. Due to the gain narrowing in the fiber amplifier, spectral bandwidth was reduced to $\sim$ 8 nm. The corresponding autocorrelation trace after the pulse shaper is shown in Fig. 3.4 when a constant phase was added across the LCM. It indicates that input pulse to the 10-km fiber has a pulsewidth of 390 fs (FWHM assuming secant-hyperbolic pulse shape). Considering the 8 nm spectral bandwidth, this gives the time-bandwidth product (TBP) of $\sim$ 0.38, which is close to the transform-limited TBP.

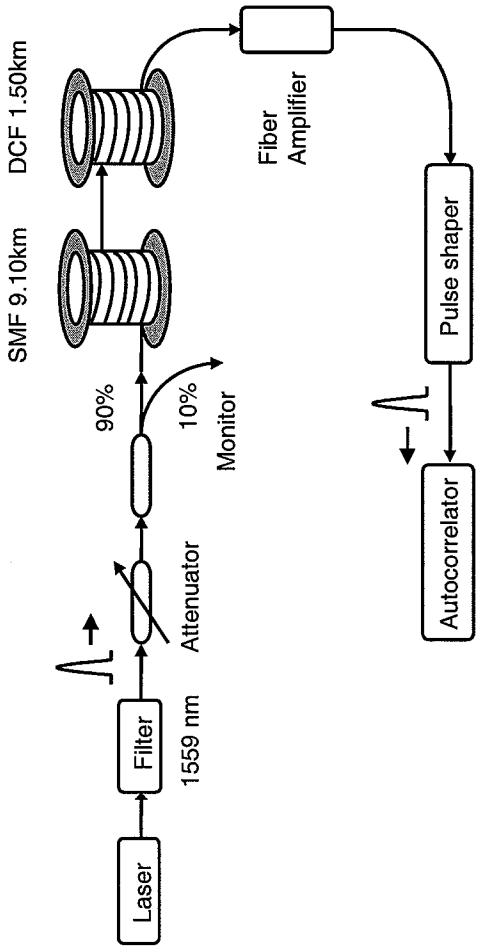

Fig. 3.2. Experiment setup for compensating dispersion using a pulse shaper and DCF.

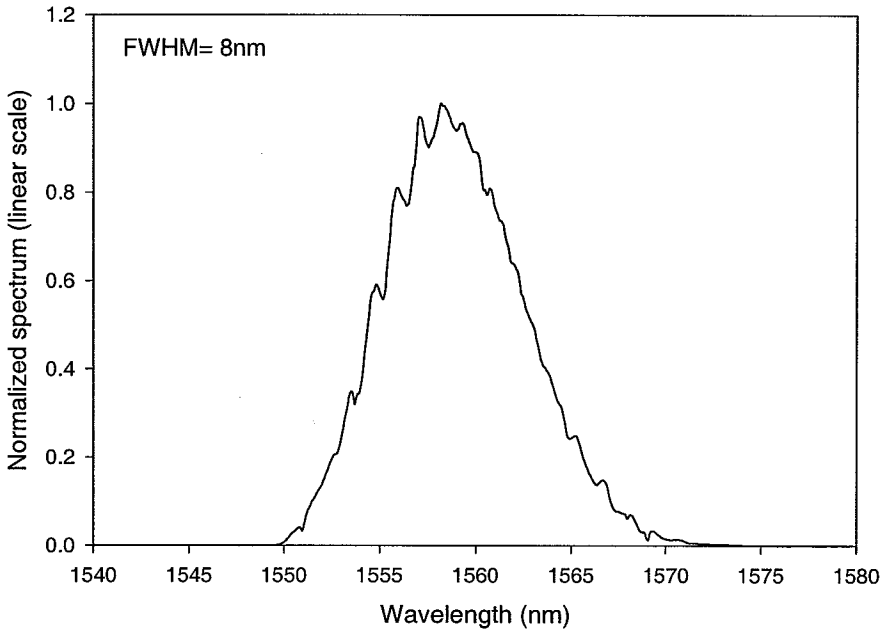

Fig. 3.3. Spectrum after the pulse shaper.

The femtosecond pulse transmission over the 10-km SMF/DCF fiber link was then measured by inserting the compensated fiber link between the interference filter and fiber amplifier as shown in Fig. 3.2. The input power in the fiber link was adjusted to be $\sim$ 200 μW so that the power at the input of the fiber amplifier is the same for experiments with and without the 10-km fiber link. No nonlinearity was observed in the fiber link. When the constant phase was applied to the LCM, we measured an output pulse width of $\sim$ 950 fs (deconvolved FWHM) after the pulse shaper as shown by curve (a) in Fig. 3.5. Compared to the input pulsewidth, we observed the pulse broadening due to the small residual dispersion and dispersion slope in the 10-km fiber link. Note that the estimated pulse width after the SMF alone is $\sim$ 1.2 ns,

which means the DCF is actually compensating 99.9% of the pulse broadening. To remove the remaining dispersion, we iteratively applied quadratic and cubic phases onto the LCM to restore the original input pulse. Fig. 3.6 shows the optimized phase curve applied to the LCM.

Fig. 3.5 shows the autocorrelation trace after the pulse shaper when the optimized quadratic (curve (b): $\phi_2 = 0.050$ ps^2) and the cubic phase (curve (c): $\phi_3 = -0.25$ ps^3) were applied onto the LCM separately and together (curve (d)). A deconcolved FWHM pulse width of $\sim$ 405 fs (assuming secant-hyperbolic pulse shape) has been obtained when the complete dispersion (both optimized quadratic and cubic phase) was applied onto the LCM. Compared to the input autocorrelation measurement, it shows that the pulse shaper has virtually removed all the residual dispersion in the fiber link and has essentially recompressed the laser pulses back to their input pulse width. From ϕ_2 and ϕ_3, we estimated that the residual dispersion in the compensated fiber link of $\beta_2 = 0.0047$ ps^2/km ($D = -0.0036$ ps/km/nm) and $\beta_3 = -0.0236$ ps^3/km ($D' = -0.0142$ ps/km/nm^2). The residual 2nd order dispersion compensated by the pulse shaper corresponds to $\sim$ 2.5 m SMF length deviations from its optimal value. The residual 3rd order dispersion β_3 in our 10-km fiber link is equivalent to that measured in our previous 2.5-km fiber link [37]. However, the cubic phase corrected in our experiments by the pulse shaper is 8 times higher than that demonstrated in the previous work.

3.4 Discussion

We have experimentally demonstrated programmable and almost complete dispersion compensation, which allows distortion-free transmission for 400-fs pulse over a 10-km fiber link using the DCF and a femtosecond pulse shaper. The capacity of the phase correction in the pulse shaper is mainly limited by the finite pixel width on the LCM (which leads to discrete phase sampling) and the finite spectral resolution of the setup. Considering the LCM spectral dispersion ($\sim$ 0.12 nm/pixel, spatial width of each pixel is 100 μm) and the spectral resolution of the pulse shaper ($\sim$ 0.16 nm), we estimated that the maximum cubic phase that can be compensated in our pulse

shaper is $|\phi_3| < 0.45$ ps^3 [16]. In our 10-km dispersion compensated fiber link, the compensated residual cubic phase is $\phi_3 = -0.25$ ps^3. There is still leeway that allows us to further increase the transmission distance or reduce the required precision for fiber length trimming.

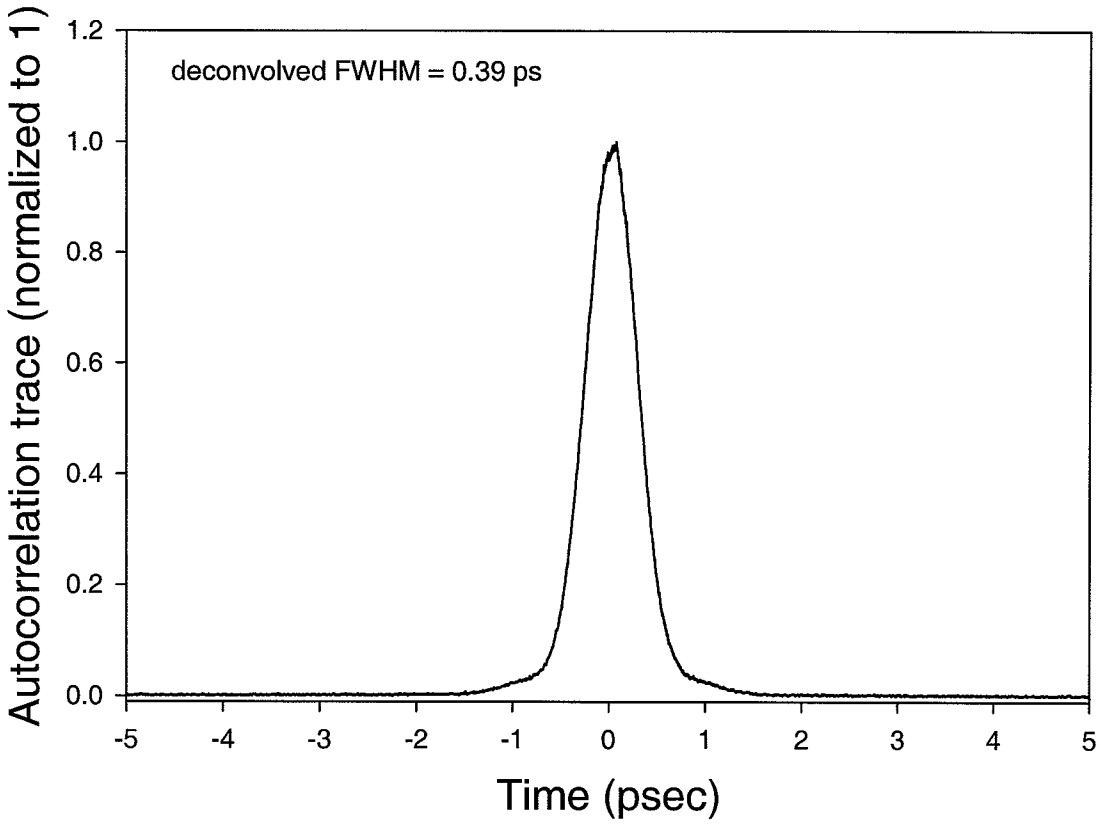

Fig. 3.4. Autocorrelation trace after the pulse shaper when the 10 km fiber link is not present.

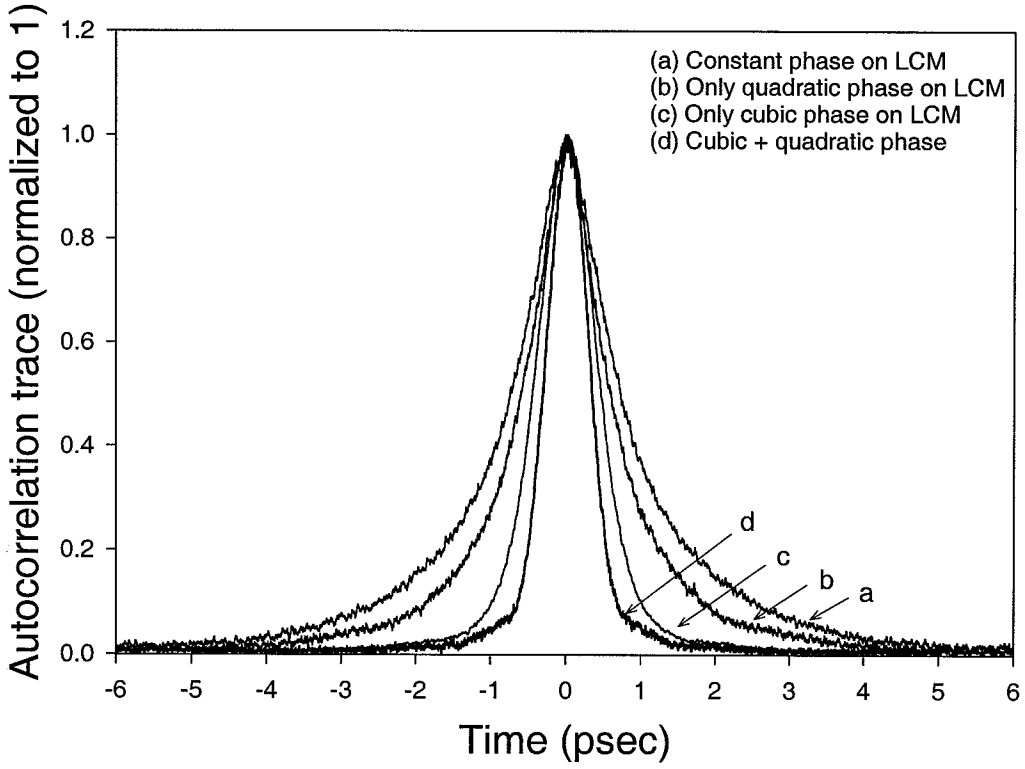

Fig. 3.5. Autocorrelation measurement after the pulse shaper with 10 km fiber link included. (a) with constant phase on the LCM (deconvolved FWHM = 950fs), (b) with optimized quadratic phase only on the LCM (deconvolved FWHM = 770fs), (c) with optimized cubic phase only on the LCM (deconvolved FWHM = 550fs), (d) with both optimized quadratic and cubic phase on LCM (deconvolved FWHM = 405fs).

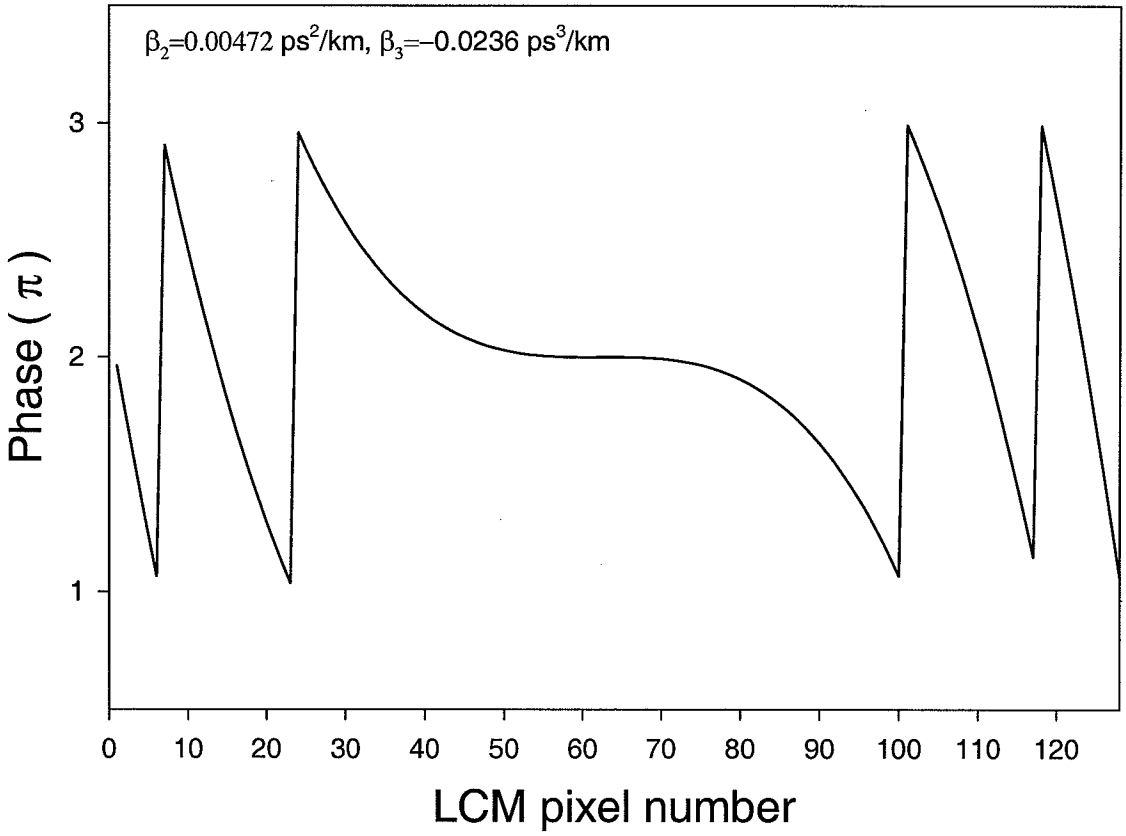

Fig. 3.6. Optimized phase curve applied to the LCM.

4. Nonlinear Effects in Dispersion Compensated Fiber Links

4.1 Introduction

In a dispersion compensated fiber link, the performance of femtosecond pulse transmission is no longer limited by the fiber group velocity dispersion (GVD) but by higher order residual dispersion and fiber nonlinear effects. The dominant nonlinear effect in a CDMA fiber link is the self-phase modulation effect (SPM) — a phenomenon caused by the nonlinear dependence of the refractive index on pulse intensity. The accumulated nonlinearity must remain small in order to avoid the degradation in the CDMA encoding-decoding operation. On the other hand, the CDMA system calls for greater received power for error-free nonlinear thresholding. The amount of pulse energy allowed in the dispersion compensated link is eventually limited by the interaction of SPM and the fiber dispersion. It becomes necessary to investigate the nonlinear effects in such links to better understand the power limitation in an ultrashort pulse optical CDMA system. It is noted that nonlinear effects in a dispersion compensated fiber link is also crucial for high speed TDM pulse transmission system.

Previously, the SPM effects on the dispersion compensated link were studied only in the sub-10 to 100 picosecond range [42, 43, 44, 45, 46]. As the pulse width of the transmission link is continuously decreased into femtosecond regime as in the case of ultrashort-pulse CDMA system, the pulse broadening and recompression factor will be drastically increased. The effect of the third order dispersion will also be significantly increased. Detailed analysis on the interaction among SPM and the second and the third-order dispersion in the fiber link for femtosecond pulse transmission is necessary.

In this chapter, we discuss the nonlinear effects in such dispersion compensated fiber links where the femtosecond pulse is largely stretched and recompressed. The

goal is to determine the onset of the fiber nonlinearity for femtosecond pulse transmission and the power levels suitable for optical CDMA networks. Considering the low pulse repetition rate in our experiments, we focused our analysis on isolated femtosecond pulses. In particular, both numerical and experimental study of SPM effects are presented for 400-fs pulse transmission over a 2.5-km SMF/DCF link with an input pulse energy ranging from 15 to 150 pJ. The SPM effects in a pre-compensated link and a post-compensated link are compared.

4.2 Numerical Analysis of SPM Effects in a Dispersion Compensated Fiber Link

We first analyze the effects of self-phase modulation on femtosecond pulse transmission over a SMF/DCF link through numerical simulations. The model used for our simulations is shown in Fig. 4.1. We modeled the post-compensated fiber link by connecting DCF at the end of SMF. By simply reversing the order of SMF and DCF, i.e. the SMF is connected at the end of the DCF; we can model a pre-compensated fiber link. In our analysis, we assumed ideal second-order dispersion compensation, since the DCF can be adjusted to provide an exactly equal and opposite second-order dispersion to that of the SMF in experiments. A small residual third-order dispersion caused by a minor dispersion slope mismatch between the SMF and the DCF will also be considered to match the experimental conditions. The SPM induced degradation in the pulse recompression process is analyzed by evaluating the output pulse broadening after the SMF/DCF link as a function of the input optical power.

The nonlinear Schrodinger equation (NLSE), modified to include higher order dispersion, has been successful in accurately modeling pulse propagation in single-mode fibers in many diverse applications [47, 48]. It can therefore be employed with confidence for dispersion-compensated fiber links. In our analysis, we used the normalized NLSE

$$i\frac{\partial U}{\partial \xi} = sgn(\beta_2)\frac{1}{2}\frac{\partial^2 U}{\partial \tau^2} + \frac{i\beta_3}{6 \mid \beta_2 \mid T_0}\frac{\partial^3 U}{\partial \tau^3} - N^2 \mid U \mid^2 U \exp(-\alpha \xi L_d) \qquad (4.1)$$

where $\xi = \dfrac{z}{L_d}$ and $\tau = \dfrac{t - z/v_g}{T_0}$ represent the normalized distance and retarded time

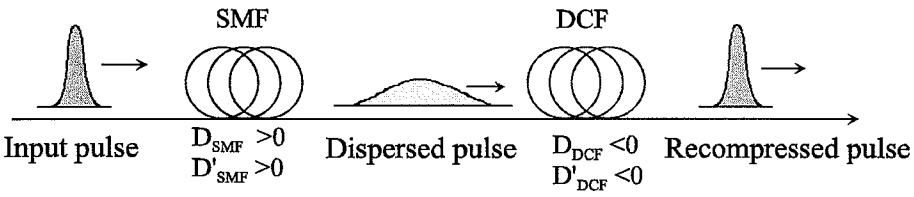

Fig. 4.1. Simulation model for a post-compensated link. Dispersion compensating fiber acts as a dispersion compensator. D and D' are the dispersion and dispersion slope parameters of the fiber.

variables respectively. U is the normalized amplitude such that the amplitude of pulse envelope equals to $\sqrt{P_0}\exp(-\frac{\alpha z}{2})U(z,\tau)$. P_0 is the peak power of the input pulse and T_0 is the input pulsewidth. β_2 and β_3 are the dispersion and dispersion slope parameters of the fiber respectively. α is the fiber loss coefficient. The dispersion length $L_d = \frac{T_0^2}{\mid \beta_2 \mid}$ and the nonlinear length $L_{NL} = \frac{1}{\gamma P_0}$ provide the length scales over which the dispersion and the nonlinear effect become important respectively. γ is the nonlinear coefficient and is related to n_2 and the effective core area A_{eff} by $\gamma = \frac{n_2\omega_0}{CA_{eff}}$. The ratio of L_d to L_{NL} gives the nonlinearity factor $N^2 = \frac{L_d}{L_{NL}} = \frac{\gamma P_0 T_0^2}{\mid \beta_2 \mid}$. The index parameter N is normally used to compare the importance of the dispersion and SPM effects in the fiber [49]. Larger N, contributed either from larger input peak power at a fixed pulsewidth or from larger pulsewidth at a fixed peak power, corresponds to larger SPM effects in the fiber link. When $N = 1$, the peak power and pulsewidth support the fundamental soliton for $\beta_2 < 0$. In our model, we consider the second and third-order dispersion effects and include SPM as the source of nonlinear terms. Other higher order nonlinear effects such as the Raman contribution to the nonlinear refractive index and the shock term have been neglected. Since the input power level in our analysis is below that for soliton generation ($N < 1$) , the effect of SPM is moderate. As long as we avoid very short pulses ($\leq$ 100 fsec), the Raman effect and shock term, which are usually smaller than SPM, should be negligible. Brillouin scattering has also been assumed to be suppressed since the optical bandwidth, on the order of terahertz for sub-500-fs pulses, is orders of magnitude larger than the Brillouin linewidth.

The split-step Fourier transform algorithm is adopted in our simulation. To simplify the problem and extract the essential properties of the interaction between the SPM effect and the fiber dispersion, we first confined our attention to the most dominant dispersion and nonlinear term, i.e. only the second-order dispersion and SPM effect are included in the simulation. SMF provides anomalous GVD ($\beta_2 < 0$) and DCF provides normal GVD ($\beta_2 > 0$). We adjust the link dispersions $\mid \beta_2 L \mid$ to be equal and opposite for the SMF and DCF, and we take the ratio of nonlinearity

to dispersion $\mid \frac{\gamma}{\beta_2} \mid$ to be the same for SMF and DCF. The amount of SPM and fiber dispersion is characterized by the nonlinearity factor N and dispersion length L_d respectively. The single isolated input pulses are considered to be Gaussian shaped.

Fig. 4.2 shows the pulse shape of the input and compressed output pulse for different values of input peak power ($N^2 = 0.01,\ 0.09,\ 0.25$) from a post-compensated fiber link of a total length $L = 200L_d,\ 1000L_d,\ 2000L_d$ respectively. The figure clearly shows the deterioration in the pulses as N is increased. There is almost no effect for $N^2 = 0.01$. At $N^2 = 0.09$, SPM starts to degrade the pulse recompression. At $N^2 = 0.25$, the SPM disturbs the dispersion balance rapidly. The size of the SPM effect is large when N is high. Hence the SPM effect gives an upper bound on the maximum input peak power that can be used for the ultrashort-pulse transmission in the post-compensated fiber link. Fig. 4.2 also shows the output pulses for the isolated input pulse after they propagate through a pre-compensated link of total length $L = 200L_d,\ 1000L_d$, and $2000L_d$ for $N^2 = 0.01, 0.09$ and 0.25 respectively. The pulses are recompressed back nicely even after a long distance ($2000L_d$) with high input peak power at a fixed input pulsewidth ($N^2 = 0.25$). The output maintains roughly the same pulse shape as the input pulse and displays no appreciable SPM induced dispersion balance degradation for $N^2 < 0.25$. Fig. 4.3 shows the plot of output peak intensity from both compensating scenarios with respect to the propagation distance for different values of N.

For the pre-compensated link, the output peak power doesn't change much when N is less than 0.5. Combined with the result of Fig. 4.2, it indicates the SPM effect in a pre-compensated link is almost negligible at these power levels. Comparing the curves for $N = 0.1$ and $N = 0.5$ for the post-compensated link, we can see that there is almost 50% peak power reduction when N is increased to 0.5. As the propagation distance is extremely large corresponding to a very substantial broadening of the pulse in SMF, the output peak power in the SMF falls substantially. Much (but not all) of the nonlinearity occurs at the beginning of the fiber due to the substantial pulse broadening and reduction in the peak intensity as the pulse propagates. For

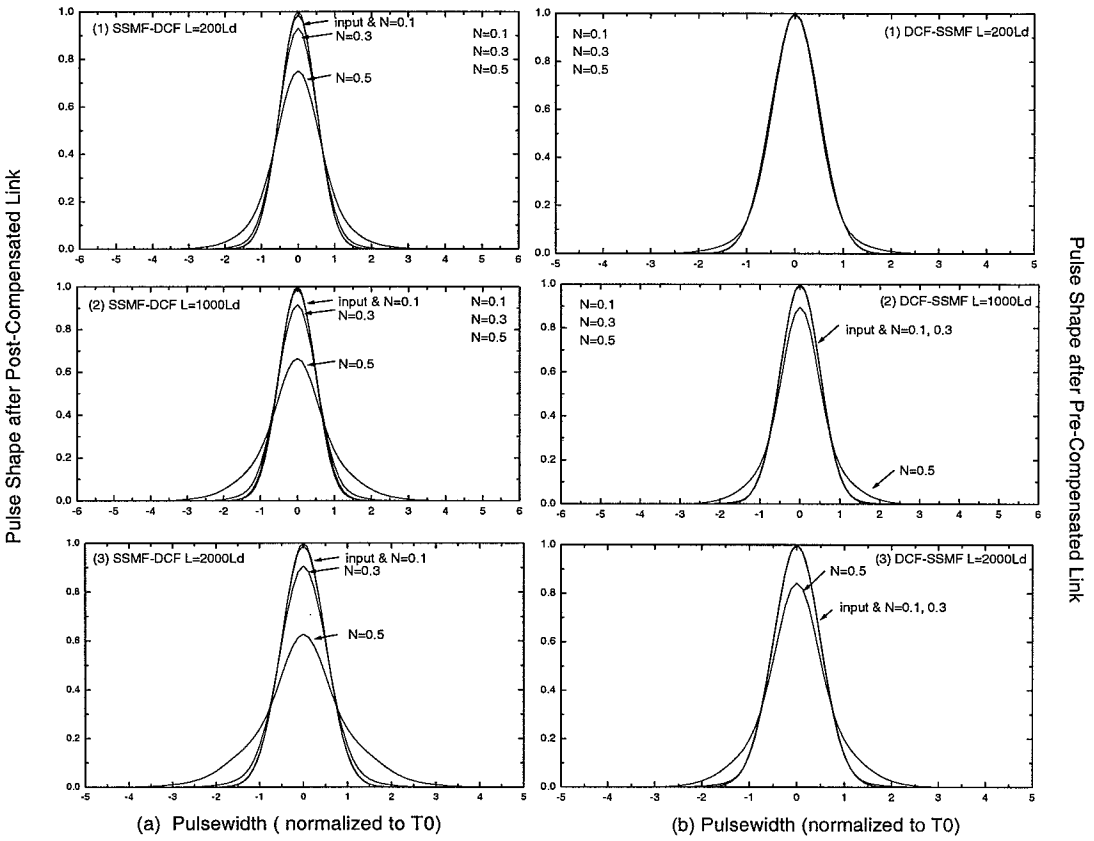

Fig. 4.2. The simulated output pulse shape from (a) post-compensated link (b) pre-compensated link

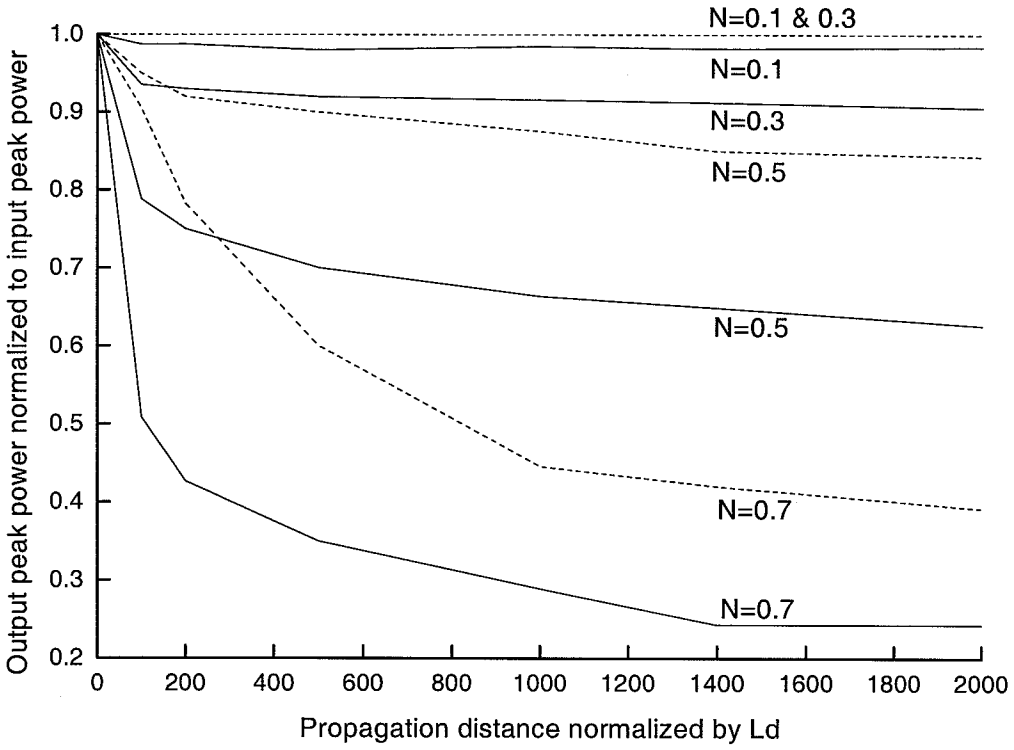

Fig. 4.3. The simulated output pulse intensity for a post-compensated link (solid line) and a pre-compensated link (dashed line) when $N = 0.1$, 0.3, 0.5, and 0.7.

$N > 0.5$ the compressed pulse deteriorates rapidly, since the input pulse breaks into two parts in the SMF- one propagates as a soliton and the other as a dispersive wave. The dispersive waves are compensated at the DCF but the soliton part is completely spread out. The net result is a very rapidly distorting pulse. Clearly, the input power must be kept sufficiently low to avoid such effects for good data transmission. The above simulation provides us the general views of the SPM effect on the dispersion compensated link when large pulse stretching and recompression occurs. By appropriately scaling using the nonlinear factor N and dispersion length L_d, we can apply the simulation results to a wide range of input pulsewidths and fiber lengths. Note that the soliton energies ($N^2 = 1$) for pulse durations of 100 fsec, 500 fsec, and 1 psec in SMF are 435 pJ, 87 pJ and 43.5 pJ respectively. Therefore, in this ultrashort pulsewidth range, good transmission corresponding to $N^2 < 0.09$ is possible for energies well into the pJ range, which should be more than sufficient for high quality communications even with a post-compensated link.

Another important feature of the SPM effect worth noticing is its different behavior in a post-compensated and a pre-compensated link. It is due to the asymmetric distribution of the anomalous GVD and normal GVD in the compensated link. In the post-compensating scenario, SPM introduces positive chirp in the propagating pulses and partially balances the effect of negative dispersion in the SMF. The pulse broadening process is therefore slowed down. Since the size of the SPM effect is peak intensity dependent, the accumulated SPM effect is increased in the post-compensated link. In contrast, since the SPM effect accelerates the pulse broadening process in the initial DCF ($\beta_2 > 0$) of a pre-compensated link, the accumulated SPM is reduced due to the more rapidly reduced peak power. Thus, the pre-compensated link is more robust than a post-compensated link when input power is high. The output pulses from a pre-compensated link maintain a reasonable pulse shape and peak power even after a fiber link of 2000 L_d when N^2 is 0.25. The power limit for a pre-compensated link thus could be further increased to nearly a hundred pico-Joule for the femtosecond-pulse transmission.

We noted that our simplified simulation includes only the second-order dispersion and the SPM term, where the parameters of DCF are the same as those of SMF except the sign of the dispersion. Usually, the ratio of nonlinear coefficient γ to fiber dispersion β_2 is less for real DCF than for SMF [50, 51]. Therefore, our simulation is conservative and overestimates the effect of SPM in the DCF. In our further analysis described in the following, we chose appropriate parameters for SMF and DCF from our measurements and includes the third-order dispersion, in order to match the simulation to the experiments.

4.3 Experiment and Simulation with Higher Order Dispersion

To verify our theoretical analysis, we performed experiments in a dispersion compensated link for isolated femtosecond pulses with a fixed pulsewidth at different power levels. The 2.5-km transmission link consisting of a 2.06-km single-mode fiber (AT&T 5D) and a 0.44-km DCF was used in our experiment [15]. The SMF has $D \approx 17$ ps/km/nm (or $\beta_2 \approx -22$ ps^2/km) and $D' \approx 0.05$ ps/km/nm^2 ($\beta_3 \approx 0.13$ ps^3/km) at 1550 nm taken from the spectral interferometry measurement [15]. The DCF has $D \approx -76$ ps/km/nm (or $\beta_2 \approx 98$ ps^2/km) measured by time-of-flight technique and a negative dispersion slope $D' \approx -0.2$ ps/km/nm^2 ($\beta_3 \approx -0.50$ ps^3/km) [15, 37]. The length ratio between SMF and DCF is optimized for a nearly zero overall second-order dispersion. The total loss of the 2.5-km link, including splicing and connector losses, was measured to be 3 dB.

The experimental setup is shown in Fig. 4.4. The 62-fs pulses were generated from a stretched-pulse passively mode-locked fiber ring laser adopted from the reference [23] at a repetition rate of $\sim$ 33 MHz. The laser output was spectrally sliced by an interference filter ($\lambda_0 = 1559$ nm, FWHM = 9.8nm) and amplified by a fiber amplifier [6] with output average power up to 5 mW. The input pulses were nearly bandwidth-limited (time-bandwidth product $\sim$ 0.32) with pulsewidth of FWHM $\sim$ 400 fsec assuming secant-hyperbolic pulse shape and centered on $\lambda_0 = 1559$ nm. We adjusted the average power of the input pulses by a fiber pigtailed attenuator. The amount of SPM introduced in the transmission link can then be adjusted. The output pulse

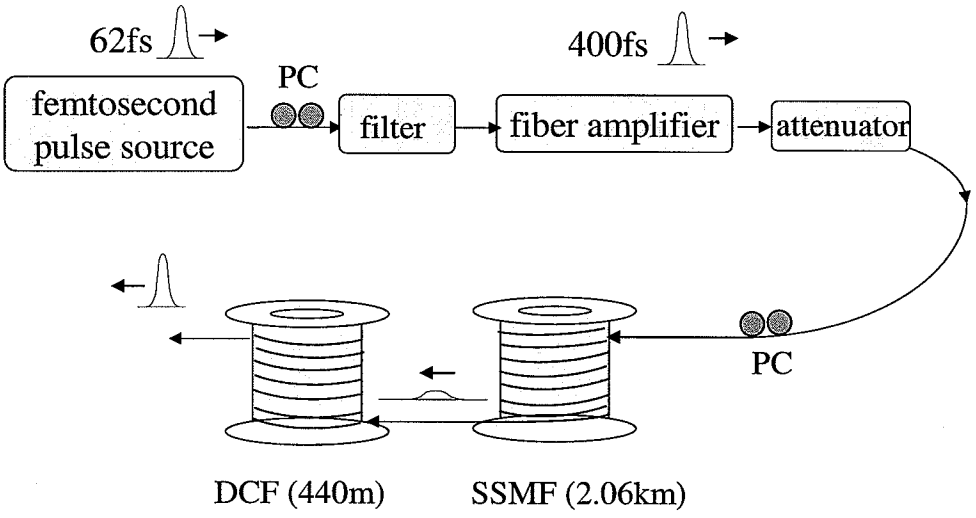

Fig. 4.4. Experiment setup for SPM effects on a 2.5-km dispersion compensated link. PC, polarization controller; Filter, interference bandpass filter; fiber amplifier, chirped pulse fiber amplifier with maximum 20 dB gain; attenuator, fiber attenuator.

intensity auto-correlation was measured at an input average power ranging from 500 μW up to 3.5 mW. A fiber polarization controller was employed to optimize the polarization of input pulses for maximum autocorrelation signal. The input and output spectra of the link were compared through an optical spectrum analyzer (OSA). SPM effects on both pre-compensated (DCF-SMF) link and post-compensated (SMF-DCF) links were investigated.

Fig. 4.5 shows the input and output auto-correlation traces of the post-compensated link (SMF-DCF) with input average powers of 0.6 mW, 1.0 mW, 2.2 mW and 3.0 mW respectively. All the output auto-correlation traces shown were normalized to unit amplitude. The corresponding auto-correlation traces for the pre-compensated link are shown in Fig. 4.6. The power dependent output auto-correlation FWHM (not deconvolved) is shown in Fig. 4.7, from which the actual pulsewidths can be estimated by dividing the auto-correlation FWHM by 1.55 (assuming secant-hyperbolic pulse shape).

The experiment is repeatable as indicated by the stable input pulsewidth ($\sim$ 400 fs) under each input power level shown in Fig. 4.7. It is clear that the SPM effect behaves in different ways in the post-compensated and pre-compensated cases as expected from our previous simulation results. For the post-compensated scenario, input pulses were initially stretched to $\sim$ 200 ps (calculated) in the SMF and recompressed back to $\sim$ 500 fs (FWHM) in the subsequent DCF under linear low power operation ($<$ 500 μW or $N < 0.09$). The small output pulse broadening is due to the residual dispersion slope of the compensated link. The pulse broadening and recompression ratio is estimated be over 300. As the input power is increased from 500 μW to 3.5 mW with a corresponding pulse energy up to $\sim$ 0.15 nJ, the pulse recompression was degraded by the SPM effect significantly. The link output pulsewidth was broadened by almost a factor of three as shown in Fig. 4.7. As the input average power was further increased beyond $\sim$ 3.5 mW (not shown), a soliton component was generated in SMF, which was then broadened tremendously in the subsequent DCF. For the pre-compensated scenario, the positive dispersion of DCF balanced the

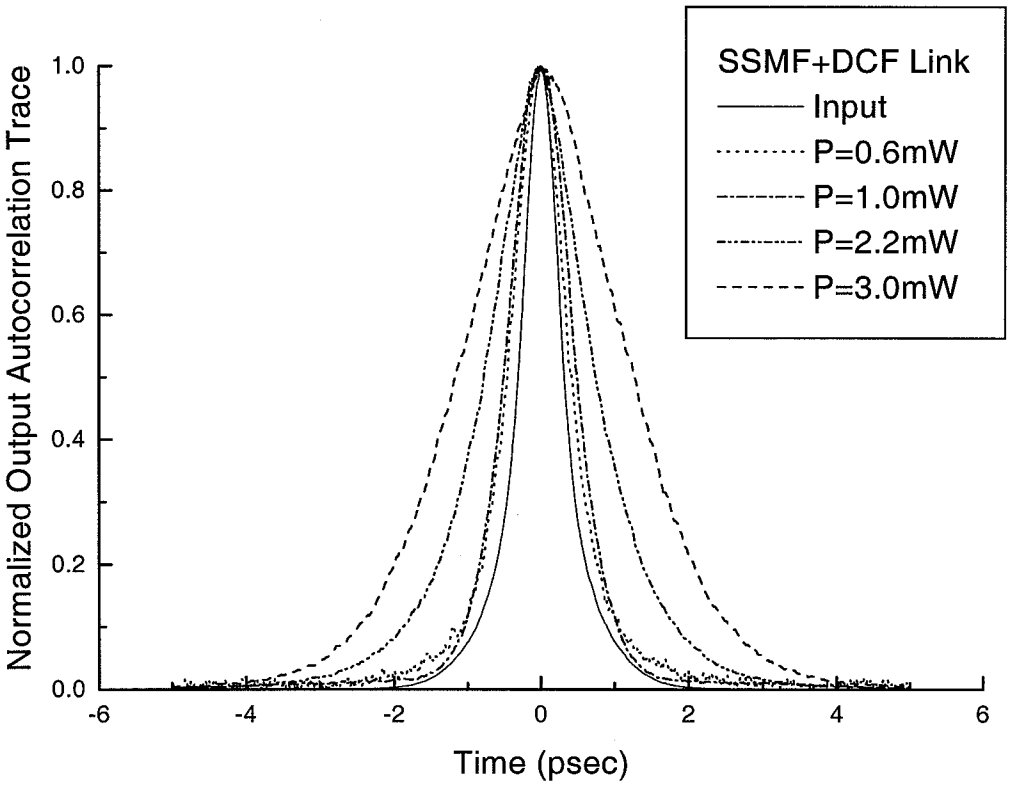

Fig. 4.5. Measured intensity auto-correlation traces of input and output pulses after a 2.5-km post-compensated link (normalized to unit amplitude). The input average power $P = 0.6$ mW, 1.0 mW, 2.2 mW, and 3.0 mW with pulse repetition rate of 33 MHz. The input pulse FWHM is 400 fsec (solid line).

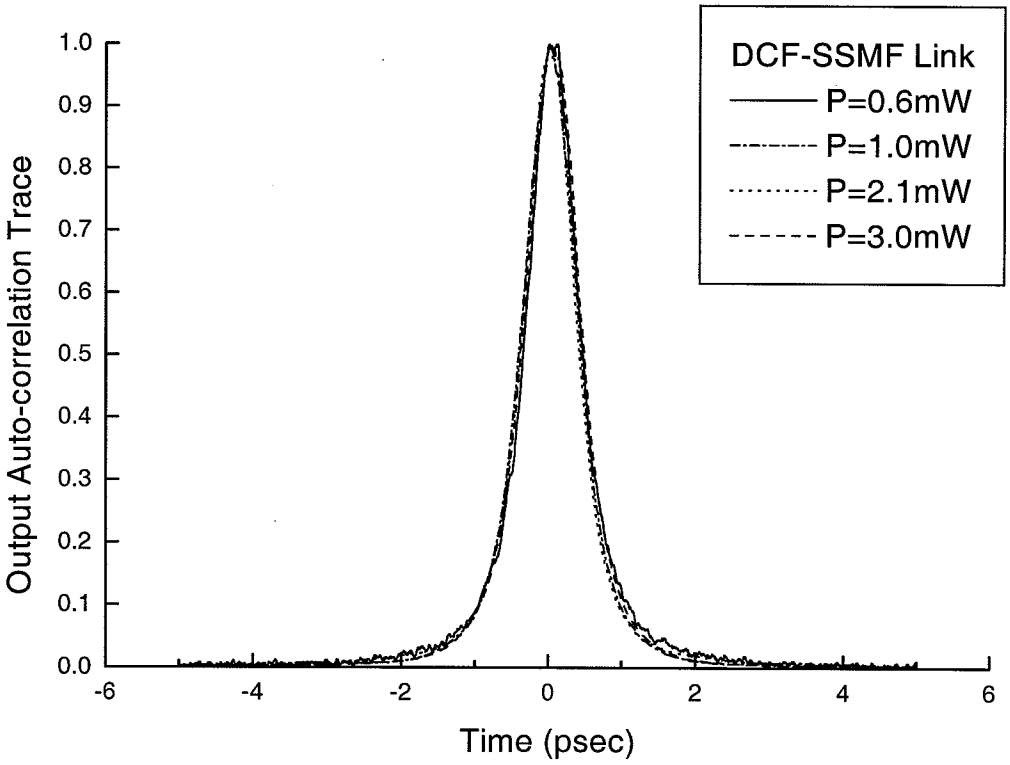

Fig. 4.6. Measured intensity auto-correlation traces of input and output pulses after a 2.5-km pre-compensated link (normalized to unit amplitude). The input average power $P = 0.6$ mW, 1.0 mW, 2.1 mW, and 3.0 mW with pulse repetition rate of 33 MHz. The input pulse FWHM is 400 fs (solid line).

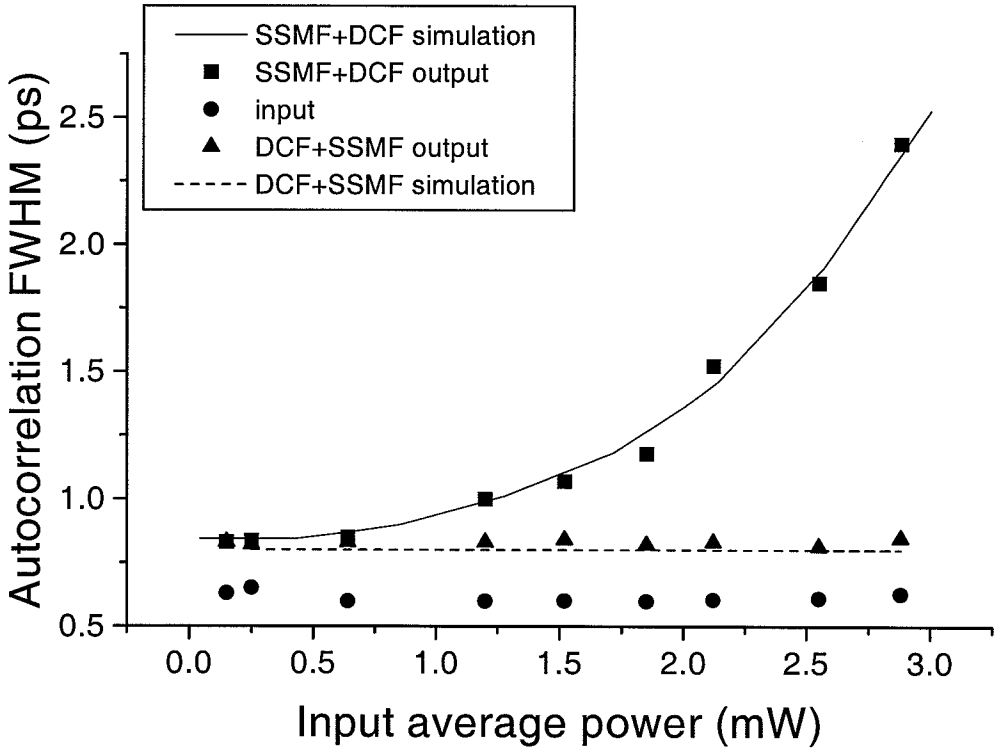

Fig. 4.7. Measured and simulation results of input and output pulse broadening due to the SPM effect in a 2.5-km dispersion compensated link. The input pulse FWHM is 400fs.

negative dispersion of SMF and recompressed the pulse back at the output end of the transmission link nicely. With input average power increased to as high as 3.5 mW, the output pulse width of the link doesn't change much. The SPM effect on the output pulses from a pre-compensated link is insignificant until much higher power levels.

Fig. 4.8 shows the input and output spectra width for the pre- and post-compensated links. The input spectrum FWHM maintains the same $\sim$ 6.5 nm for each measurement. A dramatic spectral narrowing effect was observed from the output of the post-compensated link when the input power was increased. By comparing the output spectra of the compensated link to the output spectra directly from SMF, we observed that the spectral narrowing effect mainly (almost $\sim$ 90%) occurred in the SMF portion of the link. Subsequent to the SMF, the optical pulse is negatively chirped and SPM leads to additional small spectral narrowing in the DCF. The latter result is consistent with the spectral narrowing effects previously observed from the propagation of negatively chirped input pulses over a normal dispersion fiber only [52]. For the pre-compensated scenario, the output spectrum is slightly broadened when input power is increased up to 3 mW. Again, the effect of SPM on the output of the pre-compensated link is minor. For comparison, the results of the simulation, which will be discussed later in details, are also shown in Fig. 4.7 and Fig. 4.8. Experimental data are in excellent agreement with the simulation.

To further investigate the actual output pulse shape of the link, we also measured the cross-correlation traces. The reference pulse of the cross-correlation measurement was obtained from the fiber laser directly by splitting part of the laser output (FWHM = 62 fsec) into the reference measurement path. In the cross-correlation measurement, the path of the signal pulses (2.5-km fiber) is much longer than that of the reference pulses ($\sim$ 2 m of free space). The #N output pulse was correlating with #N+387 instead of the #N reference pulse. The accuracy of the cross-correlation measurement is therefore limited to $\sim \pm 100$ fsec by the laser timing jitter effects. In this experiment, the input is again maintained at 400 fsec (FWHM) for each measurement assuming

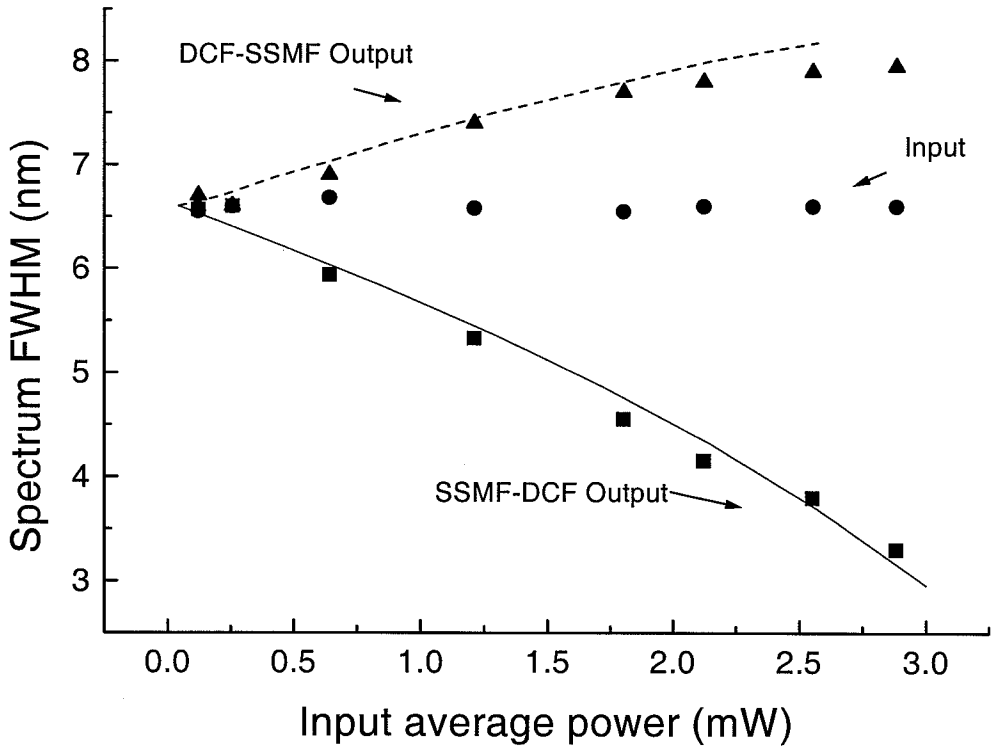

Fig. 4.8. Measured and simulation results of input and output pulse spectrum FWHM due to the SPM effect in a 2.5-km dispersion-compensated link (solid line, dashed line: simulation results; circle, triangle, square: experiment data).

the secant-hyperbolic pulse shape. Fig. 4.9 shows output cross-correlation traces from the post-compensated link when input power is 0.5 mW, 2.0 mW and 3.2 mW respectively. It was shown that the output pulse displays asymmetric oscillating tail even at low power. It indicates a small residual third-order dispersion of the concatenated link as expected from the previous experiment by my colleagues [15]. Note that when the input power reaches as high as 3.2 mW, the output pulses are significantly broadened and deteriorated. Fig. 4.10 shows one example of a cross-correlation trace for the pre-compensated link when the input average power is as high as 3.2 mW. In contrast, we observed that the output pulse broadening in the pre-compensated link is quite small.

As a further metric, we also measured the SPM induced signal peak-power reduction by recording the input and output peak signals using the lock-in amplifier during the cross-correlation measurements. The experimental result is shown in Fig. 4.11. We observed almost 50% peak-power drop in the post-compensated link due to the SPM effect. These cross-correlation results are quantitatively consistent with previous auto-correlation measurements.

To compare the experimental results with our theoretical analysis, we have performed numerical simulations using the experimental conditions. In contrast to the previous simulation where only the second-order dispersion and SPM are included, the third-order dispersion of SMF and DCF were included in this simulation. The SMF has $D = 17$ ps/km/nm (or $\beta_2 = -22$ ps^2/km) and $D' = 0.05$ ps/km/nm^2 at 1550 nm and the DCF has $D = -76$ ps/km/nm (or $\beta_2 = 98$ ps^2/km) and dispersion slope $D' = -0.2$ ps/km/nm^2. A small residual third-order dispersion was included in the analysis. The transmission link loss is mainly due to the fiber connector and splicing loss under our conditions. Therefore, the distributed fiber attenuation was lumped into connector loss in our model. The length of SMF and DCF in the simulation was taken as 2.06 km and 0.44 km respectively. The nonlinear coefficient γ of SMF was taken to be 1.2 W^{-1}km^{-1}, which is roughly consistent with measured results from the references [53, 54]. The nonlinear coefficient γ of DCF was taken to

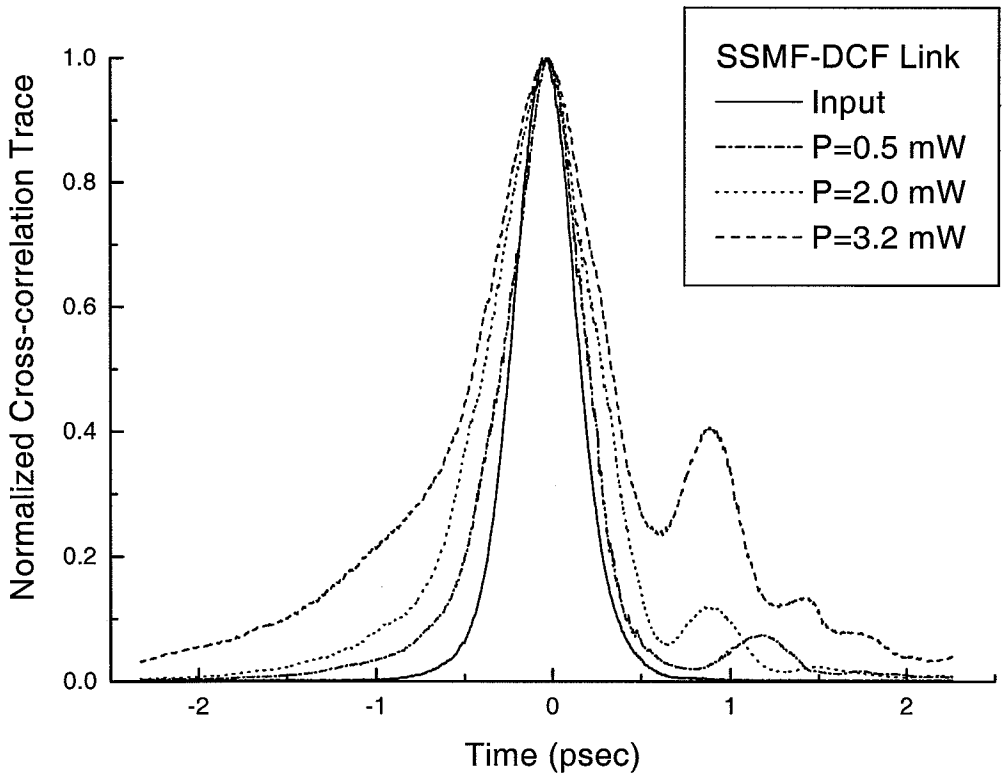

Fig. 4.9. Measured cross-correlation traces of input and output pulses after a 2.5-km post-compensated link (normalized to unit amplitude). The input average power $P = 0.5$ mW, 2.0 mW and 3.2 mW with pulse repetition rate of 33 MHz. The input pulse FWHM is 400 fsec (solid line).

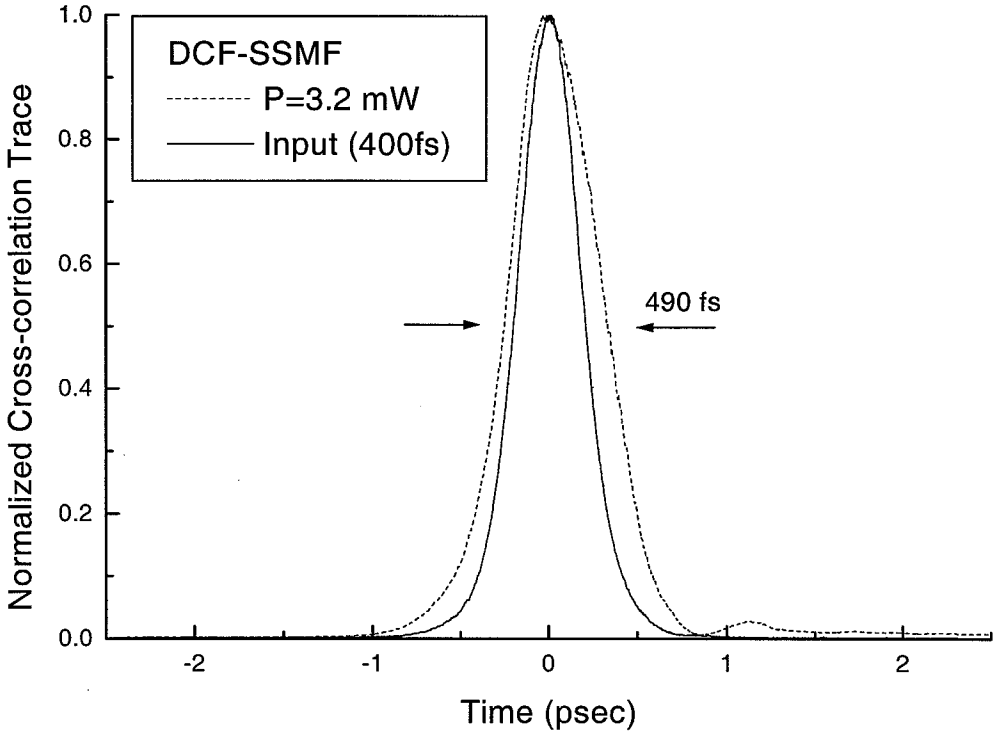

Fig. 4.10. Measured cross-correlation traces of input and output pulses after a 2.5-km pre-compensated link (normalized to unit amplitude). The input average power P is 3.2 mW at the pulse repetition rate of 33 MHz. The input pulse FWHM is 400 fsec (solid line).

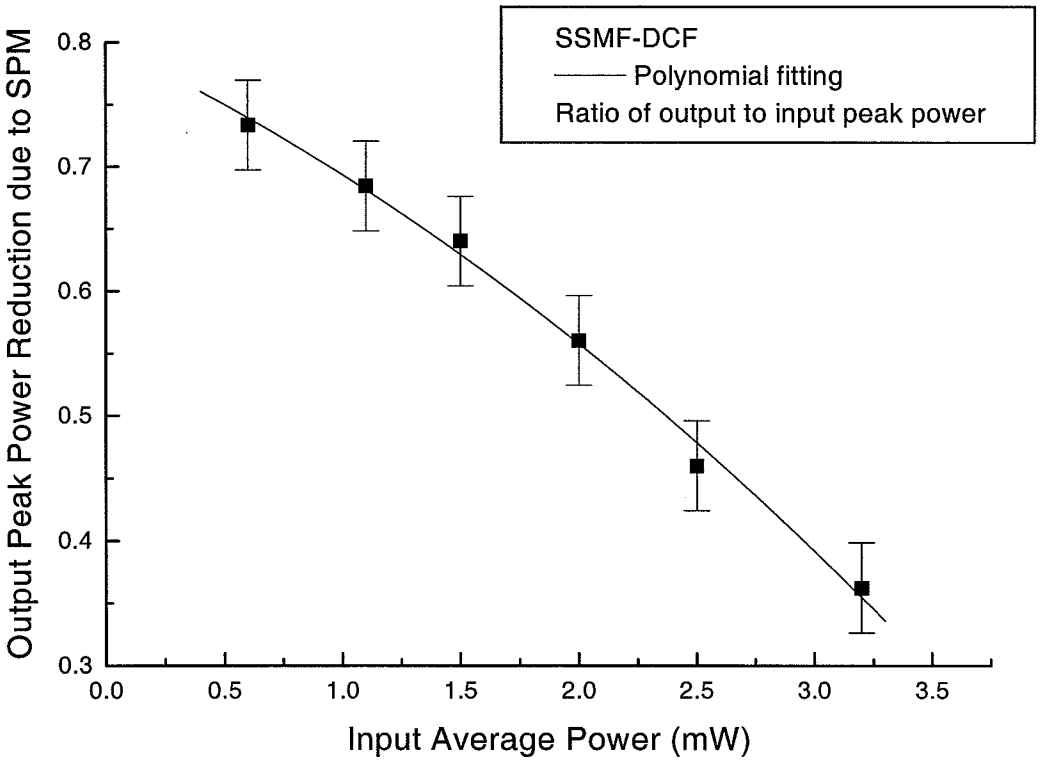

Fig. 4.11. The peak-power ratio between the output and input pulses for the post-compensated link. The output peak power used in calculating the power ratio is two times as that of the actual measurement to account for the 3 dB loss of the transmission link. The input pulse FWHM is 400 fsec (solid line).

be twice that of the SMF. The ratio of nonlinear coefficient γ to fiber dispersion D for the DCF is comparable with reported values of other DCFs [50, 51]. These simulation parameters were confirmed by matching the simulated output spectra from either the SMF (2.06 km) or the DCF (0.44 km) alone with the corresponding measured spectra respectively. The input pulsewidth in the simulation is 400 fsec with the secant hyperbolic pulse shape assumed.

Fig. 4.12 shows the simulation results of the SPM effects on the output pulse shape of a post-compensated link where the DCF is connected at the end of the SMF. Fig. 4.13 shows SPM effects on the output pulse-shape of a corresponding pre-compensated link. The output pulse shape after the transmission link under each input peak power level was normalized to unit amplitude. The pre-compensated link simulation is the same as that for post-compensated link except that the order of SMF and DCF is reversed. In both cases, the small broadening in the output pulses under low power operation is due to the third-order dispersion mismatch of SMF and DCF, which can be identified from the oscillating cubic tail of the output pulse shape. This simulation result is consistent with our cross-correlation trace measurement. The overall calculated pulse shape from the post-compensated link shows a great resemblance with the measured cross-correlation traces under various input powers. The measured cross-correlation traces from the pre-compensated link show less cubic tail than the corresponding simulation results, which is probably due to a small DCF nonlinear parameter mismatch between the experiments and the simulations. We also calculated the FWHM of the simulated output pulse autocorrelation traces to compare with our measurements shown in Fig. 4.7. The calculated output spectra FWHM is shown in Fig. 4.8. The simulation results match the experiment data very well. This confirms that our theoretical approach is valid for the analysis of SPM effect on a dispersion compensated link in the femtosecond regime when the pulse stretching and recompression is extremely large ($\sim$ on the order of several hundreds). By comparing this simulation with the previous simulation results which only consider the second-order dispersion and SPM, we noted that the second-order dispersion is

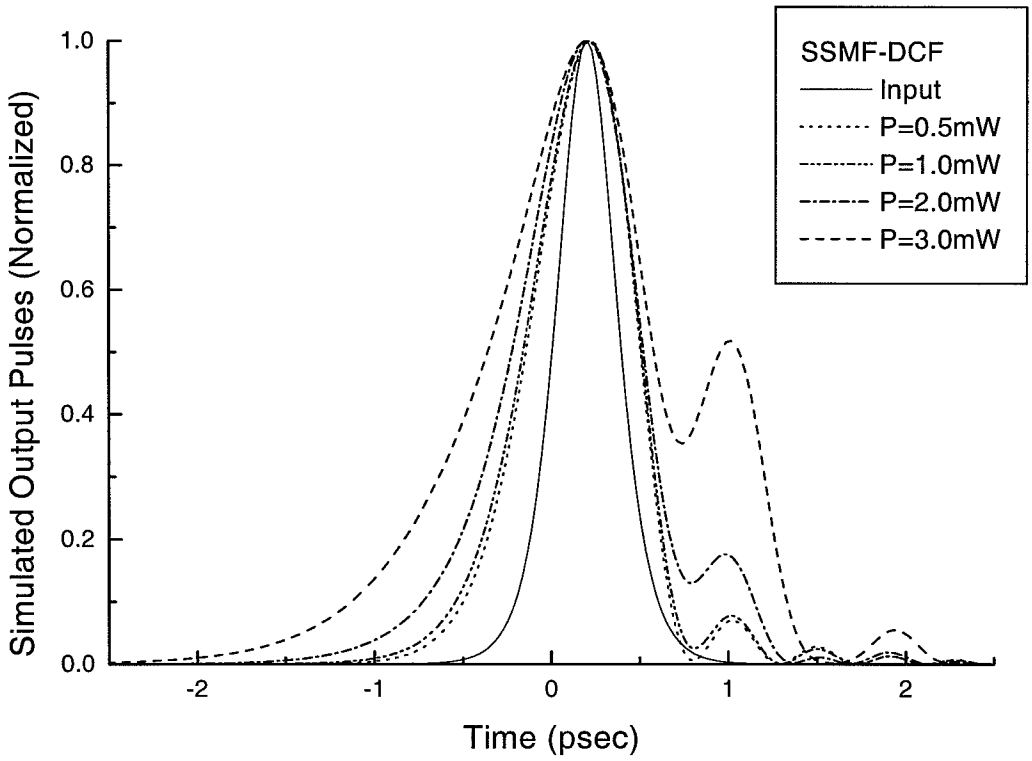

Fig. 4.12. Simulation results of normalized input and output pulses after a 2.5-km dispersion compensated link (SMF (2.06 km)-DCF (0.44 km)) for input peak power $P0 = 38$ mW, 75 mW, 150 mW, and 230 mw. The input pulse FWHM is 400 fsec (solid line).

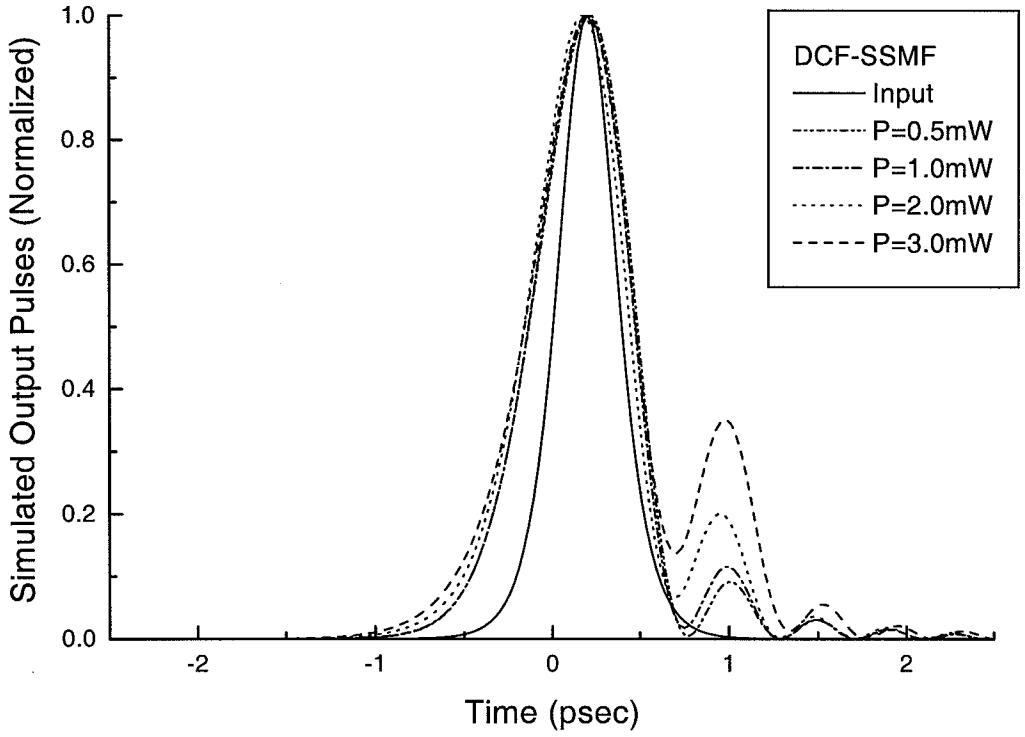

Fig. 4.13. Simulation results of normalized input and output pulses after a 2.5-km dispersion compensated link (DCF (0.44 km)-SMF (2.06 km)) for input peak power $P_0 = 38$ mW, 75 mW, 150 mW, and 230 mw. The input pulse FWHM is 400 fsec (solid line).

the dominant term leading to the different behavior of the SPM effects in the post-compensated and pre-compensated links. Other effects, such as differences in loss and third-order dispersion of SMF and DCF, are not needed to explain the overall trends.

4.4 Summary

We have experimentally and numerically demonstrated the SPM effects on 400-fs pulse transmission over a dispersion-compensated link using DCF. The interaction between the fiber dispersion and the SPM effect was shown to be a major factor that limits the amount of energy allowed to be launched into the dispersion-compensated link for femtosecond pulse transmission. This power limit will eventually provide an upper bound on the length of the transmission link due to the increasing loss for the longer link. Effects due to SPM are stronger for the post-compensated link. Nonetheless, our results indicate that transmission of sub-500-fs pulses in a dispersion-compensated fiber link should be possible at energy up to tens of pJ, which is consistent with high quality communication. For better pulse transmission, the pre-compensated scheme should be employed. For CDMA schemes the previous analysis is an overly conservative estimate, since a coded input pulse will have substantially lower intensity for fixed energy than that of an uncoded input pulse considered above. Nevertheless, our study shows that the nonlinear effect in the fiber transmission link is not severe in our current one transmitter and one receiver CDMA system, but will limit the system performance when the pulse energy is increased to accomodate more users in the networks.

5. Performance of an Ultrashort-pulse Optical CDMA Channel under Multi-access Interference

5.1 Introduction

The performance of ultrashort-pulse optical CDMA systems has been investigated in theory by Salehi et. al. in early 90's [8]. Over the past decade, advances on the key photonic devices required for CDMA operation have also made possible a CDMA test bed with one transmitter and one receiver [1, 6, 9, 15, 16]. However, the system-level evaluation of ultrashort-pulse optical CDMA has never been carried out in experiments. The key performance metric for any optical CDMA scheme is its ability to reject multi-access interference [55]. Therefore, it is critically important to study the performance of CDMA detection under multi-access interference in order to truly demonstrate its feasibility in a multiple-user environment. This chapter presents the first experimental study of multi-access interference suppression in an ultrashort-pulse fiber-optic CDMA system. We show that the CDMA system performance depends strongly on the efficacy of spectral phase coding and subsequent nonlinear signal thresholding. Our bit-error-rate (BER) measurements of a signal channel in the presence of the cross-talk from an interfering channel demonstrate almost total interference suppression, resulting in measured BER below 10^{-11}. This back-to-back system measurement provides us an evidence for the possibility of error-free CDMA detection with a large number of users in the system.

5.2 Experimental Setup

The block diagram of a complete ultrashort-pulse optical CDMA system has been shown in Fig. 1.1. Its performance is directly related to the ability of the receiver to reject multi-access interference. The receiver in a CDMA system generally con-

sists of a spectral phase decoder, an optical nonlinear thresholder, and a direct O/E convertor such as a PIN detector or an avalanche photodetector (APD). The suppression of interference is achieved primarily through pseudorandom spectral phase encoding/decoding in conjunction with the use of the nonlinear optical thresholder.

The structure and operation of the spectral decoder is similar to that of an encoder, except that the phase code applied is the complex conjugate of that applied in the encoder of the desired users [8]. After the decoder, correctly decoded data from a desired user are restored to clean ultrashort pulses with relatively high-peak intensity, while incorrectly decoded multi-access interference (MAI) appears as a pseudonoise-like signal. A nonlinear thresholder detects the peak power of the correctly decoded signals and suppresses the low intensity noise based on nonlinear optics. Note that without a nonlinear thresholder, the simple O/E conversion with even state-of-the-art bandwidth performance (normally < 50 GHz) is not sufficient to distinguish the correctly decoded femtosecond pulses from the incorrectly decoded noises ($\sim$tens of picoseconds in duration), since their pulse energy are the same.

To evaluate the efficacy of multi-access interference suppression, we performed back-to-back measurements in an ultrashort-pulse CDMA system with two users - one as a desired user and the other as an interfering user. Fig. 5.1 shows the schematic diagram of our experimental setup. At the transmitter side, we used the home-built passively mode-locked fiber laser [56, 23] (source #1 in Fig. 5.1) to provide a 40 MHz train of ultrashort pulses for the desired user. After an interference filter, the nearly transform-limited laser pulses (FWHM pulse-width $\sim$ 480 fs) were synchronously modulated at 40-Mb/s with a length-$2^{23}-1$ pseudorandom bit stream (PRBS) data. We used another mode-locked fiber laser (a Femtolite from IMRA, Inc) as the broadband source for the interfering user (source #2 in Fig. 5.1). It generates transformed-limited pulses repeated at 50 MHz. For simplicity, the interfering user's pulse train was not modulated in the experiments. The spectra of both signal and noise paths before the CDMA receiver were centered at 1560 nm as shown in Fig. 5.2.

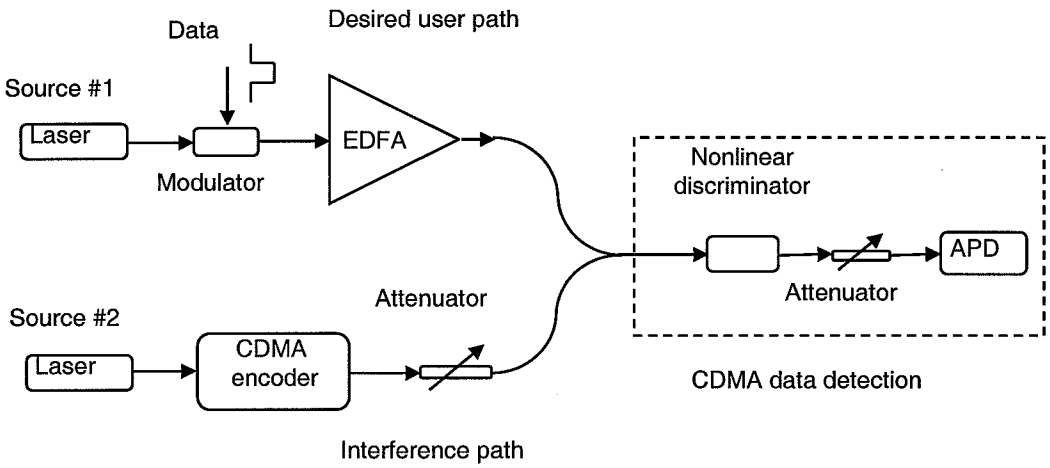

Fig. 5.1. Experimental setup of CDMA system BER measurements.

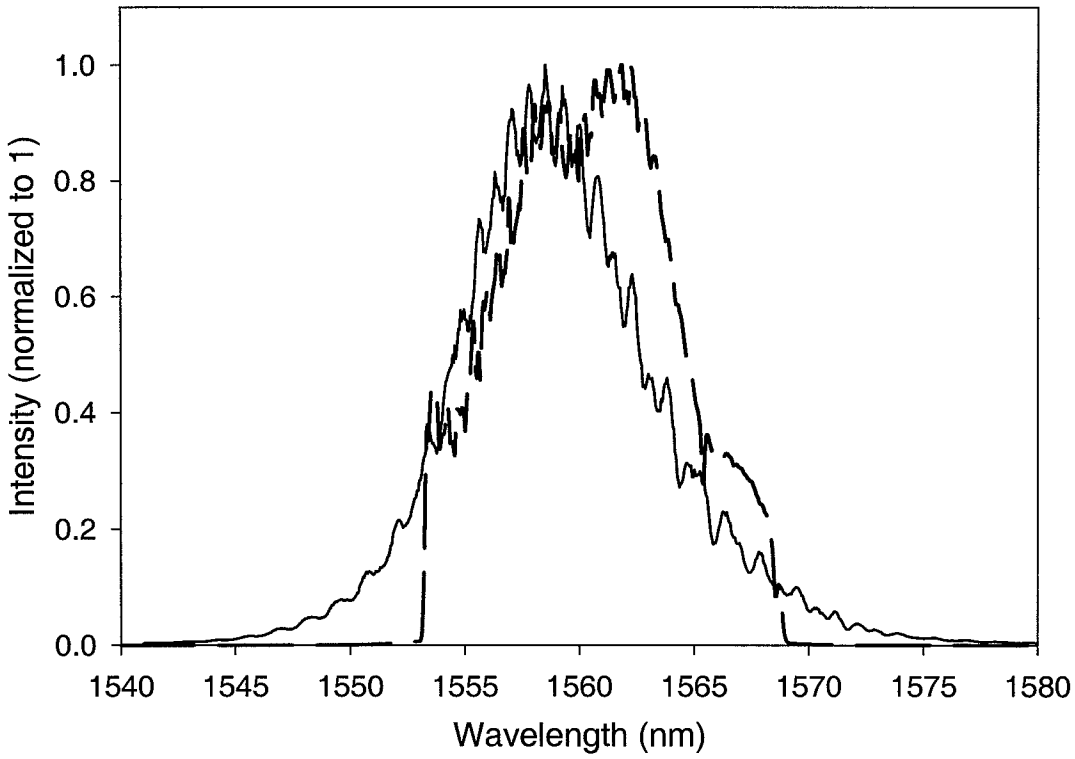

Fig. 5.2. Optical spectra of the desired user path (solid line) and interference path (dashed line).

Laser pulses from the interfering user (source #2) were launched into a fiber-pigtailed femtosecond pulse-shaper equipped with a 128-pixel liquid-crystal phase modulator (LCM) array [2] for spectral phase coding. After the pulse shaper, the interfering pulse has a FWHM pulsewidth of $\sim 430fs$ if constant phase is applied across the LCM. The structure of the pulse shaper is shown in Fig. 3.1. Pseudorandom M-sequence phase codes with various code lengths were applied in the LCM in experiments, which leads to coded pulses $\sim$ tens of picosecond in duration but with the almost the same pulse energy. Fig. 5.3 shows one example autocorrelation traces of interfering pulses without spectral phase coding and with length-31 M-sequence coding. Note that peak power of the coded pulses is substantially lower than that of uncoded pulses.

After being combined with modulated data from the desired user through a 1×2 fiber coupler, the coded pulses emulate the incorrectly decoded multi-access interference in a complete lightwave CDMA system. At the receiver side, we used a nonlinear thresholder based on self-phase modulation (SPM) in an optical fiber to suppress the incorrectly decoded noise for error-free CDMA data detection. An avalanche photodetector (APD) with a bandwidth of $\sim$ 550 MHz was used after the thresholder. For simplicity, we omitted spectral phase coding both after source #1 and in the CDMA receiver. Hence the uncoded pulses from source #1 emulate correctly decoded CDMA signals from the desired user.

Three types of nonlinear thresholder have been developed for CDMA operation by our colleagues — nonlinear fiber thresholder [6], two-photon absorption waveguide (TPA) [18], and thresholders based on second-harmonic generation. The nonlinear fiber thresholder based on self-phase modulation effect in an optical fiber was used in the experiment to study the CDMA system performance. It consists of a dispersion-shifted fiber (DSF) followed by a long-wavelength pass filter, which transmits very little of the input light unless there are frequency shifts toward the longer wavelength arising from SPM in the fiber. The zero dispersion wavelength of the DSF was chosen to coincide with the center wavelength of laser pulses for increased fiber nonlinear-

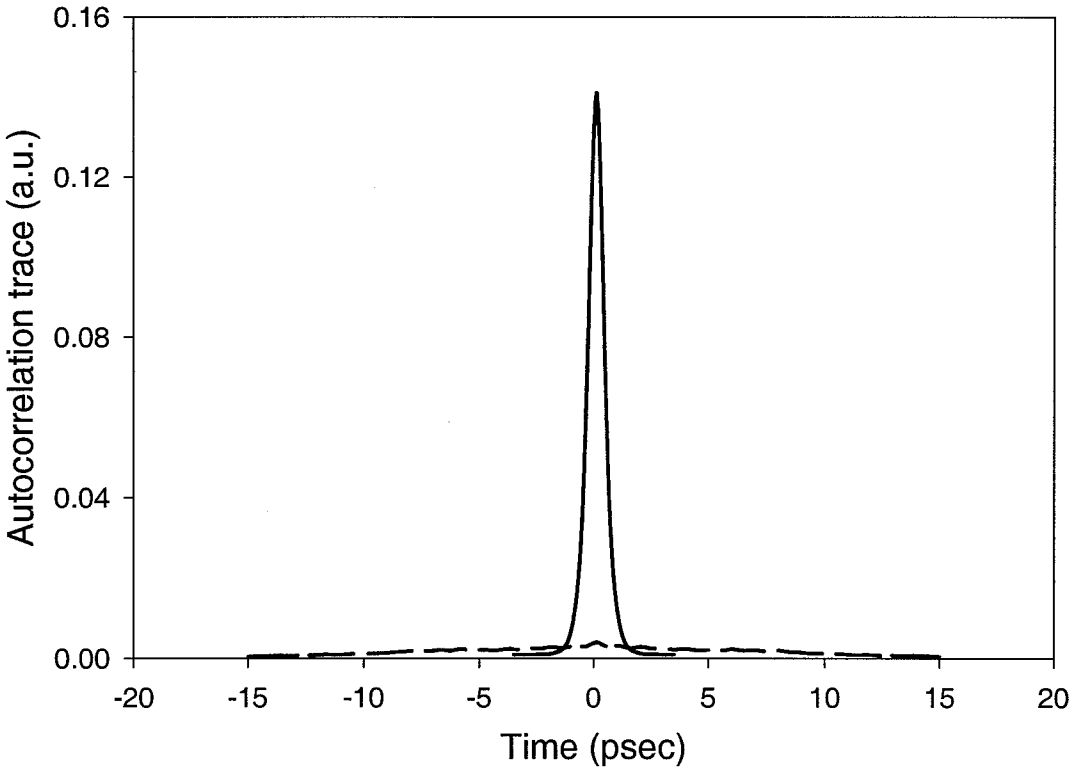

Fig. 5.3. Autocorrelation trace of the laser pulses in the interference path without phase coding (solid line) and with length-31 M-sequence phase coding (dashed line).

ity. The cutoff wavelength of the long-wavelength pass filter was set at 1572 nm to yield enough conversion efficiency ($\sim$ 10%) and large output contrast ratio ($> 35dB$) after the thresholder. Here the conversion efficiency is defined as the power ratio between the output and input of the thresholder for correctly decoded pulses and the contrast ratio is defined as the output power ratio between the correctly and incorrectly decoded pulses. Both signal and interference paths before the thresholder were dispersion compensated using dispersion-compensating fibers (DCF). Fig. 5.4 shows the autocorrelation traces of the laser pulses in the signal path before the nonlinear thresholder. The corresponding measurement for the interference path (no spectral phase coding) is shown in Fig. 5.3 (dashed line).

5.3 Experimental Results

In experiments, the average power of CDMA data (source #1) was fixed at 250μW before the nonlinear thresholder, which yields sufficient nonlinearity in the DSF to generate as much as 10 μW output power after the long-wavelength pass filter. For error-rate measurements, the received signal power at the APD was varied from -44 dBm to -37 dBm. To evaluate CDMA detection under large interference conditions, we always kept the interference power before the APD at -30 dBm when no phase coding was added in the interference path. This was achieved by adjusting the input interference power before the thresholder. Note that if no phase coding is used, the interference level is at a minimum 7 dB higher than the signal level at the APD. To show interference suppression, we first compared the eye-diagrams of the signal channel (set at -44 dBm before the APD) with and without a length-63 M-sequence phase code applied to the interference path. Fig. 5.5 shows optical spectrum of interfering pulses after the dispersion shifted fiber with and without the phase code (length-63 M-sequence). Clearly, coded pulses (here representing incorrectly decoded noise) do not generate appreciable components at the longer wavelength region ($>$ 1572 nm), therefore can be effectively suppressed by a long wavelength pass filter after the DSF. The eye-diagram in Fig. 5.6 shows that without phase coding, the desired data are completely buried under the multi-access interference. Note that the interference

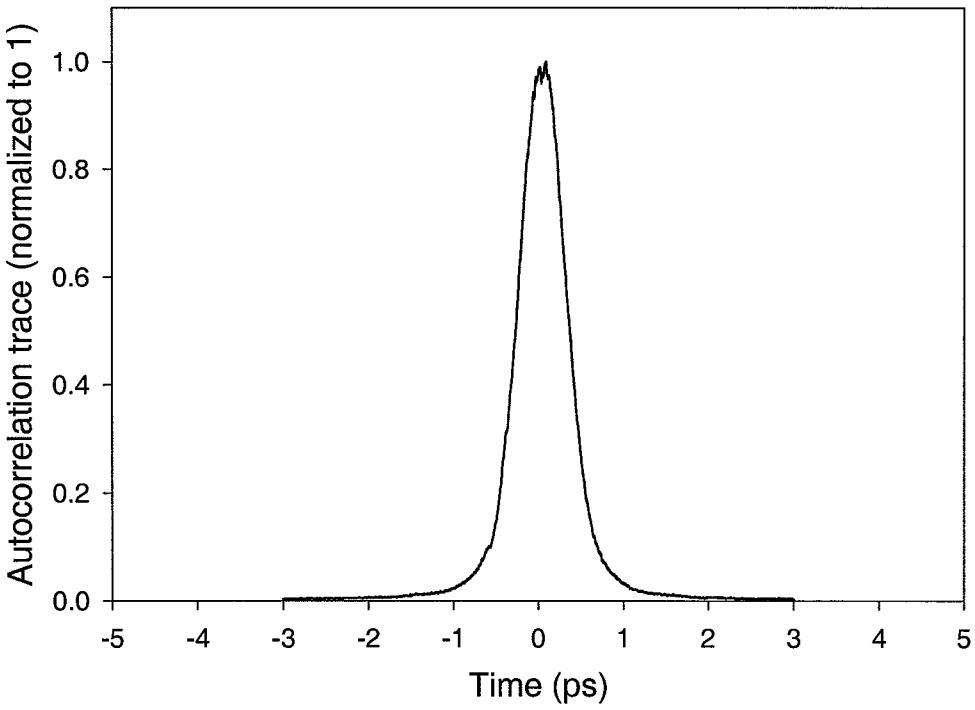

Fig. 5.4. Autocorrelation trace of the laser pulses in the signal path.

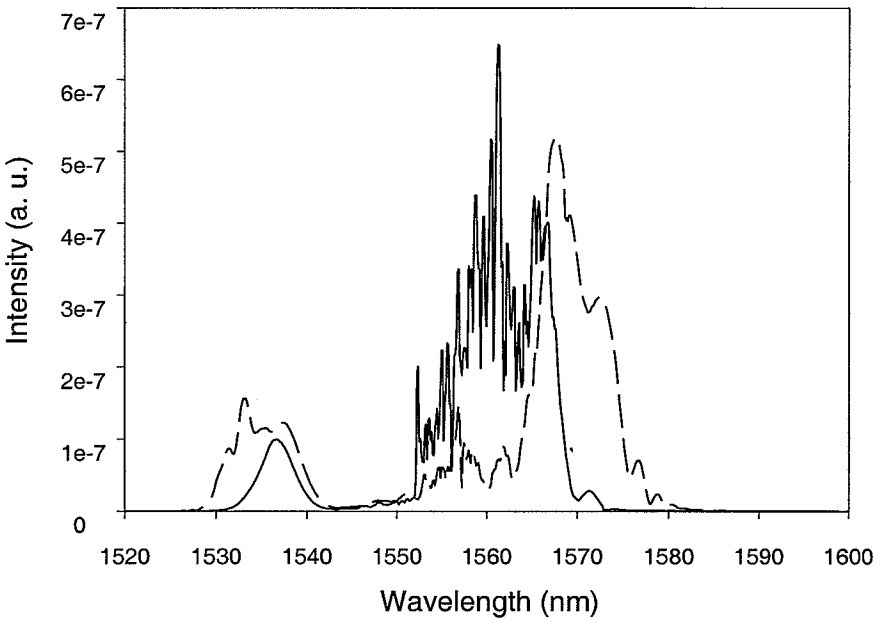

Fig. 5.5. Optical spectra of interfering pulses after the dispersion shifted fiber with and without length-63 M-sequence phase coding.

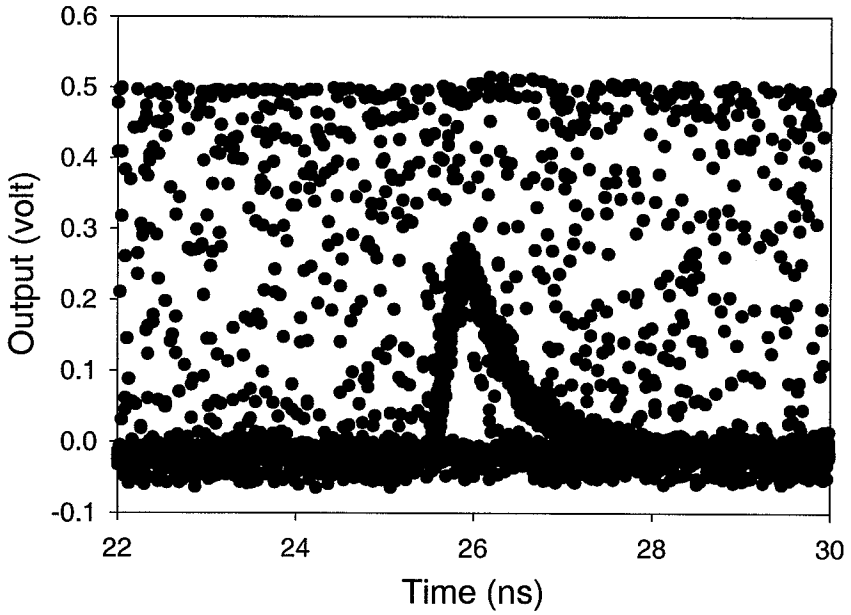

Fig. 5.6. Eye-diagrams of CDMA signals under multi-access interference without phase coding in the interference path).

power here is 14 dB larger than the signal power and has already saturated the APD receiver. The clean eye-diagram in Fig. 5.7 demonstrates that coding together with the fiber nonlinear thresholder strongly suppress this large interference, resulting in a clean and open eye.

Fig. 5.8 shows the BER performance of the signal channel when the length of the M-sequence phase code in the interference path was varied. For M-sequence code lengths of 7, 15, 31, and 63, the interference power was suppressed to 10 nW, 1.7nW, 0.6 nW and 0.1 nW (40 dB suppression!), respectively. For comparison, the BER of the signal channel without interference is also shown in Fig. 5.8. We note that as the coding length in the interference path increases, the power penalty to CDMA signal detection decreases substantially. When the code length reaches 63, the power penalty caused by the interfering user is almost zero. The decreased power penalty implies that with larger spectral phase coding length, more users could be supported simultaneously in a system. Since the interference power before the APD is purposefully set to be much larger than the signal power, our results provide evidence for the possibility of error-free CDMA detection with a large number of users in the system.

In conclusions, we have performed the first bit-error-rate measurement of an ultrashort-pulse CDMA channel under multi-access interference. Our results shows that the suppression of interference in a CDMA system depends critically on the spectral phase coding length and the output contrast of the nonlinear thresholder.

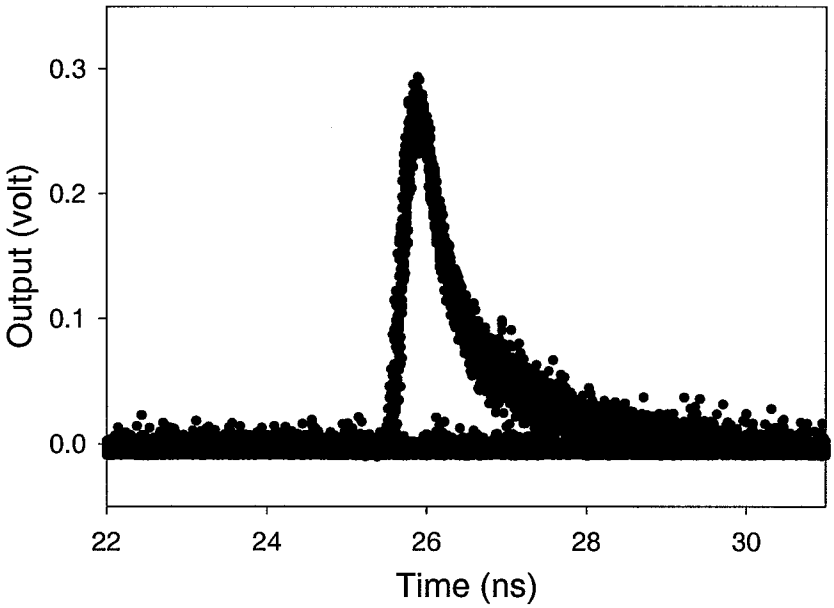

Fig. 5.7. Eye-diagrams of CDMA signals under multi-access interference with length-63 pseudorandom phase coding in the interference path).

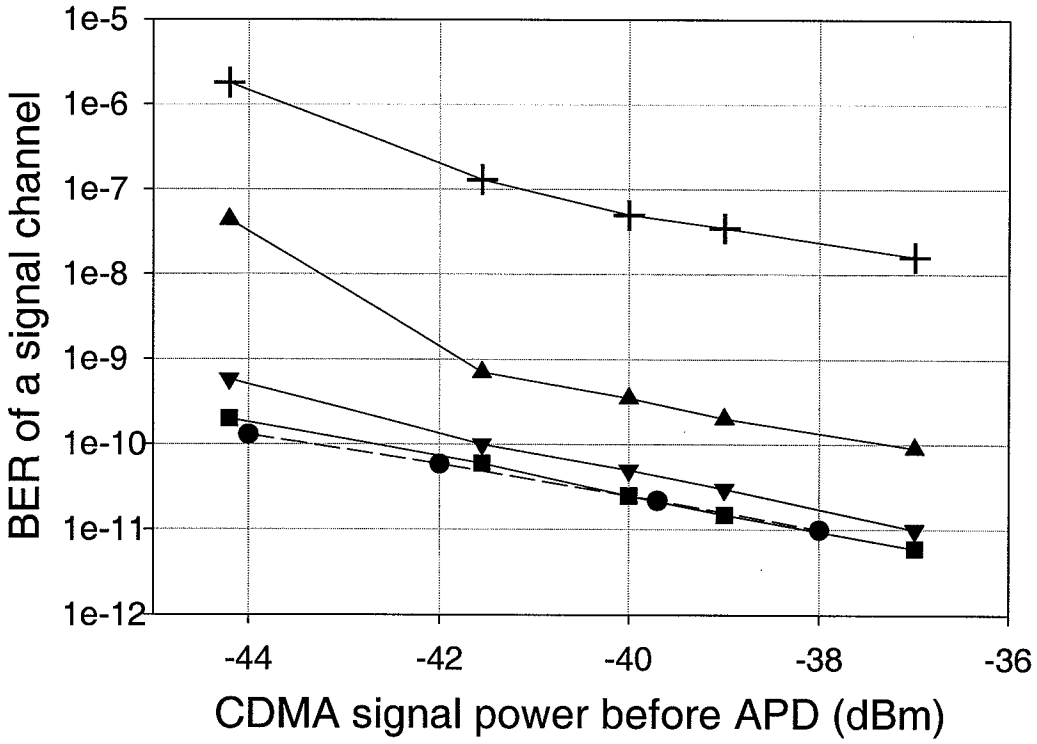

Fig. 5.8. BER of an ultrashort-pulse CDMA channel without interference (circle) and under interference with the M-sequence code length of 63 (square), 31 (down-triangle), 15 (up-triangle), and 7 (cross).

6. Spectrally Overlaid Optical WDM-CDMA Hybrid Operation for Fiber-optic Communications

6.1 Introduction

Ultrashort-pulse optical CDMA is feasible and useful for broadband fiber-optic communications. It can also be implemented in conjunction with other optical multiple-access techniques. The hybrid operation promises additional network advantages to an existing system using only one multiplexing technique. This chapter presents the proof-of-concept study of spectrally overlaying ultrashort-pulse optical CDMA on WDM in the same spectral region. In this hybrid WDM-CDMA scheme, broadband CDMA signals primarily utilize the spectral guard bands between WDM channels and may provide additional bandwidth to the WDM system without requiring costly expansion of EDFA bandwidth or very precise wavelength control of WDM lasers for closer channel spacing. The hybrid operation offers features from both WDM and CDMA - the mature technology available for WDM and the higher level data security as well as the potential for larger spectral efficiency promised by overlaying CDMA on WDM. In this chapter, we report the first system experiments indicating the feasibility of the hybrid WDM-CDMA operation through simultaneous error-free recovery of WDM in the presence of overlaid broadband ultrashort-pulse CDMA and of CDMA in the presence of narrowband WDM interference. The study includes (1) the performance measurements of WDM channels under different CDMA interference strength, (2) the development of a theoretical model (verified by our experiments) to predict the system performance at Gb/s CDMA data rate, (3) the detection of an ultrashort-pulse CDMA channel in the hybrid operation, (4) the scaling of the experiments to a system with many closely spaced WDM users. Note that this work, although was

performed in a fiber-optics context, is also applicable to free-space optical communications [57]. To show the compatibility of the CDMA and WDM schemes from the prospective of fiber transmission, we also demonstrated bit-parallel WDM data transmission over a dispersion-compensated fiber link designed for ultrashort-pulse CDMA operation with record-low timing skew.

6.2 Hybrid Optical WDM-CDMA Operation

Optical wavelength-division-multiplexing (WDM) is a major multiple-access techniques adopted by today's fiber-optic communication industry. It has been studied extensively over the past decade and plays an important role in both local-area and long-haul optical communications [58, 59]. In a WDM system, each user takes on a unique narrowband wavelength channel and users are distinguished by their channel locations in the network. Spectral guard bands between wavelength channels are obviously required in a WDM system to avoid channel crosstalks. Precision frequency control of WDM lasers is also necessary to prevent one user channel from interfering with other users. The use of guard bands unfortunately reduces the utilization of spectral bandwidth, i.e. usable bandwidth of fiber amplifiers. This makes it difficult to fully exploit the available bandwidth capacity. Unlike WDM, optical CDMA allows users to share the same spectral window. Users are distinguished through minimally-correlated code sequences. Therefore, one may envision to re-ultilize the guard bands between WDM channels by combining optical CDMA with WDM in the same communication system [60]. The additional CDMA channels may be used to support network control or additional data flow. An increased system spectral efficiency is expected with the hybrid WDM-CDMA operation.

The overlay of CDMA on WDM can be implemented in different ways. For example, one could envision to use the spectral guard band between two adjacent WDM channels as a spectral window for CDMA operation. Several CDMA windows could be implemented into a sparsely spaced WDM system to provide additional transmission bandwidth. In this thesis work, we focus on a different hybrid WDM-CDMA implementation, i.e. broadband CDMA is directly overlaid over WDM in the same

spectral region. It will be shown in the followings that the ultrashort-pulse CDMA can be easily integrated into a WDM system with this hybrid approach. The direct spectral overlay also enables us to study the crosstalk between WDM and CDMA signals during the hybrid operation. The concept of this hybrid optical WDM-CDMA is illustrated in Fig. 6.1. Here broadband ultrashort-pulse CDMA channels allow utilization of some of the optical bandwidth occupied by the guard bands between WDM channels and can be used to provide additional transmission bandwidth for WDM systems already operating at capacity or to support bursty traffic. The inherent difference between WDM and ultrashort-pulse CDMA signals both in the spectral domain (narrowband versus broadband) and in the time domain (low-intensity versus high peak power) implies that the cross talk between these two types of signals may be suppressed allowing simultaneous error-free recovery of WDM and CDMA data. For the WDM channels, interference from the CDMA overlay is mitigated based on two mechanisms: (a) the broadband nature of CDMA signals means that most of the CDMA energy that falls outside of one WDM channel can be eliminated by a narrowband pass filter in the WDM detector, and (b) for stronger suppression of CDMA energy within each WDM channel, one can use notched CDMA spectra. Since each notch in the CDMA spectrum is aligned to a particular WDM channel, the CDMA energy within the WDM bandwidth has been eliminated beforehand (see dashed line in Fig. 6.1). For the CDMA channels, interference from the overlaid WDM signals is also mitigated based on two mechanisms: (a) each WDM channel only takes on a narrow spectral window. A series of narrow-band notch filters in the CDMA receiver may eliminate most of the WDM energy without seriously degrading the CDMA signal. (b) WDM traffic typically is of low-intensity NRZ or RZ data in contrast to the high peak-power of CDMA signals. Any WDM energy surviving the notch filters is strongly suppressed by the nonlinear optical "thresholder". Note that the thresholder is already required for pure ultrashort-pulse CDMA implementation. With effective interference suppression, the hybrid WDM-CDMA operation is feasible using receivers designed either for pure WDM or for a pure ultrashort-pulse CDMA

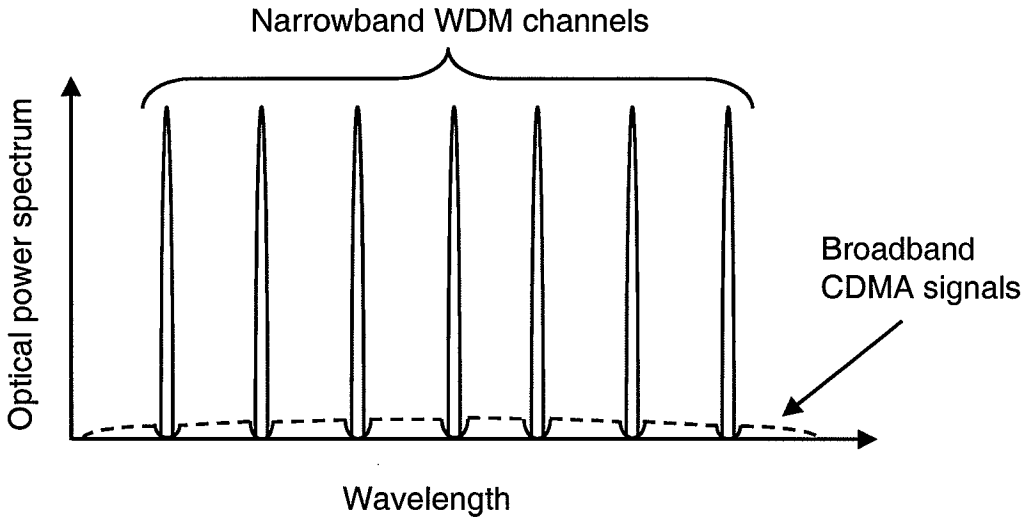

Fig. 6.1. The concept of spectral overlaid hybrid WDM-CDMA scheme. Solid line: narrowband WDM channels, Dashed line: broadband CDMA channel with spectral notches.

system, with only slight modification.

To evaluate the cross-talk between WDM signals and CDMA data and demonstrate the hybrid operation, we constructed a sub-system test bed shown in Fig. 6.2 and performed back-to-back system measurements. In this system, incoming network traffic consists of both WDM data and spectrally overlaid CDMA data. At the receiver end, each user is equipped with two detectors - one for WDM detection and the other for CDMA detection, which both receive the hybrid data. The structure of the WDM detector consists of a narrowband pass filter followed by direct O/E conversion. In the CDMA detector, we used a spectral decoder made from a fiber pigtailed femtosecond pulse-shaper equipped with a programmable liquid-crystal phase-modulator array [9]. Since the wavelength components of both CDMA and WDM data are spatially dispersed across the Fourier plane of the pulse shaper, narrow-band notch filters were easily installed at the Fourier plane to remove most ($> 99.6\%$) of the WDM power. Then after an EDFA with 25dB gain, we launched the CDMA data and the residual WDM interference into a nonlinear fiber thresholder based on self-phase modulation (SPM) in a dispersion-shifted fiber [6]. The nonlinear thresholder rejects improperly decoded pulses from interfering CDMA users (manifested as low-intensity pseudo-noise signals) and recognizes properly decoded pulses from a desired CDMA user (clean femtosecond or subpicosecond pulses) based on signal peak power [55, 6]. Since the WDM signal has low peak intensity, any residual WDM interference after the notch filters is completely rejected by the nonlinear thresholder as well. In the following, we report our experimental results on simultaneous error-free detection of both WDM and CDMA data in this hybrid system.

6.3 Error-free Detection of WDM Data in the Presence of CDMA Interference

We first evaluated WDM channel performance in the hybrid system through measuring the bit-error-rate performance of two WDM channels overlaid with one CDMA channel in the same spectral region. The WDM signals were generated from two temperature-stabilized DFB lasers, each modulated at 2.5Gb/s with length-$2^{31} - 1$

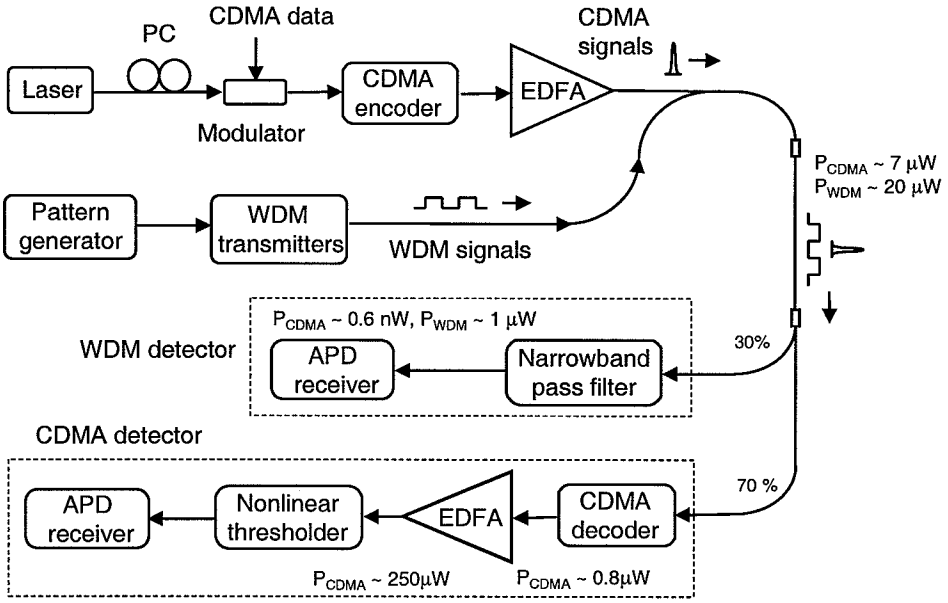

Fig. 6.2. Schematic diagram of a hybrid WDM-CDMA system test bed.

NRZ pseudorandom bit stream (PRBS) data. A passively mode-locked fiber laser [23, 24, 56] was used to generate a 400fs-pulse (transformed-limited) CDMA channel modulated with 40-Mb/s length-$2^{23} - 1$ RZ PRBS data. We note that although the CDMA data rate is at present limited by the low repetition rate of our passively mode-locked femtosecond laser, it suffices to demonstrate the WDM-CDMA overlay scheme as well as to verify our theoretical expressions for the performance of such a system. To evaluate two extreme cases, we intentionally tested one WDM channel located close to the peak of the CDMA spectrum at 1560.4 nm and the other near the edge at 1551.2 nm in experiments. The optical spectrum of the hybrid data before the WDM receivers is shown in Fig. 6.3. To suppress CDMA interference for error-free WDM detection, we first added two spectral notches at the CDMA encoder (shown in Fig. 6.2) to reduce CDMA energy within WDM bandwidth, where each notch is aligned to the corresponding WDM channel location. The incoming CDMA signals therefore have notched spectra. Then the CDMA energy outside each WDM channel is suppressed through a narrowband pass filter centered at each channel. After the band-pass filter, an avalanche photo detector (APD) with a bandwidth of 2 GHz was used for WDM data detection. In experiments, the average power of the co-propagating CDMA signals before the WDM detector is varied with a minimum of $\sim 2\mu W$. This power level scales to high enough CDMA energy for high quality nonlinear thresholding operation ($>$ 20dB contrast between properly and improperly decoded pure CDMA signals) in the CDMA detector. For the WDM channel at 1560.4 nm, the insertion loss of the narrowband pass filter (FWHM $\sim$ 0.1nm) is $\sim$ 8-dB. After the filter, the CDMA interference was suppressed by $\sim$ 34 dB, which includes $\sim$ 8-db insertion loss of the filter setup itself. The measured BER under different CDMA power before the WDM detector is shown in Fig. 6.4. Fig. 6.5 shows the eye-diagram of the channel at 1560.4nm corresponding to BER $\sim 2 \times 10^{-9}$. Using a similar narrowband filter centered at 1551.2nm, we measured the channel at the edge of the CDMA spectrum. The power penalty from the CDMA cross-talk to both channels at 1560.4 nm and at 1551.2 nm is shown in Fig. 6.6. We found that for

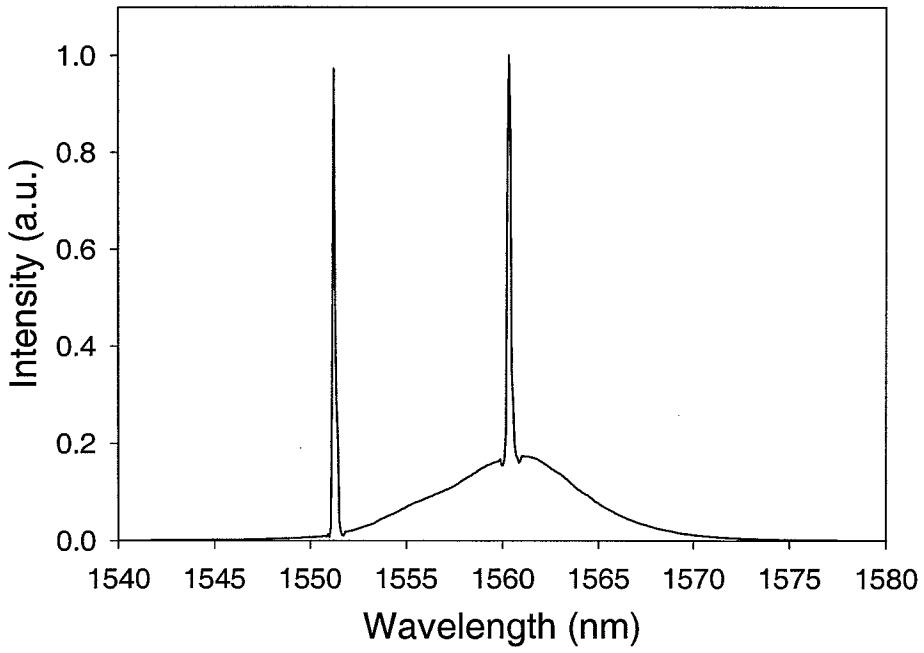

Fig. 6.3. Optical spectrum of two WDM channels and one overlaid CDMA channel before data detection.

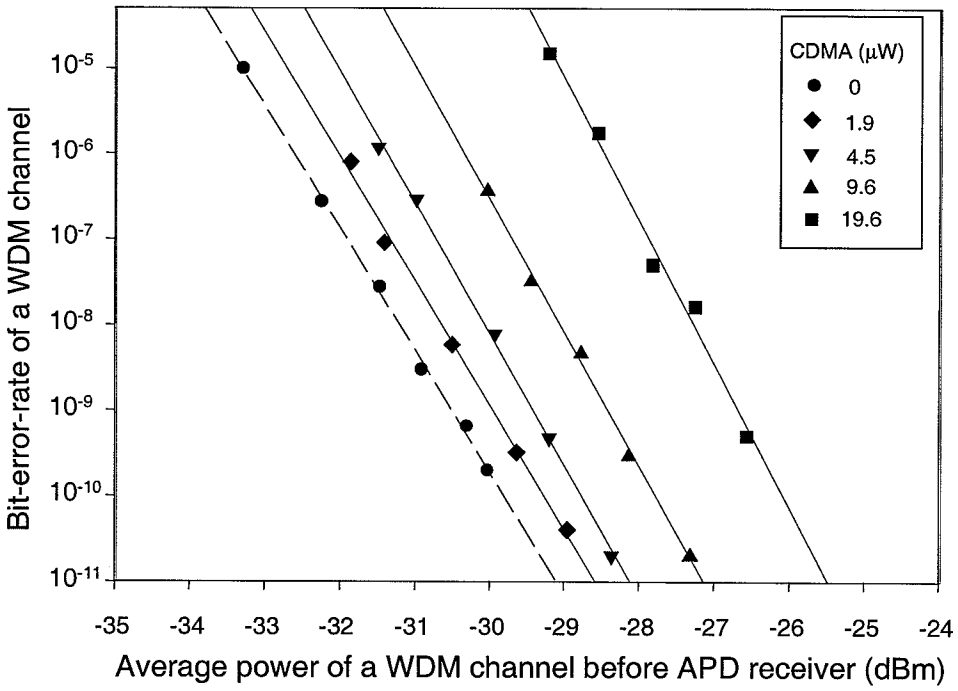

Fig. 6.4. BER performance of the WDM channel at 1560.4nm with different CDMA average power before the WDM detector: Circle, $0\mu W$; Diamond, $1.92\mu W$; Down-triangle, $4.48\mu W$; Up-triangle, $9.56\mu W$; Square, $19.56\mu W$.

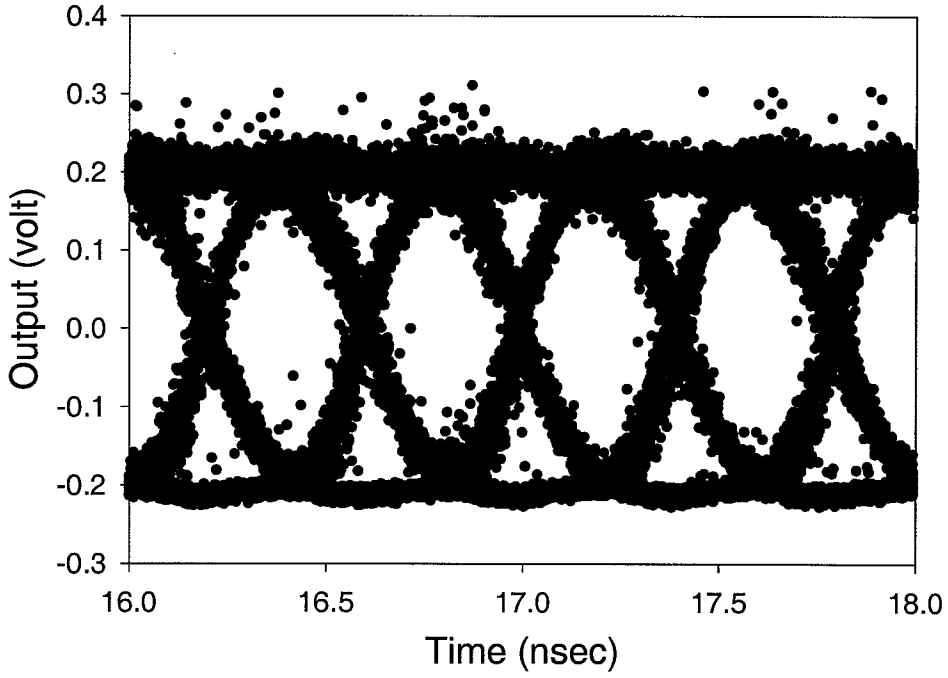

Fig. 6.5. Eye-diagram of the WDM channel at 1560.4 nm under residual CDMA interference (BER $\sim 1 \times 10^{-9}$).

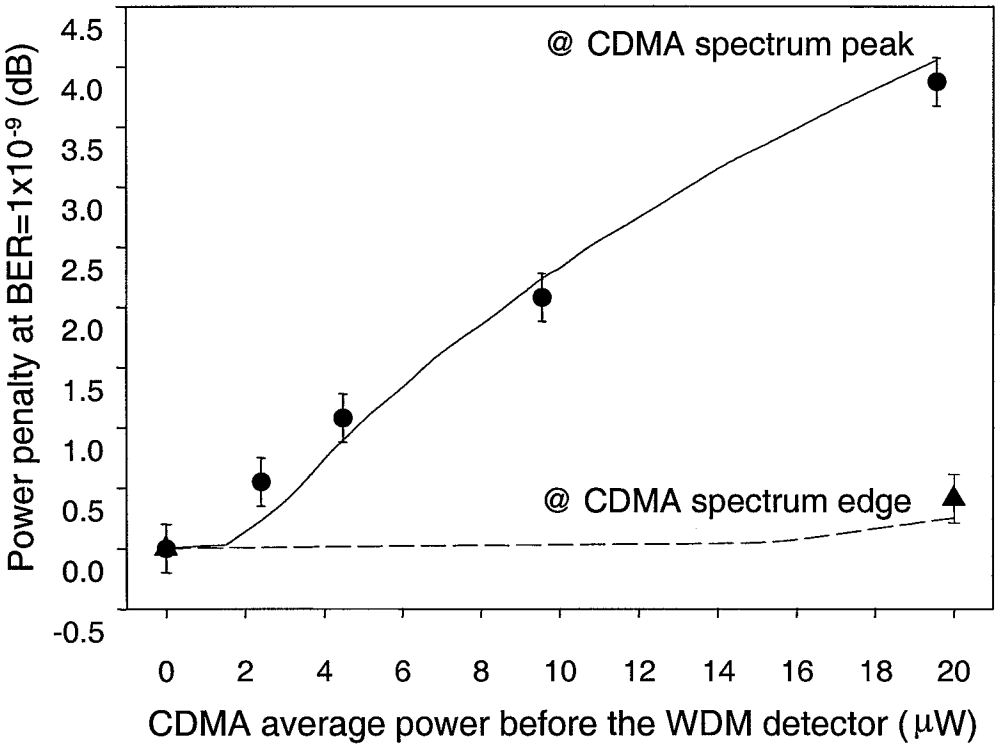

Fig. 6.6. Power penalty to WDM channels (1560.4 nm and 1551.2 nm) under different levels of CDMA interference. Circle, for the channel at the CDMA spectral peak (1560.4 nm), Triangle, for the channel at the CDMA spectral edge (1551.2nm). Solid and dashed line, simulation results.

the channel at the CDMA spectral peak, the power penalty is only $\sim$ 0.5dB when the CDMA interference is $2\mu W$, while the power penalty to the channel at 1551.2nm (CDMA spectral edge) is $<$ 0.2dB. When the strength of CDMA interference is increased to $\sim 20\mu W$, which is 10 times higher than needed, we found $\sim$ 4 dB power penalty to the channel at 1560.4 nm and 0.5 dB to the channel at 1551.2 nm.

6.4 Modeling of the WDM Channel Detection under CDMA Interference

To predict system performance under various operating conditions, we modeled the error rate of the WDM detection in our hybrid system through simply taking into account the SNR degradation caused by the interference from a single CDMA user. Modeling the interference for multiple CDMA users [8, 61] is more involved and is beyond the scope of this work. Assuming the detection of a WDM channel alone with binary encoding follows Gaussian noise statistics, one may relate the bit-error-rate (BER) to the signal-to-noise ratio (SNR) Q_w at a WDM detector as shown in Eq. 6.1.

$$BER_w = \frac{1}{2} erfc(\frac{Q_w}{\sqrt{2}}) \tag{6.1}$$

where Q_{WDM} is estimated in Eq. 6.2 [62].

$$Q_w = \frac{I_{WDM}}{\langle \sigma_{w1} \rangle + \langle \sigma_{w0} \rangle} \tag{6.2}$$

Here $I_{WDM} = R \times (P_{wh} - P_{wl})$ is the detected signal current and R is the receiver responsivity. P_{wh} and P_{wl} are the peak powers of the WDM signal for symbols "1" and "0" respectively. $\langle \sigma_{w1} \rangle$ and $\langle \sigma_{w0} \rangle$ are the corresponding root-mean-square (RMS) noises, which takes into account both detector thermal noise and shot noise. To account for the detection noises from CDMA cross-talk, one needs to consider the eye-closure caused by the co-propagating CDMA signals in WDM channels. Fig. 6.7 shows one example of the measured WDM eye-diagram for the channel (1560.4 nm) under large CDMA cross-talk (BER $\sim 5 \times 10^{-5}$).

Note that CDMA channels use return-to-zero (RZ) coding while WDM channels employ non-return-to-zero (NRZ) data format. From Fig. 6.5 and 6.7, we observed that the CDMA cross-talk moves the lower rail (symbol "0") of the WDM eye pattern

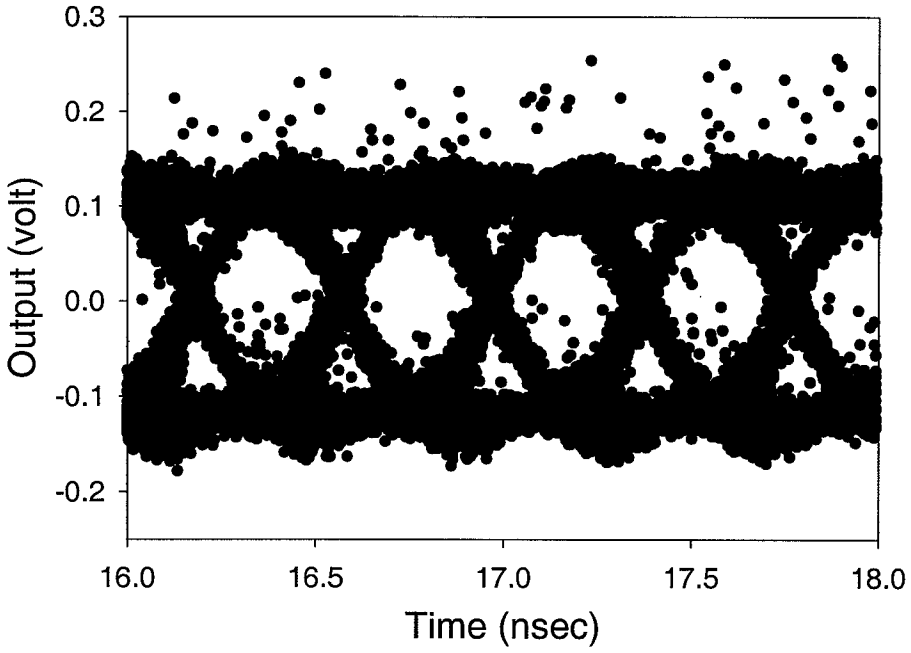

Fig. 6.7. Eye-diagram of the WDM channel at 1560.4 nm under large CDMA cross-talk (BER $\sim 5 \times 10^{-5}$)

closer to the decision level optimized for pure WDM detection and on the other hand moves the upper rail (symbol "1") away from the decision level. Hence one would expect that most of the CDMA induced WDM detection errors come when the symbol "1" in the CDMA channel overlaps with the symbol "0" in the WDM channel. In our analysis, we assumed that the detection of WDM data bits ("0" or "1") overlapped with CDMA symbol "1" still follows Gaussian noise statistics. For simplicity, we also assumed that the CDMA data rate is lower than or equal to the WDM data rate and that the decision threshold is kept at the optimum value for pure WDM operation. As a rough estimation, the performance of WDM channels in the hybrid system can be given by the weighted summation (Eq. 6.3) of error performance with and without CDMA symbol "1" overlapping with WDM data bits.

$$BER_{overlap} = (1 - P_{overlap}) \times BER_w + P_{overlap} \times (\frac{1}{2} BER_{w0+c1} + \frac{1}{2} BER_{w1+c1}) \quad (6.3)$$

$$BER_{w0+c1} = \frac{1}{2} erfc(\frac{Q_{w0+c1}}{\sqrt{2}}) \quad (6.4)$$

$$BER_{w1+c1} = \frac{1}{2} erfc(\frac{Q_{w1+c1}}{\sqrt{2}}) \quad (6.5)$$

The error-rate contribution from the CDMA cross-talk consists of two terms — the error performance when CDMA "1" overlaps with WDM "0" as expressed by in Eq. 6.4 and when CDMA "1" overlaps with WDM "1" as in Eq. 6.5. Q_{w0+c1} and Q_{w1+c1} are the corresponding SNRs of the WDM channel. $P_{overlap}$ is the probability of a CDMA "1" overlapping with a specific WDM data bit at any sampling instant, which takes into account different CDMA and WDM data rates. We note that CDMA signals are short optical pulses a couple of hundreds of femtoseconds in duration. After O/E conversion at the APD with 2 GHz bandwidth, the electrical pulse width of CDMA signals ($\sim 175ps$) is smaller than that of WDM signals ($\sim 400ps$ for 2.5 Gb/s data rate). Therefore, if CDMA data rate f_{CDMA} is smaller than WDM data

rate f_{WDM} , we can estimate $P_{overlap} = \frac{1}{2}\frac{f_{CDMA}}{f_{WDM}}$, where the factor of $\frac{1}{2}$ reflects the assumption that in a long CDMA bit stream, as many marks and spaces occur.

To estimate Q_{w0+c1} and Q_{w1+c1} in Eqs. 6.4 and 6.5, we consider the effects of CDMA "1" overlapping with WDM "0" and "1" separately. We note that the probability density function of a Gaussian random variable has a symmetric profile and recall that a CDMA "1" moves the lower rail of the WDM eye-pattern closer to the decision level. Therefore, the error-rate contribution for the case of CDMA "1" overlapping with WDM "0" is equivalent to one half of the error rate of a pure WDM channel with reduced signal strength $(I_{WDM} - 2I_{CDMA})$. Note that $I_{WDM} = R \times (P_{wh} - P_{wl})$ is defined as the distance between the upper and lower rail of the eye-pattern. Therefore a factor of 2 before I_{CDMA} is required here to reflect the reduction caused by the RZ formatted CDMA signal. Similiarly, since the CDMA signal moves the upper rail of the WDM eye-pattern away from the decision level, the error-rate contribution for the case of CDMA "1" overlapping with WDM "1" is equivalent to one half of the error rate of a pure WDM channel with increased signal strength $(I_{WDM} + 2I_{CDMA})$. From above discussions, one may estimate Q_{w0+c1} and Q_{w1+c1} as shown in Eqs. 6.6 and 6.7.

$$Q_{w0+c1} = \frac{I_{WDM} - 2I_{CDMA}}{\langle\sigma_{o1}\rangle + \langle\sigma_{o0}\rangle} \tag{6.6}$$

$$Q_{w1+c1} = \frac{I_{WDM} + 2I_{CDMA}}{\langle\sigma_{o1}\rangle + \langle\sigma_{o0}\rangle} \tag{6.7}$$

$\langle\sigma_{o1}\rangle$ and $\langle\sigma_{o0}\rangle$ represent the RMS noise for the case of a CDMA "1" overlapping with a WDM "1" or "0" respectively. $\langle\sigma_{o1}\rangle$ and $\langle\sigma_{o0}\rangle$ are similar to the noise forms for pure WDM operation, but increased to account for the additional shot noise caused by the CDMA cross-talk as shown in Eqs. 6.8 and 6.9. Note that here we assumed incoherent addition of CDMA and WDM signals in the analysis; this should be a good approximation due to the very different optical bandwidths of CDMA and WDM signals.

$$\langle \sigma_{o0} \rangle = \sqrt{\frac{4kTBF}{R_o} + 2qBM^2F(RP_{wl} + I_{CDMA} + I_{bd})} \tag{6.8}$$

$$\langle \sigma_{o1} \rangle = \sqrt{\frac{4kTBF}{R_o} + 2qBM^2F(RP_{wh} + I_{CDMA} + I_{bd})} \tag{6.9}$$

B is the bandwidth of the receiver. F is the noise figure of the receiver amplifier. k is the Boltzmann constant. T is the operating temperature ($297K$ for room temperature). R_o is reveiver output impedence. q is electrical charge. M and I_{bd} are the amplification factor and the dark current of the APD respectively.

Since the CDMA channel uses impulsive coding, the received CDMA current is given as [63]

$$I_{CDMA} = 2 \times \alpha \times R \times \gamma \times P_{avec} \times F_x \tag{6.10}$$

$$\alpha = \frac{B}{f_{CDMA}} \tag{6.11}$$

$$F_x = \frac{1 - 2exp(\frac{-2\pi\alpha}{\sqrt{3}})}{1 - exp(\frac{-2\pi\alpha}{\sqrt{3}})} \tag{6.12}$$

$$\gamma = \frac{1.2\pi}{\sqrt{3}} \tag{6.13}$$

F_x is the bandwidth dependent inter-symbol interference penalty. P_{avec} is the average power of CDMA interference. Using Eqs. 6.3 to 6.13, we computed the power penalty to two WDM channels (1560.1 nm and 1551.2nm) under different levels of CDMA cross-talk before the WDM detector. The solid line and dashed line in Fig. 6.6 show the simulation results under our experimental conditions. The simulation results match the experiment data well, which validates our error-rate estimation model. To further predict the system performance for Gb/s CDMA data rate, we used our model (Eq. 6.3) to compute the error-rate performance of the WDM channels in the hybrid system with different CDMA data rate. For comparisons, we assumed constant CDMA pulse energy in the calculation. Fig. 6.8 shows our simulation results

on power penalty to the WDM channel (1560.4 nm) at the peak of CDMA spectrum for CDMA data rate up to 2.5 Gb/s. When CDMA data rate changes from 40 Mb/s (experimental condition) to 2.5 Gb/s, the calculated additional power penalty to WDM detection is only $\sim 1-$dB. This reflects the fact that the dominant factor in determining the hybrid cross-talk induced power penalty is the CDMA pulse energy, which we have assumed constant in the simulation. Our results indicate that the error-free operation of WDM channels in the hybrid WDM-CDMA system should be possible for simultaneous Gb/s CDMA and WDM data rates. Further reductions of the power penalty would occur with improvements to the CDMA detection path, since this would lower the CDMA power at the front of the WDM detector as well. This could be achieved by increasing the EDFA gain by a modest amount or possibly by developing a thresholder with a lower power requirement in the CDMA detector.

6.5 Error-free Detection of CDMA Signals in the Presence of WDM Interference

To demonstrate the feasibility of error-free CDMA detection in the hybrid system, we measured the BER performance of an ultrashort-pulse CDMA channel spectrally overlaid with a WDM channel using the CDMA detector shown in Fig. 6.2. To simplify the measurement, we omitted the CDMA encoder shown in Fig. 6.2 in the data path. By applying either a constant phase or a length-31 M-sequence phase code in the decoder, we emulated the properly and improperly decoded CDMA signals respectively. The CDMA ultrashort-pulse train was generated from a passively mode-locked fiber laser centered at 1560 nm with the repetition rate of 40-MHz. The nearly transform-limited pulses (FWHM pulsewidth $\sim 480fs$) were synchronously modulated at 40-Mb/s with a length-$2^{23}-1$ pseudorandom bit stream (PRBS). The data path of CDMA signals was dispersion compensated using a dispersion-compensating fiber (DCF). Our previous work showed that this is possible for $> 10km$ fiber length [20, 64]. The overlaid WDM signal was again generated from a temperature-stabilized DFB laser centered at the peak of CDMA spectrum ($\lambda_0 = 1560.4nm$, FWHM $< 0.1nm$) and modulated with 2.5-Gb/s $2^{31}-1$ nonreturn-to-zero (NRZ) PRBS data.

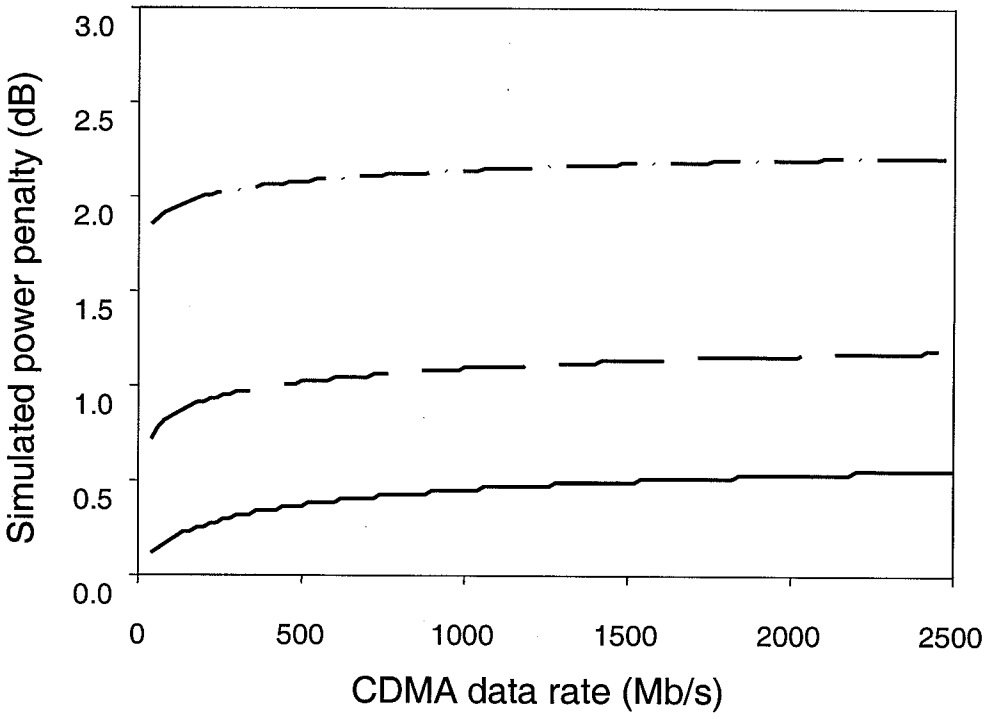

Fig. 6.8. Simulation results on power penalty to the WDM channel at 1560.4 nm with different CDMA data rate. CDMA average power before the WDM detector at 40 Mb/s: Solid line, $2\mu W$; Dashed line, $4\mu W$; Dot-dashed line, $8\mu W$.

The decoder in the CDMA detector has an insertion loss of 8 dB for both WDM and CDMA signals. The average CDMA signal power is $> 5\mu W$ before the decoder (which corresponds to $> 2\mu W$ CDMA signals before the WDM detector) and $> 250\mu$W before the fiber thresholder. We note that this energy level yields $>$ 20dB contrast ratio between properly and improperly decoded CDMA pulses at the output of the thresholder, which ensures sufficient multi-access interference suppression for proper CDMA operation alone. The CDMA power used here could be lowered possibly by using a thresholder with lower power requirement.

The average power of WDM signals before the CDMA decoder was intentionally set to $\sim 75\mu W$, which is 5 times higher than needed to yield simultaneous error-free detection in the WDM detector as shown earlier. This is also $\sim$ 15 times higher than the CDMA power prior to the detector. The notch filter (FWHM $\sim 0.3nm$) in the pulse shaper (i.e. decoder) blocks the WDM component with an extinction ratio of 30-dB (This includes the insertion loss of the pulse shaper itself). Note that in a complete system, the incoming CDMA signals already have spectral notches added in the encoder as we described earlier. Hence the use of notch-filters at the CDMA detector does not degrade CDMA detection further. The output spectrum after the decoder with the WDM channel blocked is shown in Fig. 6.9. After the thresholder, an APD detector with a bandwidth of 550 MHz was used to detect the CDMA signals. Fig. 6.10 shows the BER performance of the CDMA channel with and without the WDM interference. Our results show no observable power penalty to CDMA detection from the coexisting WDM signals. The WDM interference has been completely removed in the CDMA detection path by the spectral notch filter and the fiber thresholder. The use of nonlinear thresholder is effective in suppressing the low-intensity WDM components. We found in experiments that the thresholder can tolerate as high as 1-mW WDM residual interferences. Note that it is expected that this CDMA detection scheme should work equally well for Gb/s CDMA data rates as long as the output of the fiber amplifier is increased proportionally.

With many closely spaced WDM users in the hybrid system, multiple spectral

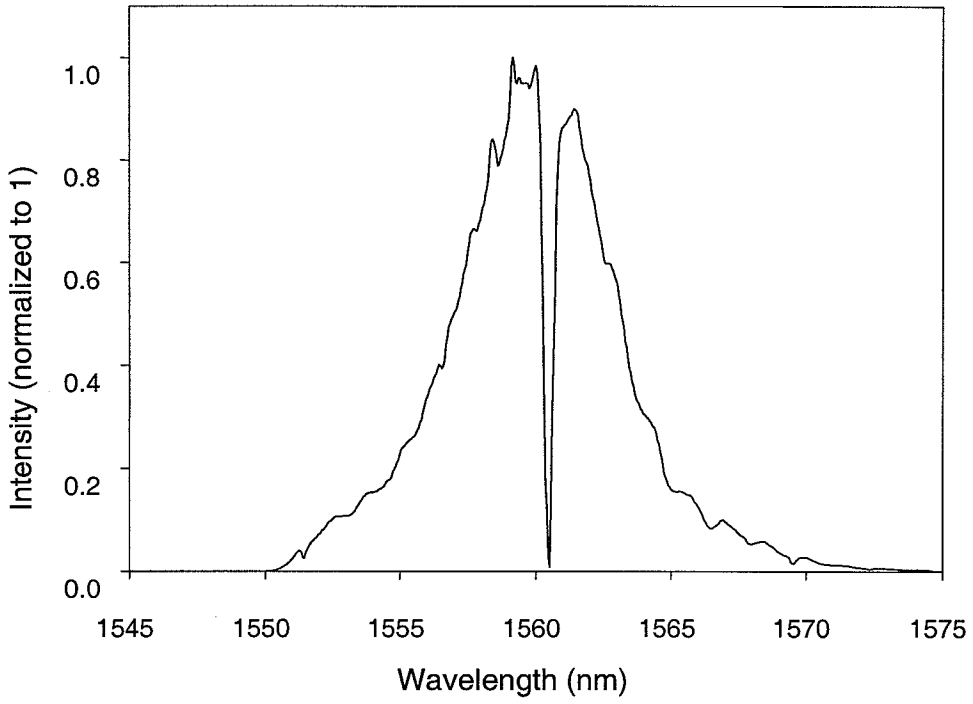

Fig. 6.9. Optical spectrum of a CDMA channel with a narrowband spectral notch filter (0.3 nm) blocking WDM components at 1560.4 nm.

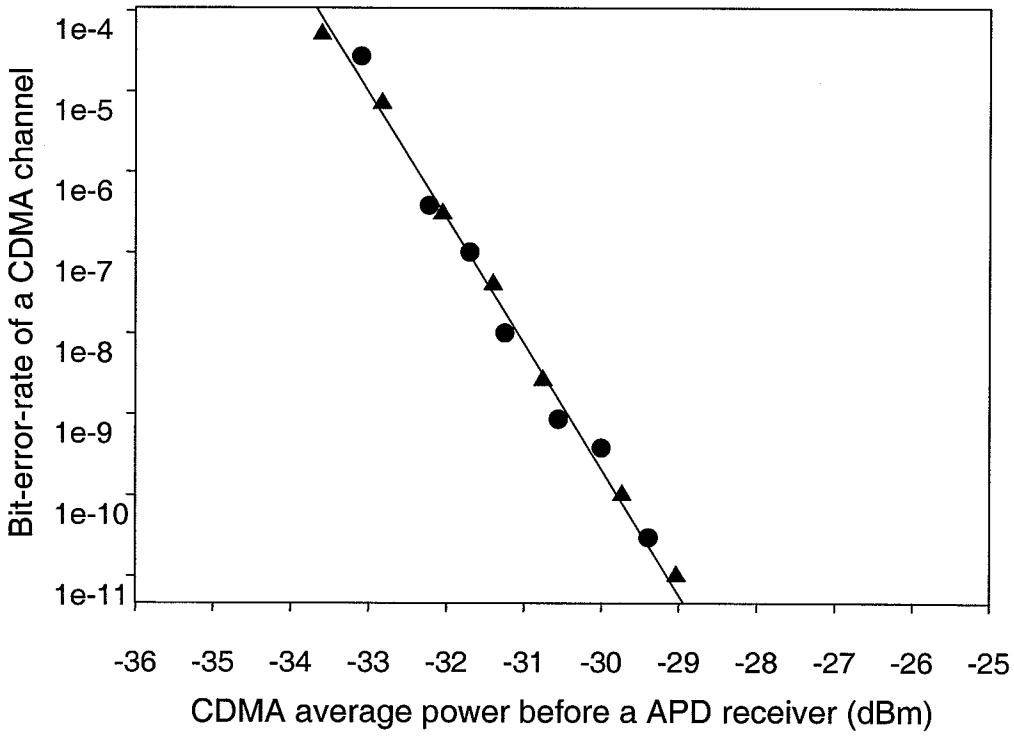

Fig. 6.10. BER of a CDMA channel without WDM interference (circle) and with a $75\mu W$ WDM signal (triangle) before the decoder.

notches will lead to a peak power reduction in the ultrashort-pulse CDMA signals, which eventually degrades the output contrast ratio between the properly and improperly decoded signals after the nonlinear thresholder. This is expected to be the major impairment to CDMA detection in the hybrid operation. However, this power loss can be compensated through simply increasing the gain required before the thresholder in order to maintain sufficient multi-access interference suppression. To evaluate this multiple-notch effect, we measured the additional gain required in the CDMA detector to maintain constant 20-dB thresholding contrast compared to the CDMA signal without spectral notches. In the contrast ratio measurement, we applied length-31 M-sequence spectral phase coding in the decoder to emulate the improperly decoded CDMA signal while the properly decoded signal was emulated through applying constant phase in the decoder. The CDMA spectra with 10 and 20 notches are shown in Fig. 6.11 and Fig. 6.12 as examples.

Fig. 6.13 shows the additional gain required for CDMA signals to achieve the same 20-dB contrast in the fiber thresholder with different numbers of spectral notches. In each case, the FWHM bandwidth of each individual notch is $\sim 0.3nm$ and the notches are evenly distributed across the CDMA spectrum. We observed that only $<$ 3dB additional gain is required to compensate the peak power reduction in the CDMA signals when the number of spectral notches increases up to 20, which would correspond to 20 WDM channels with $\sim$ 100 GHz channel separation. This result indicates the feasibility of error-free CDMA detection with closely spaced WDM users in a hybrid overlay system.

In conclusion, we have presented a new multiplexing concept - a spectrally overlaid WDM-CDMA scheme. The study on the cross-talk between WDM and CDMA signals in this system provides an evidence for the feasibility of the hybrid WDM-CDMA operation.

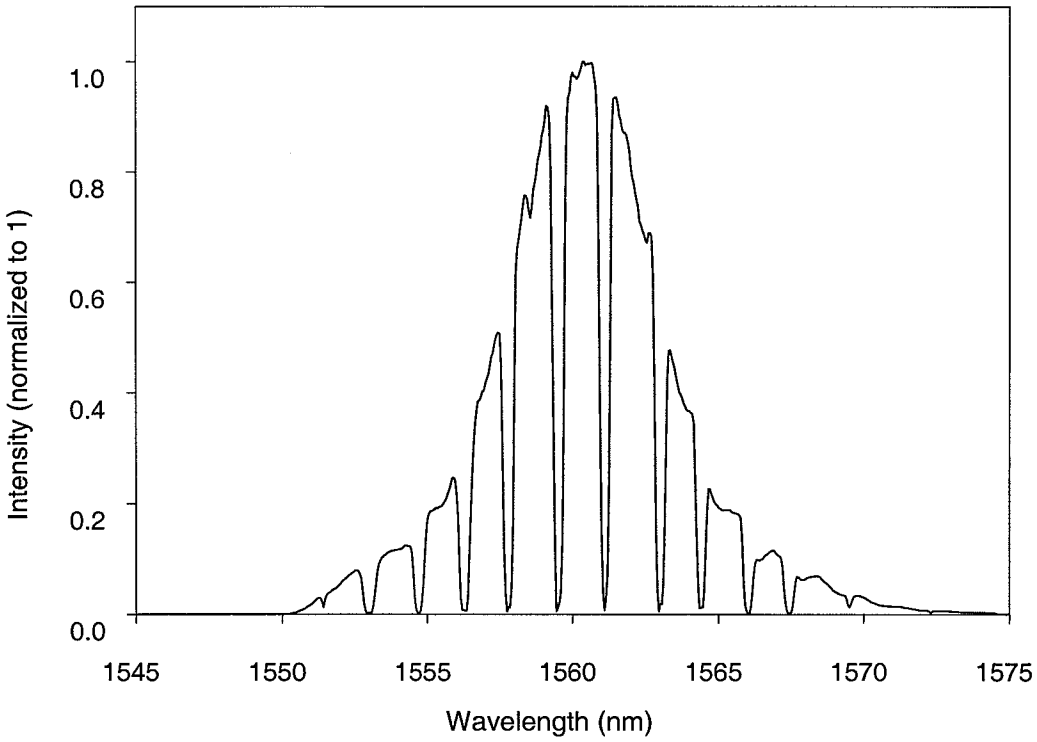

Fig. 6.11. Optical spectrum of CDMA signals with 10 spectral notches.

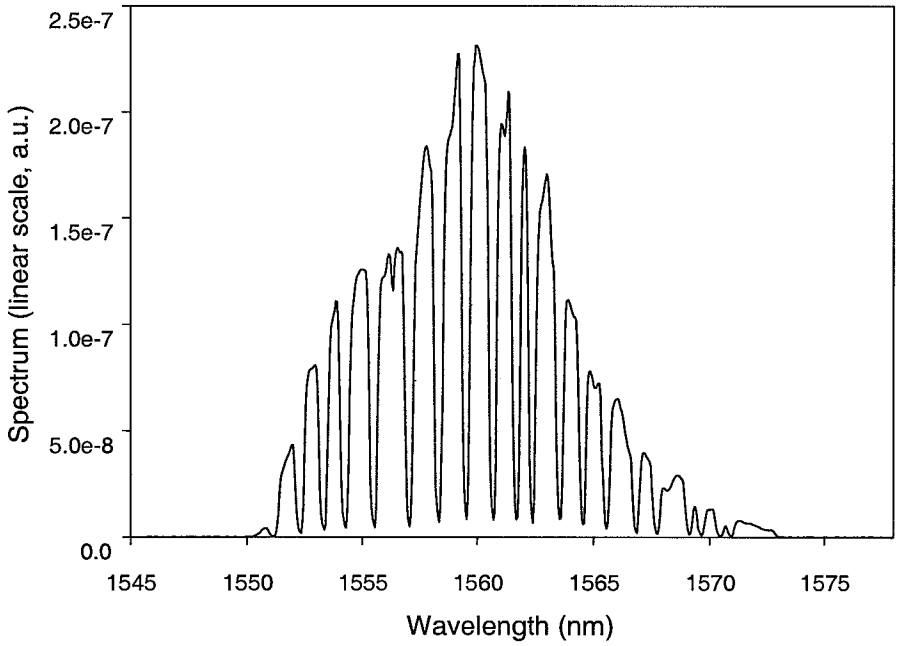

Fig. 6.12. Optical spectrum of CDMA signals with 20 spectral notches.

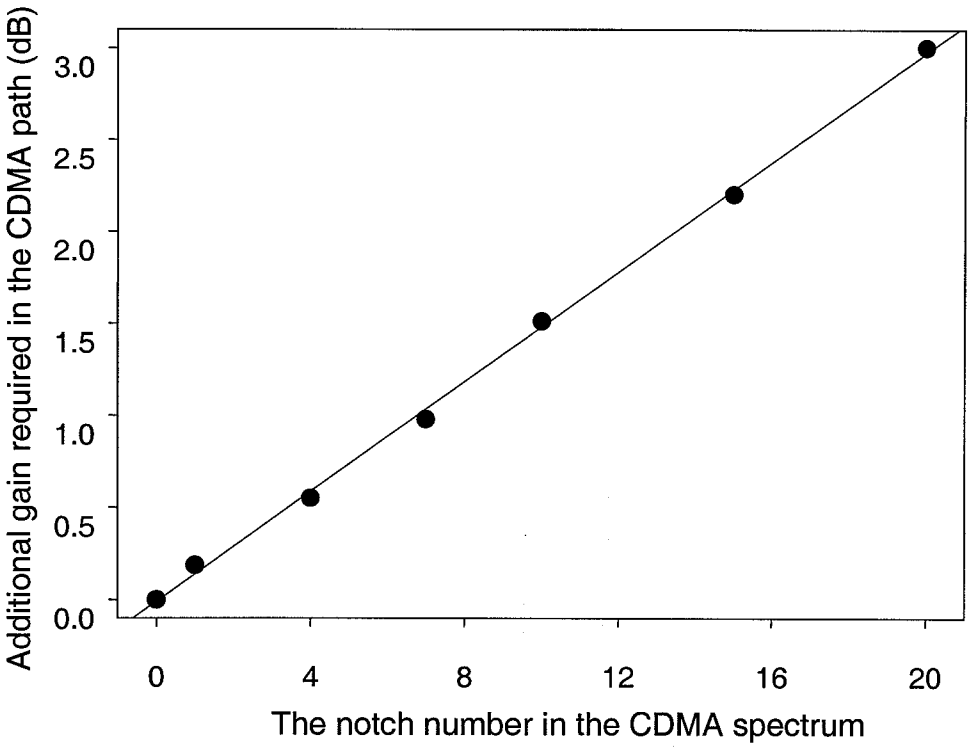

Fig. 6.13. Additional gain required for the CDMA channel with multiple spectral notches to achieve the same $\sim$ 20−dB thresholding contrast ratio in the fiber thresholder compared to the case when no-notch is used in the CDMA spectrum. Solid line, linear regression.

6.6 Transmission of Bit-parallel WDM Data over a Fiber Link Designed for Ultrashort-pulse CDMA Operation

In a hybrid WDM-CDMA system, it is expected that the same fiber transmission link is shared by both WDM users and CDMA users. This section describes an experiment to demonstrate that the dispersion compensated fiber link designed for femtosecond-pulse CDMA operation also find a unique application in WDM data transmission, in particular the bit-parallel data transmission with ultralow timing skew for computer communications application. Note that the transmission of WDM data in the hybrid operation is not limited to the bit-parallel data transmission format. Nonetheless, the successful transmission of bit-parallel data over a dispersion compensated link indicates that optical WDM and CDMA can share the same physical medium in the hybrid WDM-CDMA scheme. This work also shows that the dispersion compensating fiber technique is effective in timing skew compensation. The experiment was arranged in such a way that it allows us to directly measure the small residual dispersion slope of a 2.5 km fiber link dispersion compensated with picosecond precision. It provides us a reliable way to characterize the dispersion compensated fiber link.

6.6.1 Bit-parallel WDM Data Transmission and Timing Skew

The demand for higher data rate communications has grown substantially in parallel processing computer networks [65, 66]. Difficulties in producing electronic circuits (serializer/deserializer, etc.) with required speeds at a reasonable cost limit interconnections based on the conventional serial data transmission format for distributed multiprocessor systems. Bit-parallel WDM data transmission has been proposed as an alternative strategy for computer communications [65, 66, 67]. In this technique, each bit of a byte (or word) of data is transmitted at a separate wavelength, and wavelength division multiplexing (WDM) is used to transmit the data bytes over a single fiber. Since the transmission of data in parallel form (serial-by-byte, parallel-by-bit) is compatible with computer architecture, electronic bottlenecks are reduced. The timing alignment between different bits within one byte (or word) is crucial to

the success of bit-parallel WDM data transmission. The attractive feature of this technique versus fiber ribbons [68] is that the timing misalignment imposed by multiple path lengths and complex connectors are eliminated. However, the timing skew between different bits due to the group velocity dispersion (GVD) of the fiber link is still a major problem. Several techniques have been proposed to deal with this timing skew. These techniques include the use of dispersion-shifted fiber [65], electronic bit realignment in the receiver [67], and a shepherd pulse technique [69] based on nonlinear optics. Drawbacks of these techniques include high pulse energy to induce fiber nonlinearity [69] or lack of high re-synchronization accuracy ($\sim$ 100 ps) [67]. In addition, the shepherd pulse technique requires that the passive component skew be within the capture range of the shepherd pulse ($\sim$5 ps), which complicates the design of optical couplers [70]. It is desirable to develop a linear timing-skew compensation technique to improve the timing alignment accuracy for future ultra-high capacity WDM data transmission. In this chapter, we demonstrate that the DCF technique not only is effective in dispersion compensation for femtosecond-pulse CDMA data transmission, but also can be conveniently employed to precisely compensate the timing skew for local area computer communication networks. To show this, we generated 7 synchronized WDM channels over a 15 nm wavelength span from a single femtosecond pulse and a pulse shaper, and measured the timing skew over a 2.5 km dispersion compensated fiber link. The total of less than 3 ps timing skew, limited by the third-order dispersion, was measured over the transmission link.

6.6.2 Experiments and Results on Timing Skew Compensation

When synchronized WDM wavelengths are launched into a standard single-mode fiber (SMF), they will arrive at the receiver end at different times due to the group velocity dispersion (GVD) of the fiber link. The dispersion effect can be expressed in terms of the variation in the group delay per unit length $T(\omega)$ with respect to deviations in wavelength λ as shown in Eq. 3.5. This GVD induced timing skew can be substantial ($> 200ps$) when the length of a SMF transmission link is over several kilometers for a sufficient wide WDM spectral range (over 10 nm). The

dispersion-compensated fiber link is constructed by concatenating a standard SMF and a carefully chosen DCF. The overall dispersion of the compensated link is given by

$$D = \frac{D_{smf} \times L_{smf} + D_{dcf} \times L_{dcf}}{L_{smf} + L_{dcf}} \tag{6.14}$$

where D_{smf} and D_{dcf} are the 2nd order dispersion of SMF and DCF link respectively. L_{smf} and L_{dcf} represent the lengths of the corresponding fibers. The DCF has the opposite sign of 2nd order dispersion and dispersion slope with respect to that of SMF. With an optimal length ratio between DCF and SMF, DCF will cancel out all the 2nd order dispersion of SMF. The third order dispersion is also partially compensated. In this work, we demonstrate that this SMF/DCF fiber link can reduce the timing skew for WDM bit-parallel data transmission to a picosecond range. The remaining timing skew over the dispersion-compensated link is determined by the residual 3rd order dispersion and is less than 3 ps over our 2.5-km link.

The experimental setup for generating synchronized multiple-wavelength channels and for timing skew measurement is shown in Fig. 6.14. A stretched-pulse passively mode-locking fiber ring laser [56] generating 150 fs (FWHM) pulses at 35MHz-repetition rate serves as a broadband source. The synchronized multiple-wavelength channels were derived from the femtosecond laser pulses using a modified pulse shaper, which is equipped with a 128-pixel liquid crystal modulator array (LCM) [9]. We used the pulse shaper-LCM combination as a voltage programmable amplitude modulator with independent control over different wavelength components. A total of 7 wavelength channels ($\sim$0.83 nm FWHM per channel) with channel separation $\sim$2.5 nm were generated over a 15 nm span from the initial femtosecond pulse. The on/off contrast ratio of each channel reaches 30 dB. By applying appropriate voltages on the LCM, we were also able to equalize the amplitudes of each individual wavelength channel, which vary by $\sim$ 3dB before equalization. Fig. 6.15 shows the equalized spectra of 7 channels generated from the pulse shaper.

The dispersion compensated link used in our experiments consists of a 2.06-km standard SMF (AT&T 5D) ($D = 17$ ps/km/nm , $D' = 0.06$ ps/km/nm^2 at 1550nm)

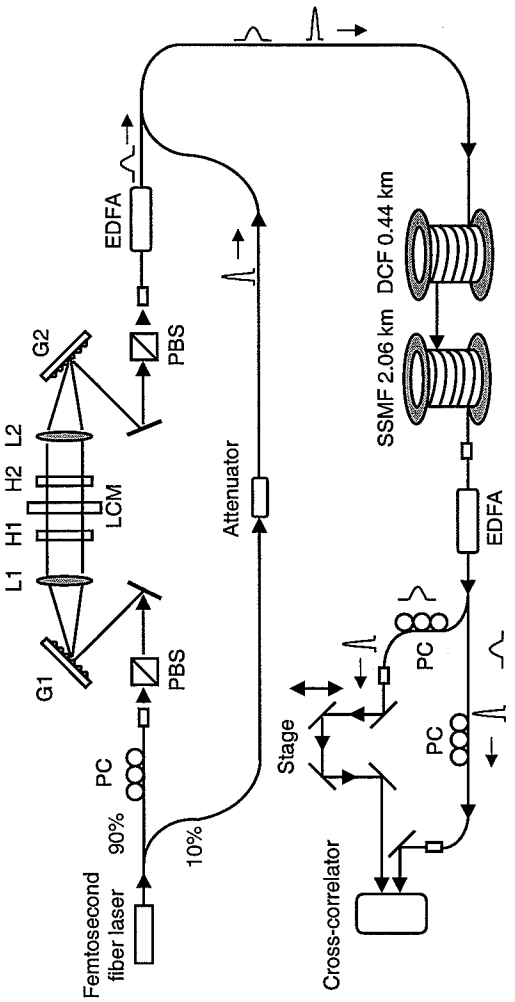

Fig. 6.14. Experiment setup for the generation of WDM multiple wavelength channels and for timing skew measurement. LCM: liquid crystal modulator array; H1, H2: half-wave plate; L1, L2: lens; G1, G2: grating; PBS: polarization beam splitter; PC: polarization controller.

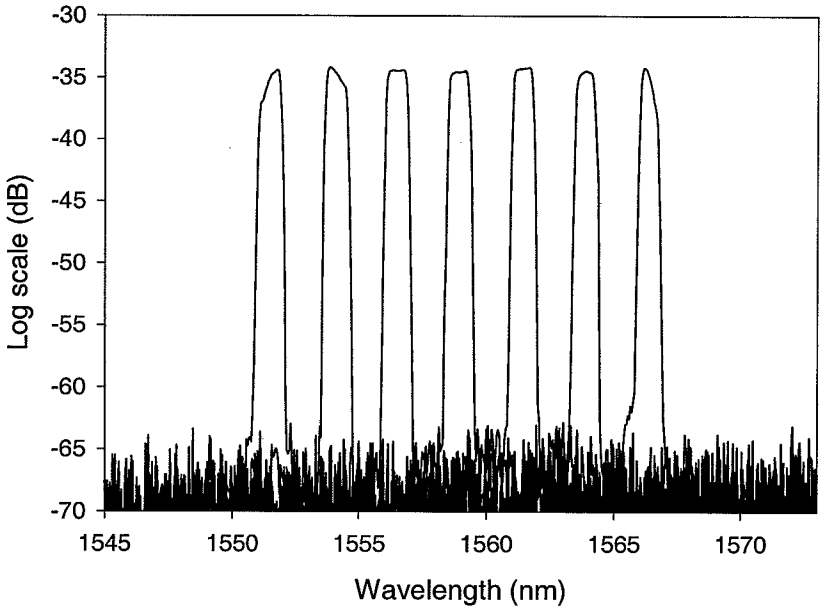

Fig. 6.15. Spectra of 7 WDM wavelength channels after the amplitude equalization (log scale).

and a 0.44 km length of DCF [15, 37, 71]. The DCF ($D = -76$ ps/km/nm , $D' = 0.2$ ps/km/nm^2) compensates the 2nd order dispersion and much of the third-order dispersion (dispersion slope) of SMF. Previously, the transmission of 250-fsec pulses over this link with only $\sim$ two times pulse broadening as limited by the residual third-order dispersion has been shown [15, 71]. The timing-skew of the 2.5-km dispersion compensated link was measured by comparing the relative timing position of each individual wavelength channel before and after the link. This was accomplished through intensity cross-correlation using second harmonic generation with a short reference pulse derived from the fiber laser using a 1 x 2 fiber splitter. The experiment was performed with one wavelength channel turned on at a time. To suppress laser jitter effects and environmentally induced timing changes, we launched both the signal pulse ($\sim$ 6.5 ps FWHM for one channel) and the reference pulse ($\sim$ 0.5 ps FWHM) into the 2.5-km transmission link with $\sim$900 ps delay in between and separated them at the end of the link for the cross-correlation measurement. The power levels were kept low enough to avoid any fiber nonlinearity in the link.

Fig. 6.16 shows 7 well-aligned signal pulses (bits) at different wavelengths before the transmission link. The timing misalignment ($\sim$ 525 psec estimated) incurred in the 2.06 km SMF alone is compensated by DCF. Fig. 6.17 shows measurements of different wavelengths (bits) after the transmission link. The cross-correlation traces of 7 signal pulses show similar pulsewidth ($\sim$6.5ps) and pulse shape before and after the link. The timing skew of the dispersion compensated link (i.e. the difference between Fig. 6.16 and Fig. 6.17) is shown in Fig. 6.18.

A maximum of only 2.4 ps timing skew was observed over the 15 nm spectral span. Based on the timing variations of several independent measurements, we estimate the timing accuracy of our measurement reaches $\pm$0.2 ps. The quadratic nature of the wavelength dependent time delay shown in Fig. 6.18 indicates the timing skew over the link is limited by the residual 3rd dispersion of the compensated link. From our data, we calculate a zero net dispersion at 1562 nm with a dispersion slope $D' = 0.017$ ps/km/nm^2 ($\beta_3 = 0.027$ ps^3/km). The accuracy of the β_3 measurement for the 2.5-km

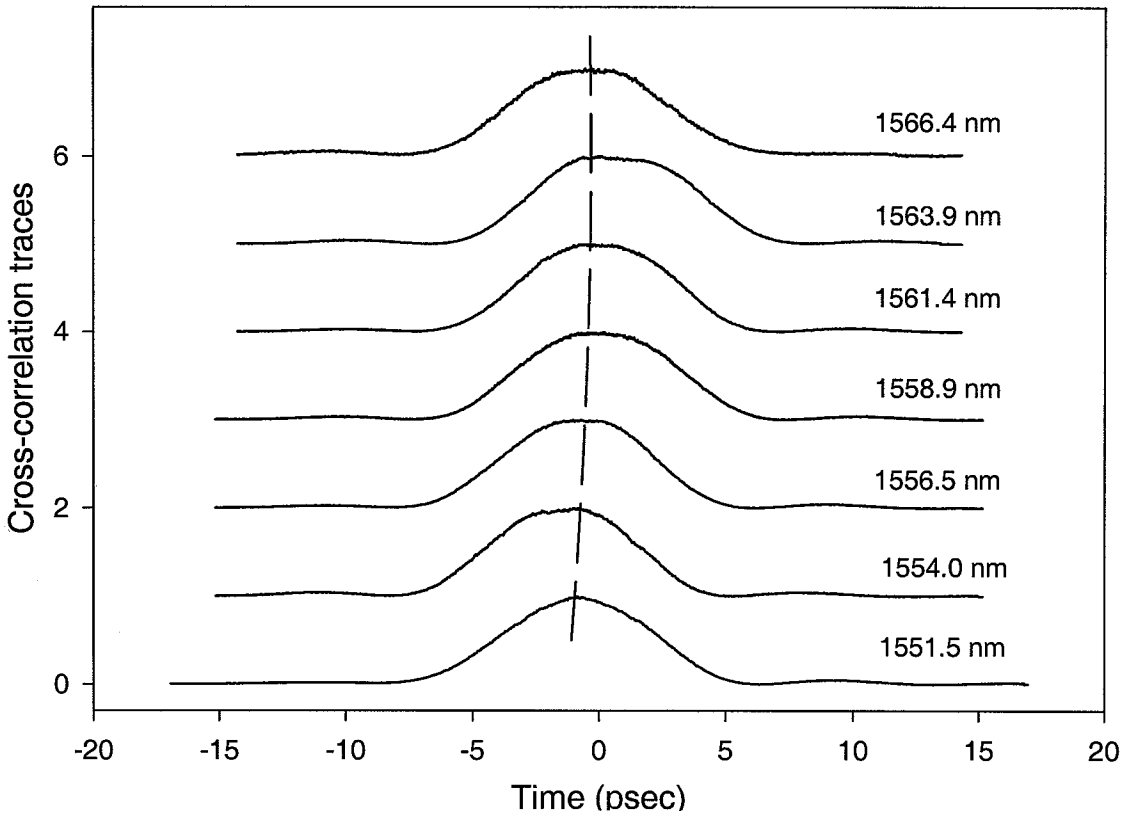

Fig. 6.16. 7 signal pulses (bits) at different wavelengths before the transmission link (dashed line: peak position fitting).

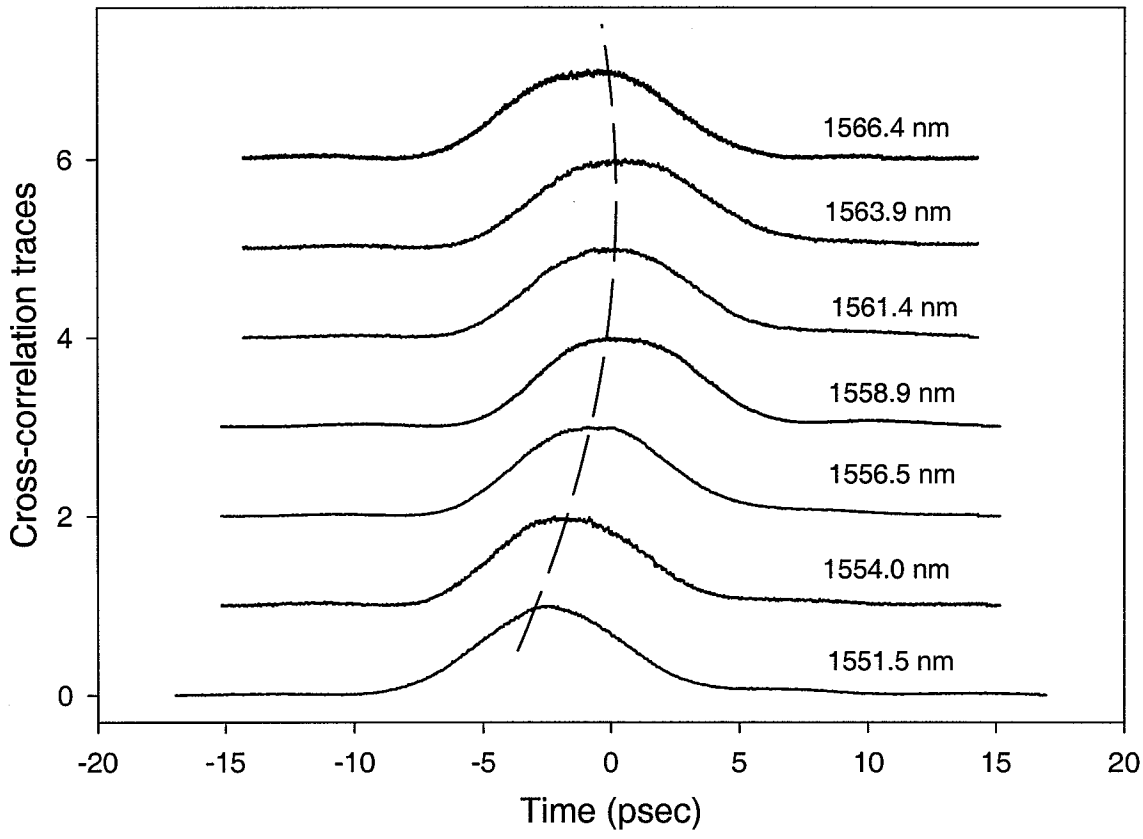

Fig. 6.17. 7 signal pulses (bits) at different wavelengths after the transmission link (dashed line: peak position fitting).

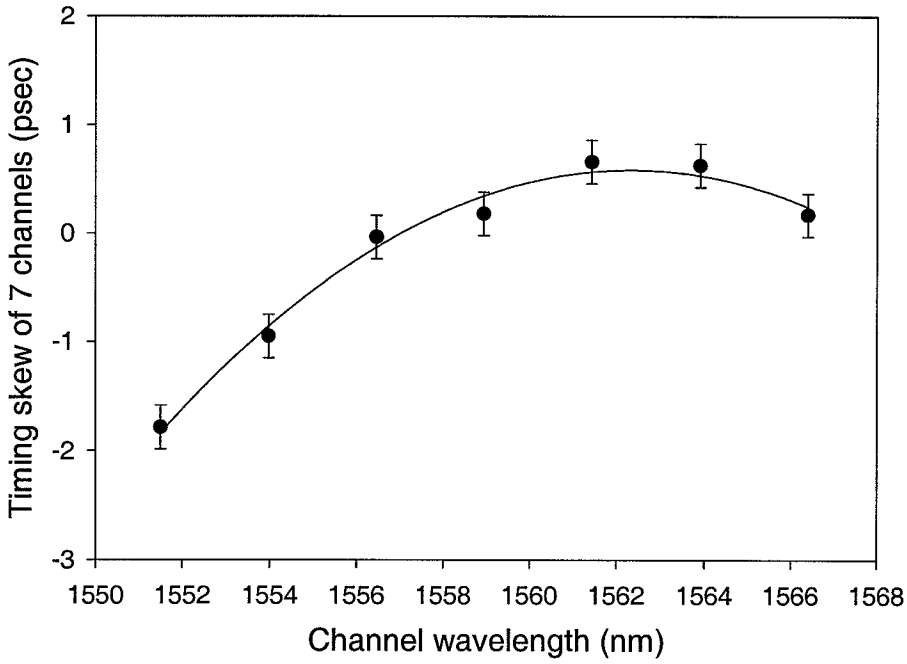

Fig. 6.18. Measured timing skew of the 2.5-km dispersion compensated link (solid line: fitting curve).

fiber link is estimated to be $\pm 0.003\ ps^3/km$. This result is consistent with our previous estimation of the dispersion slope ($\beta_3 \approx 0.026$ ps^3/km) by our colleague, which was based on matching the measured and simulated pulse shapes in a femtosecond pulse transmission experiment [15]. It is noted that previous experiments were designed to yield an approximation but not an exact measurement of the residual dispersion. The current experiment provides a direct measurement of residual dispersion slope and therefore gives a more reliable result. The measured dispersion slope is ~ 4 times less that of dispersion shifted fiber ($D' = \sim 0.06\ ps/km/nm^2$). It indicates the timing skew over a dispersion compensated fiber link is significantly smaller than that over a dispersion-shifted fiber link with equivalent length. We note that with $< 3ps$ timing-skew between different wavelength channels in the transmission link, the aggregate data throughput in a timing-skew limited WDM bit-parallel transmission link could reach over 100 Gbytes/s. It also shows that the dispersion compensated fiber link can be used both by WDM data and by CDMA femtosecond pulses.

7. Summary

This dissertation demonstrates and extends the technical feasibility of ultrashort-pulse optical code-division multiple-access scheme for fiber-optic communications. The femtosecond fiber laser constructed for CDMA experiments provides wide spectral bandwidth and can be reliably modelocked with communication grade diode pump lasers. The efforts on distortion-less transmission of subpicosecond pulses over a 10-km fiber link extends the coverage of ultrashort-pulse CDMA technique to the range suitable for local-area network applications. The theoretical and experimental study on fiber nonlinearity during sub-picosecond pulse propagation indicates the power limit in the CDMA transmission link. At the system level, I presented the bit-error-rate measurements of a CDMA channel under multi-access interference. It provides the first experimental evidence for the possibility of error-free ultrashort-pulse CDMA operation in an environment with large number of users. Finally, I presented the first system experiment on spectrally overlaying CDMA on WDM. It demonstrates the physical feasibility of hybrid WDM/CDMA operation. In conclusion, the device and system studies documented here have contributed the development of coherent CDMA technique. It lays a foundation for the future work in this area. Although this thesis research is focused on the implementation of ultrashort-pulse CDMA, some research results also find impacts to other multiplexing approaches. For example, dispersion compensation, fiber nonlinearity, and fiber lasers, etc. are very important topics in optical TDM and WDM fiber communication systems as well.

Future work on ultrashort-pulse CDMA scheme could be directed toward several areas. First, it is important to develop compact yet economical photonic-devices for ultrashort-pulse CDMA operation. Most of the devices used in this thesis work are not suitable for field applications. For examples, the femtosecond pulse shaper used

for spectral phase coding are bulky and not convenient to align. At current stage, it is not practical to install a pulse shaper setup at each user node in a fiber-optic networks. Possible candidate for replacing the grating/lens based pulse shapers could be arrayed-waveguide-gratings. Second, it is important to develop polarization-insensitive phase coding and nonlinear thresholding schemes for stable CDMA operation. In current experiments, due to the use of polarization-sensitive elements, such as gratings and liquid-crystal modulator, any polariztion drift caused by the environmental fluctuation will lead to system output changes. This is detrimental for the reliable CDMA operation. Third, current ultrashort-pulse CDMA experiments are conducted at tens of Mb/s data rate limited by the repetition rate of the fiber laser. Although it suffices to demonstrate the feasibility and physical principle of CDMA, this data rate is well below the desired Gb/s channel operation rate. It is important to develop a short-pulse laser source with GHz or above repetition rate, with which future study on high-speed CDMA operation could be truely carried out. Finally, although we have demonstrated the feasibility of hybrid WDM/CDMA opertion, our WDM/CDMA test bed involves only one CDMA and two WDM channels. More WDM and CDMA users could be inlcuded in the future work to fully evaluate the hybrid system. The system design could also be improved through using the photonic devices with better performance such as a nonlinear CDMA thresholder with lower input power requirement compared to the fiber thresholder, spectral phase encoder and decoder with lower insertation loss compared to the grating/lens based pulse shaper.

LIST OF REFERENCES

[1] H. P. Sardesai, C. C. Chang, and A. M. Weiner, "A femtosecond code-division multiple-access communication system test bed," *J. Lightwave Technol.*, vol. 16, pp. 1953–1964, 1998.

[2] D. Zaccarin and M. Kavehrad, "An optical CDMA system based on spectral encoding of led," *IEEE Photon. Technol. Lett.*, vol. 4, pp. 479–483, 1993.

[3] M. E. Marhic and Y. L. Chang, "Pulse coding and coherent decoding in fiber-optic ladder networks," *Electron. Lett.*, vol. 25, no. 22, pp. 1535–1536, 1989.

[4] J. Y. Hui, "Pattern code modulation and optical decoding - A novel code-division multiplexing technique for multifiber networks," *IEEE J. Sel. Areas Commun.*, vol. 3, pp. 916–927, 1985.

[5] A. Grunnet-Jepsen, A. E. Johnson, E. S. Maniloff, T. Mossberg, M. Munroe, and J. Sweetser, "Fibre Bragg grating based spectral encoder/decoder for lightwave CDMA," *Electron. Lett.*, vol. 35, pp. 1096–1097, 1999.

[6] H. P. Sardesai and A. M. Weiner, "Nonlinear fiber-optic receiver for ultrashort pulse code division multiple access communications," *Electron. Lett.*, vol. 33, pp. 610–611, 1997.

[7] D. Sampson, G. J. Pendock, and R. A. Griffin, "Photonic code-division multiple access communications," *Fiber Integrated Opt.*, vol. 16, pp. 129–157, 1997.

[8] J. A. Salehi, A. M. Weiner, and J. P. Heritage, "Coherent ultrashort light pulse code-division multiple access communication systems," *J. Lightwave Technol.*, vol. 8, pp. 478–491, 1990.

[9] A. M. Weiner, D. E. Leaird, J. S. Patel, and J. R. Wullert, "Programmable shaping of femtosecond optical pulses by use of 128-element liquid crystal phase modulator," *IEEE J. Quantum. Electron.*, vol. 28, pp. 908–920, 1992.

[10] T. Kurokawa, H. Tsuda, K. Okamoto, K. Naganuma, Y. I. H. Takenouchi, and M. Ishii, "Time-space-conversion optical signal processing using arrayed-waveguide grating," *Electron. Lett.*, vol. 33, pp. 1890–1891, 1997.

[11] J. E. Ford, J. A. Walker, M. C. Nuss, and D. A. B. Miller, "32 channel WDM graphic equalizer," in *IEEE LEOS 1996 Summer Topical Meetings on Broadband Optical Networks*, (Keystone, CO), pp. 26–27, August 1996.

[12] A. M. Weiner, J. P. Hertage, and J. A. Salehi, "Encoding and decoding of femtosecond pulses," *Opt. Lett.*, vol. 13, pp. 300–302, 1988.

[13] A. M. Weiner, "Femtosecond optical pulse shaping and processing," *Progr. Quantum. Electron.*, vol. 3, pp. 161–233, 1995.

[14] C. C. Chang, H. Sardesai, and A. M. Weiner, "Code-division multiple access encoding and decoding of femtosecond optical pulses over a 2.5km fiber link," *IEEE Photon. Technol. Lett.*, vol. 10, pp. 171–173, 1998.

[15] C. Chang and A. M. Weiner, "Fiber transmission of sub-500-fs pulses using dispersion-compensating fiber," *IEEE J. Quantum Electron.*, vol. 33, pp. 1455–1464, 1997.

[16] C. Chang, H. P. Sardesai, and A. M. Weiner, "Dispersion-free fiber transmission for femtosecond pulses using a dispersion-compensating fiber and a programmable pulse shaper," *Opt. Lett.*, vol. 23, pp. 283–285, 1998.

[17] H. P. Sardesai and A. M. Weiner, "A nonlinear fiber-optic thresholder for spectrally coded ultrashort pulses with 36db extinction ratio," in *Tech. Dig. OSA TOPS Ultrafast Electron. Optoelectron.*, vol. 13, 1997.

[18] Z. Zheng, A. M. Weiner, J. H. Marsh, and M. M. Karkhanehchi, "Ultrafast optical thresholding based on two-photon absorption GaAs waveguide photodetectors," *IEEE Photon. Technol. Lett.*, vol. 9, pp. 493–405, 1997.

[19] Z. Zheng and A. M. Weiner, "Spectral phase correlation of coded femtosecond pulses by second-harmonic generation in thick nonlinear crystals," *Opt. Lett.*, vol. 25, pp. 984–986, 2000.

[20] S. Shen and A. M. Weiner, "Complete dispersion compensation for 400-fs pulse transmission over 10-km fiber link using dispersion compensating fiber and spectral phase equalizer," *IEEE Photonics Technol. Lett.*, vol. 11, pp. 827–829, 1999.

[21] S. Shen, C. C. Chang, H. P. Sardesai, V. Binjrajka, and A. M. . Weiner, "Effects of self-phase modulation on sub-500 fs pulse transmission over dispersion compensated fiber links," *IEEE J. of Lightwave Technol. Lett.*, vol. 17, pp. 452–461, 1999.

[22] S. Shen and A. M. Weiner, "Timing-skew compensation for bit-parallel wdm data transmission with picosecond precision," *IEEE Photonics Technol. Lett.*, vol. 11, pp. 566–568, 1999.

[23] K. Tamura, H. A. Haus, and E. P. Ippen, "Self-starting additive pulse mode-locking erbium fiber ring laser," *Electron. Lett.*, vol. 28, pp. 2226–2228, 1992.

[24] K. Tamura, J. Jacobson, E. P. Ippen, H. A. Haus, and J. G. Fujimoto, "Unidirectional ring resonators for self-starting passively mode-locked lasers," *Opt. Lett.*, vol. 18, pp. 220–222, 1993.

[25] S. M. J. Kelly, "Characteristic sideband instability of periodically amplified average soliton," *Electron. Lett.*, vol. 28, no. 8, pp. 806–807, 1992.

[26] S. Namiki, C. X. Yu, and H. A. Haus, "Obseravtion of nearly quantum-limited timing jitter in an all-fiber ring laser," *J. Opt. Soc. Am. B*, vol. 13, pp. 2817–2823, 1996.

[27] M. Endo, G. Ghosh, and Y. Tanaka, "Timing jitter reduction in a passively mode-locked fiber laser," *Jpn. J. Appl. Phys.*, vol. 36, pp. 860–862, 1997.

[28] S. Kawanishi, H. Takara, O. Kamatani, and M. Saruwatari, "200 Gbit/s 100 km time-division-multiplexed optical transmission using supercontinuum pulses with prescaled PPL timing extraction and all-optical demultiplexing," *Electron. Lett.*, vol. 31, pp. 816–817, 1995.

[29] H. Tsuda, H. Takenouchi, T. Ishii, K. Okamoto, T. Goh, K. Sato, A. Hirano, T. Kurokawa, and C. Amano, "Spectral encoding and decoding of 10 *g*bit/s femtosecond pulses using high resolution arrayed-waveguide grating," *Electron. Lett.*, vol. 35, pp. 1186–1188, 1999.

[30] S. Watanabe, T. Naito, and T. Chikama, "Compensation of chromatic dispersion in a single-mode fiber by optical phase conjugation," *IEEE Photon. Technol. Lett.*, vol. 5, pp. 92–95, 1993.

[31] R. Jopson, A. H. Gnauck, and R. M. Derosier, "10-Gb/s 360-km transmission over normal-dispersion fiber using mid-system spectral inversion," in *Conference on Optical Fiber Communications, 1993 Technical Digest Series*, pp. 17–20, 1993.

[32] A. D. Ellis, M. C. Tatham, D. A. O. Davies, D. Nessett, D. G. Moodie, and G. Sherlock, "40 Gbit/s transmission over 202 km of standard fiber using midspan spectral inversion," *Electron. Lett.*, vol. 31, pp. 299–301, 1995.

[33] R. Kashyap, S. V. Chernikov, P. F. Mckee, and J. R. Taylor, "30ps chromatic dispersion compensation of 400 fs pulses at 100 *g*bits/s in optical fibers using an all fiber photoinduced chirped reflection grating," *Electron. Lett.*, vol. 30, pp. 1078–1080, 1994.

[34] L. Dong, M. J. Cole, A. D. Ellis, M. Durkin, M. Ibsen, V. Gusmeroli, and R. I. Laming, "40 Gbit/s 1.55 nm transmission over 109 km of nondispersion shifted fiber with long continuously chirped fiber grating," in *Conference on Optical Fiber Communications, 1997 Technical Digest Series*, pp. 391–394, 1997.

[35] M. Stern, J. P. Heritage, and E. W. Chase, "Grating compensation of third-order fiber dispersion," *IEEE J. Ouan. Electron.*, vol. 28, pp. 2742–2748, 1992.

[36] J. M. Dugan, A. J. Price, M. Ramadan, D. L. Wolf, E. F. Murphy, A. J. Antos, D. K. Smith, and D. W. Hall, "All-optical fiber-based 1550-nm dispersion compensation in a 10 Gbit/s, 150km transmission experiment over 1310 nm optimized fiber," in *Conference on Optical Fiber Communications, 1992 Technical Digest Series*, pp. PD–14, 1992.

[37] A. M. Vengsarkar, A. E. Miller, M. Haner, A. H. Gnauck, W. A. Reed, and K. L. Walker, "Fundamental-mode dispersion-compensating fibers: Design consideration and experiments," in *Conference on Optical Fiber Communications, 1994 Technical Digest Series*, p. 225, 1994.

[38] C. Lin, H. Kogelnik, and L. Cohen, "Optical-pulse equalization of low-dispersion transmission in single-mode fibers in the 1.3-1.7 μm spectral region," *Opt. Lett.*, vol. 5, pp. 476–478, 1980.

[39] S. Kawanishi, H. Takara, T. Morioka, O. Kamatani, K. Takiguchi, T. Kitoh, and M. Saruwatari, "400 Gbit/s TDM transmission of 0.98 ps pulses over 40 km employing dispersion slope compensation," in *Conference on Optical Fiber Communication, 1996 Technical Digest Series*, vol. 2, pp. 423–426, 1996.

[40] E. Yoshida, T. Yamamoto, A. Sahara, and M. Nakazawa, "320 Gbit/s TDM transmission over 120km using 400fs pulse train," *Electron. Lett.*, vol. 34, pp. 1004–1005, 1998.

[41] E. Wolf, ed., vol. 20. Amsterdam, North-Holland: Academic Press, 1983.

[42] M. Schiess, "Comparison of dispersion compensation schemes including fiber nonlinearities," *J. Opt. Commun.*, vol. 16, pp. 92–98, 1995.

[43] A. Berntson, D. Anderson, M. Lisak, M. L. Quiroga-Teixeiro, and M. Karlsson, "Self phase modulation in dispersion compensated optical fibre transmission systems," *Opt. Commun.*, vol. 130, pp. 153–162, 1996.

[44] F. Kuppers, A. Mattheus, and R. Ries, "Optimized design of passive fibre compensated transmission systems in view of kerr non-linearity," *Pure Appl. Opt.*, vol. 4, pp. 459–467, 1995.

[45] M. Stern, J. P. Heritage, R. N. Thurston, and S. Tu, "Self-phase modulation and dispersion in high data rate fiber-optic transmission systems," *J. of Lightwave Technol.*, vol. 8, no. 7, pp. 1009–1016, 1990.

[46] R. Ludwig, W. Pieper, H. G. Weber, D. Breuer, K. Petermann, F. Kuppers, and A. Mattheus, "Unrepeatered 40 Gbit/s RZ single channel transmission over 150 km of standard single mode fiber at 1.55 μm," *Electron. Lett.*, vol. 33, pp. 76–77, 1997.

[47] J. D. Minelly, A. Galvanauskas, M. E. Fermann, D. Harter, J. E. Caplen, Z. J. Chen, and D. N. Payne, "Femtosecond pulse amplification in cladding-pumped fibers," *Opt. Lett.*, vol. 20, pp. 1797–1799, 1995.

[48] W. J. Tomlinson, R. H. Stolen, and C. V. Shank, "Compression of optical pulses chirped by self-phase modulation in fibers," *J. Opt. Soc. Am. B*, vol. 1, pp. 139–149, 1984.

[49] G. P. Agrawal, *Nonlinear fiber optics.* San Diego, CA: Academic Press, 1995.

[50] V. L. D. Silva, Y. M. Liu, A. J. Antos, G. E. Berkey, and M. A. Newhouse, "Comparison of nonlinear coefficient of optical fibers at 1550nm," in *Conference on Optical Fiber Communications, 1996 Technical Digest Series*, pp. 202–203, 1996.

[51] T. Kato, Y. Suetsugu, M. Takagi, E. Sasaoka, and M. Nishimura, "Measurement of the nonlinear refractive index in optical fiber by the cross-phase-modulation method with depolarized pump light," *Opt. Lett*, vol. 9, pp. 988–990, 1995.

[52] M. Oberthaler and R. A. Hopfel, "Special narrowing of ultrashort laser pulses by self phase modulation in optical fibers," *Appl. Physics Lett.*, vol. 63, no. 8, pp. 1017–1019, 1993.

[53] K. S. Kim, R. H. Stolen, W. A. Reed, and K. W. Quoi, "Measurement of the nonlinear index of silica-core and dispersion-shifted fibers," *Opt. Lett.*, vol. 19, pp. 257–259, 1994.

[54] R. H. Stolen, K. S. Kim, S. E. Evangelides, G. T. Harvey, and W. A. Reed, "Nonlinear-index measurement by SPM at 1.55 μm," in *Conference on Optical Fiber Communications, 1995 Technical Digest Series*, pp. 312–313, 1995.

[55] J. A. Salehi, "Code division multiple-access techniques in optical fiber networks-Part I: Fundamental principles," *IEEE Trans. Commun.*, vol. 37, pp. 824–833, 1989.

[56] K. Tamura, C. R. Doerr, L. E. Nelson, H. A. Haus, and E. P. Ippen, "Technique for obtaining high-energy ultrashort pulses from an additive-pulse mode-locked erbium-doped fiber ring laser," *Opt. Lett.*, vol. 19, pp. 46–48, 1994.

[57] G. Nykolak, B. Brown, P. F. Szajowski, J. J. Auborn, H. M. Presby, G. Raybon, and B. Mikkelsen, "A 160 Gb/s free space transmission link," in *Conference on Lasers and Electro-Optics, 2000 Technical Digest Series*, (San Francisco, CA), pp. CPD15/29–30, 2000.

[58] S. Kawanishi, H. Takara, K. Uchiyama, I. Shake, and K. Mori, "3 Tbit/s (160 Gbit/s x 19 ch) OTDM-WDM transmission experiment," in *Conference on Optical Fiber Communication, 1999 Technical Digest Series*, (San Diego, CA), p. PD1, 1999.

[59] C. D. Chen, I. Kim, O. Mizuhara, T. V. Nguyen, K. Ogawa, R. E. Tench, L. D. Tzeng, , and P. D. Yeates, "1-Tb/s (40 Gb/s x 25ch) WDM transmission experiment over 342km of TrueWave((non-zero dispersion) fiber," in *Conference on Optical Fiber Communication, 1999 Technical Digest Series*, (San Diego, CA), p. PD7, 1999.

[60] A. M. Weiner, M. R. Bell, E. J. Coyle, and J. S. Lehnert, "New optical networks based on ultrabroadband spectral encoding," *A proposal to National Science Foundation*, 1993.

[61] J. A. Salehi and C. A. Brackett, "Code division multiple access techniques in optical fiber networks - part II: system performance analysis," *IEEE Trans. Commun.*, vol. 37, pp. 834–842, 1989.

[62] G. P. Agrawal, *Fiber-Optic Communication Systems.* New York: John Wiley & Sons, 1992.

[63] L. Boivin, M. C. Nuss, J. Shah, D. A. B. Miller, and H. A. Haus, "Receiver sensitivity improvement by impulsive coding," *IEEE Photonics Technol. Lett.*, vol. 9, pp. 684–686, 1997.

[64] A. S. M. D. Pelusi, Y. Matsui, "Fourth-order dispersion suppression of ultrashort optical pulses by second-order dispersion and cosine phase modulation," *Opt. Lett.*, vol. 25, pp. 296–298, 2000.

[65] M. L. Loeb and G. R. S. Jr., "High-speed data transmission on an optical fiber using a byte-wide WDM system," *J. Lightwave Technol.*, vol. 1306-1311, p. 6, 1988.

[66] L. Bergman, J. Morookian, and C. Yeh, "An all-optical long-distance multi-Gbytes/s bit-parallel WDM single-fiber link," *J. Lightwave Technol.*, vol. 16, pp. 1577–1582, 1998.

[67] G. Jeong and J. W. Goodman, "Long distance parallel data link using WDM transmission with bit-skew compensation," *J. Lightwave Technol.*, vol. 14, pp. 655–660, 1996.

[68] A. Takai, T. Kato, S. Yamashita, S. Hanatani, Y. Motegi, K. Ito, H. Abe, and H. Kodera, "200-Mb/s/ch 100 -m optical subsystem interconnections using 8-channel 1.3 mm laser diode arrays and single-mode fiber arrays," *J. Lightwave Technol.*, vol. 12, pp. 260–270, 1994.

[69] L. Bergman, J. Morookian, C. Yeh, and S. Monacos, "Experimental verification of the pulse shepherding concept in dispersion-shifted single-mode fiber for bit-parallel wavelength links," in *The Fourth International Conference on Massively Parallel Processing Using Optical Interconnections*, pp. 25–29, 1997.

[70] A. J. Mendez and E. Segundo, "Design of constant optical path couplers for bit-parallel WDM systems," in *Proceeding of SPIE*, vol. 3234, pp. 94–99, 1998.

[71] C. C. Chang, A. M. Weiner, A. M. Vengsarkar, and D. W. Peckham, "Broadband fiber dispersion compensation for sub-100-fs pulses with a compression ratio of 300," *Opt. Lett.*, vol. 21, pp. 1141–1143, 1996.

VITA

Shuai Shen received his B. S. and M. S. degree in applied physics from Tsinghua University, P. R. China in 1992 and 1995 respectively. He started his Ph. D. study in electrical engineering at Purdue University in 1996. His research interests include lightwave communications, femtosecond pulse shaping, precision optical measurements and optical microsensor. Currently, he is a coauthor of two patents and 20 journal articles and conference presentations.

He is a member of OSA and IEEE.